UNIVERSITÀ DEGLI STUDI DI TRENTO

Doctoral School in Civil, Environmental and Mechanical Engineering

Topic 3. Modelling and Simulation

Alice Berardo

Numerical and Experimental Study on the Friction of Complex Surfaces

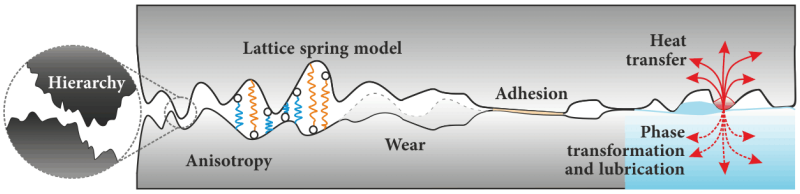

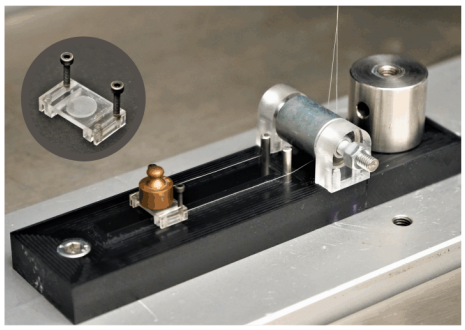

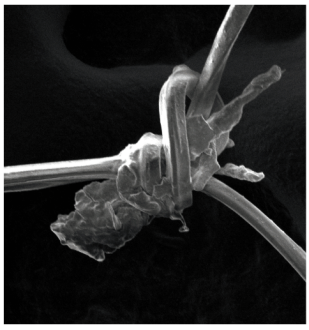

2017 - Doctoral thesis

UNIVERSITY OF TRENTO - Italy
Department of Civil, Environmental
and Mechanical Engineering

Doctoral School in Civil, Environmental and Mechanical Engineering
Topic 3. Modelling and Simulation - XXIX cycle 2014/2017

Doctoral Thesis - June 2018

Alice Berardo

Numerical and Experimental Study on the Friction of Complex Surfaces

Supervisor
Nicola M. Pugno, University of Trento

Credits of the cover image: Alice Berardo

University of Trento
Doctoral School in Civil, Environmental and Mechanical Engineering
http://web.unitn.it/en/dricam
Via Mesiano 77, I-38123 Trento
Tel. +39 0461 282670 / 2611 - *dicamphd@unitn.it*

Dedicated to

My beloved family

My patient boyfriend

My witty godfather, who unfortunately left too early

Acknowledgements

This work was made possible by the support that I have received from many people throughout my educational and professional career.

In particular, I would like to thank Professor Nicola Pugno of the University of Trento for the guidance and tutelage during these years of my PhD studies. He helped me to continue my education and gave me the freedom to explore new unexplored topics, always encouraging me to do my best.

I would like to thank Professor Cecilia Surace of the Politecnico of Turin for the help and guidance through my undergraduate and master studies that got me into the world of solid mechanics.

I would also like to thank Maria Fiorella Pantano for her experience, advice and friendship, which helped me to master my abilities and overcome the difficulties.

Thanks to all the people who have worked and collaborated with me during these years. Thanks for sharing your knowledge and improving mine.

Finally, I would like to thank my friends and colleagues, new and old friendships who have supported and believed in me.

Table of Contents

Acknowledgements 5

Table of Contents 7

List of Figures 11

List of Tables 25

List of Papers 27

Summary 29

Introduction 31

State of the art 32

Overview 34

Chapter 1 39

1. Modelling anisotropic friction in the presence of 1D and 2D roughness 39

1.1. Anisotropic Lattice Spring Friction Model for 1D roughness (1D-ALSFM) 40

1.2. Particular cases 46

1.3. ALSFM for 1D general roughness 51

1.4. Extended ALSFM for 2D roughness (2D-ALSFM) 57

1.5. Preliminary conclusions 63

Chapter 2 65

2. Hierarchical HALSTM for 1D and 2D roughness 65

2.1. Introducing adhesion in the ALSFM 66

2.2. Introducing wear in the ALSFM 75

2.3. Hierarchical ALSFM 80

2.4. Coupling hierarchy and wear effects in ALSTM..... 86

2.5. Conclusions 87

Chapter 3 89

3. Modelling the ice friction of rough surfaces: an application of the 1D-ALSFM to experiments 89

3.1. Experimental procedure..... 92

3.2. Experimental results 94

3.3. Extended 1D-ALSFM to the ice friction 98

3.4. Results 102

3.5. Conclusions 110

Chapter 4 111

4. Friction of micro-patterned surfaces: experimental and numerical investigation 111

4.1. Bespoke setup for friction tests..... 113

4.2. Experimental results 117

4.3. Numerical simulations..... 123

4.4. Comparison between experimental results with numerical simulations..... 128

4.5. Conclusions 131

Chapter 5 133

5. Friction in silk fibres to increase toughness without losing strength.... 133

5.1. Sample preparation..... 136

5.2. Mechanical properties of silk fibres..... 137

5.3. Knot implementation is silk fibres..... 139

5.4. Estimation of toughness increase due to knots....142
5.5. Results....144
5.6. Discussion and conclusions....149
5.7. Supplementary information on silk tensile tests....152
Conclusions....157
Bibliography....161
Appendix....177
A. Synergistic effect of graphene nanoplatelets and carbon black in multifunctional EPDM nanocomposites....177
A.1. Experimental details....180
A.2. Results and discussion....183
A.3. Conclusions....193
A.4. References....194

List of Figures

- *Figure 1.1 a) Asperity model for anisotropic friction as reported in (Mróz and Stupkiewicz 1994). b) The asperity model for orthotropic friction as adopted for our model: the asperities can be asymmetric and can vary the slopes from top and bottom. c). By assuming a single spring, the equilibrium on the tilted plane is showed to obtain the reaction forces F_x and F_y in the global reference system. 41*
- *Figure 1.2 Field of model application: in order to have the normal force N > 0, μ_0 must be smaller than cotφ. This defines when the model is applicable (blue part). 43*
- *Figure 1.3 Particular cases: a) One flat surface sliding on a rough surface with symmetric wedge asperities. b) Two rough surfaces with the same symmetric wedge asperities. 46*
- *Figure 1.4 Coefficient of friction for different sliding directions (β) in the case of two wedge asperity surfaces. μ_0 is set equal to 0.3. 49*
- *Figure 1.5 a) Variation of the global coefficient of friction by assuming one flat upper surface and one lower rough surface with respect to wedge slopes and the direction of sliding. b) Focus on the first part of the function: for smaller asperities slopes, reliable values of global coefficient of friction are obtained. This behaviour highlights the field of application of the model, which is suitable for asperities with small angles. μ_0 is set equal to 0.3. 50*
- *Figure 1.6 a) Variation of the global coefficient of friction by assuming both rough surfaces surface with respect to wedge slopes and the direction of sliding. b) Focus on the first part of the function: for smaller asperities slopes, reliable values of global coefficient of friction are obtained. This behaviour highlights the field of application of the model, which is suitable for asperities with small angles. μ_0 is set equal to 0.3. 50*

- *Figure 1.7 a) Detail of a surface with 1D roughness (along x direction): we consider the force equilibrium at point P, P ∈ f(x) due to the spring interaction. To obtain each force contribution, in this case the tangent plane (π) in P is considered. b) Force decomposition on π is considered with respect to the global system xyz in P. β_0 identifies the direction of the sliding velocity vector v_0 on the π plane, tilted by φ from the xy plane, while v is the projected sliding velocity and β the projection of β_0 on the xy plane. 52*
- *Figure 1.8 Coefficient of friction for six case studies reported in the box for two derivable periodic surfaces. As in the previous case, the coefficients are calculated by assuming different direction of sliding (β). μ_0 is set equal to 0.3. 55*
- *Figure 1.9 Friction coefficient μ with respect to time (i.e. sliding distance if the sliding velocity is constant) for two 1D symmetric sinusoidal shaped asperities. The graph shows the evolution in time of the global coefficient of friction with respect to the local coefficient μ_0. The average values increase, by increasing the local coefficient of friction. At the same time, the sliding direction β strongly influences both the oscillations around the mean values and the mean values as well. With β = 90° no oscillations occur due to the shape of the surfaces, which are extruded along the y direction in the xy plane. 56*
- *Figure 1.10 a) 2D roughness characterizes both surfaces in contact. A set of longitudinal springs governs the interaction at the interface. Details of one surface with 2D roughness: we consider the force equilibrium at point P, P ∈ f(x,y) due to the spring interaction. To obtain each force contribution, the tangent plane (π) in P is considered. b) Force decomposition on π is considered with respect to the local system x'y'z' in P. To obtain the overall reactions in the global reference system xyz, the rotation matrix must be applied (α). β_0 identifies the direction of the sliding velocity vector v_0 on the π*

plane, tilted by φ from the x'y' plane, while v is the projected sliding velocity and β' the projection of β_0 on the x'y' plane. 58

- *Figure 1.11 Variation of the coefficient of friction between two 2D rough surfaces with respect to the direction of sliding β. The upper and lower surfaces are the same and with symmetric roughness, thus the coefficient of friction μ varies between 0° and 45°. The blue line shows how the coefficient of friction changes between 0° and 90°, with a step Δβ equal to 5°, while the red line is the friction coefficient obtained for smaller steps. μ_0 is set equal to 0.3.60*
- *Figure 1.12 Some of the analyzed surfaces for the 2D roughness. The wavelengths vary along x and y (no differences occur between upper and lower surfaces) and the friction behavior is studied, due to these variations in both wavelength and sliding direction. 61*
- *Figure 1.13 Changes in the friction coefficient by varying both wavelength in x and y directions (from λ = π to λ = 3π) and sliding direction β from 0° (a) then 45° (c) and finally 90°(b). As expected, a) and b) are symmetrical and show the maximum coefficient of friction for the smallest wavelengths and this trend is preserved in the direction of sliding. Instead, the minimum value is reached for the biggest wavelengths. With β equal to 45°, the coefficient of friction is symmetrical with respect to the middle values. μ_0 is set equal to 0.3. 62*
- *Figure 2.1 Some examples of hierarchical and biological surfaces, SEM images of the (a) taro plant (Colocasia esculenta), (b) parrot feather plant (Myriophyllum aquaticum), and (c)–(e) lotus plant (Nelumbo nucifera) at various scales (McCarthy et al. 2012). In (f) the Brassica oleracea is an example of hierarchical and fractal surface (web source). A surface for anisotropic friction is reported in (g), with an example of snake skin microstructure (Lampropeltis getula californiae)(Tramsen et al. 2018).*

Finally, a gecko's foot, with a focus on the hierarchical morphology that covers its skin (Liskiewicz et al. 2008). 66

- *Figure 2.2 A 2D schematization of half model in various situations in the presence of adhesion, with decreasing L from a) to d). a) All the springs are compressed and the normal load is equal to the sum of all the spring axial forces. b) If some springs are elongated and L is the applied normal load, the sum of the compressive forces is larger than the load. c) In case of no external load, the sum of tensile and compressive forces on the springs is zero. d) In the case of a tensile load some compressed springs still generate friction.* 68
- *Figure 2.3 Effect of adhesion between 1D rough surfaces. a) Variation of springs elongation in time, normalized by the function period T. The number of stretched springs depends on the normal load. For each circular dot in b), a curve in a) is obtained. In the reported case, until the ratio L/Lmax is major than 0.3, the springs are all compressed (blue line in a), corresponding to zero for each time interval). After that value, some springs are elongated, and lines from blue to red show when and how many springs display a tensile force. When the upper and lower surfaces are both described by the same function, and they are in phase, the number of elongated springs is described by lines with shades of blue, which refer to L>0. On the contrary, lines with shades of red describe the number of elongated springs once the load reduces and becomes tensile (L<0). b) Tangential force $R_{x,y}$ with respect to the applied normal load L. When no adhesion occurs, the coefficient of friction is the ratio between the two; on the contrary, when some springs become tensile,, a non-linear curve describes this relationship. In the presence of 1D roughness, adhesion does not affect the sliding with $\beta=90°$, because there is a swift transition from compressed to tensile springs along the y direction.* 70
- *Figure 2.4 Effect of adhesion between 2D rough surfaces. a) Tangential force $R_{x,y}$ with respect to the applied normal load L, both normalized with respect*

to the maximum load L_{max}. Without adhesion effects, the coefficient of friction is the ratio of the two; when adhesion occurs, a non-linear relationship describes this relationship. In the presence of 2D symmetrical roughness, adhesion equally affects x and y directions of sliding (blue line and yellow dashed line). An enlargement on the graph close to the origin is reported in b). With other sliding directions, e.g. β = 45°, the behaviour is without substantial differences from the previous cases. 72

- *Figure 2.5 Surface distribution of both compressed (blue) and tensile (yellow) springs when the relative motion between two 2D rough surfaces is along the x direction. Only the compressed springs contribute to the calculation of the frictional force. 74*
- *Figure 2.6 Surface distribution of compressed (blue) and tensile (yellow) springs when the sliding direction β is 45°. As stated before, only the compressed springs are assumed to contribute to obtaining the frictional force. These tensile or compressed zones are perpendicular to the sliding motion, thanks to the simmetry of the surface roughness. 74*
- *Figure 2.7 Surface distribution of compressed (blue) and tensile (yellow) springs when the relative motion between two 2D rough surfaces is along the y direction. 75*
- *Figure 2.8 a) A schematization of the surface levelling after the wear process. z_0 is the initial surface shape, while z_i is the surface profile after a certain time t_i. At the end of the wear mechanism, the surface will be flat. b) A scheme of the surface levelling in case of 1D wedge asperities; φ^0 is the initial surface tilt angle, while φ^i is the smoothed surface after a certain time t_i. c) Surface roughness changing in time. 77*
- *Figure 2.9 Variation in time of the friction coefficient between 2D rough symmetrical asperities. Five different directions of sliding (β) have been considered, from 0° to 45° (it has been demonstrated that from 45° to 90° the behavior is the same, due to symmetry. After a time equal to T_W the surfaces*

become flat, so that the friction coefficient tends to the local friction coefficient μ_0. μ_0 is set equal to 0.3. 78

- *Figure 2.10 a) Variation in time of the friction coefficient between two wedge asperities. Three different directions of sliding (β) have been considered. After a time equal to T_W the surfaces become flat, so that the friction coefficient tends to the local friction coefficient μ_0. b) Variation in time of the friction coefficient between two asperities with generic 1D roughness, again for three different directions of sliding (β). After a time equal to T_W, the surfaces become flat, causing the friction coefficient to assume the local friction coefficient μ_0. As observed in Figure 1.8, the generic 1D roughness gives a higher friction coefficient, with respect to the equivalent wedge case. 80*
- *Figure 2.11 How to model different levels of roughness. 82*
- *Figure 2.12 Hierarchical friction for 2D roughness. a) Variation of the friction coefficient between two symmetric self-similar hierarchical asperities. Three different directions of sliding (β) are considered.. b) Variation of the friction coefficient between two asymmetric self-similar hierarchical asperities. Two different directions of sliding (β) have been considered as a prof that, if the asperities are not symmetric, the frictional response varies in a more significant way with respect to β. 83*
- *Figure 2.13 Hierarchical friction. a) Variation of the friction coefficient between two sinusoidal hierarchical asperities. Three different directions of sliding (β) are considered. The theoretical prediction, which is the exact solution in case of wedge asperities, is reported (red curve). b) Variation of the friction coefficient between a sinusoidal hierarchical surface and a flat surface. Three different directions of sliding (β) are reported. The theoretical prediction, which is the exact solution in case of wedge asperities, is reported (red curve). Hierarchical friction. c) If the surfaces are modelled as hierarchical wedges, friction coefficient is the same as obtained from the*

power law. Also other directions of sliding (β) have been reported. d) Variation of the friction coefficient between hierarchical wedge asperities. Three different directions of sliding (β) have been considered. In this casetoo, the theoretical prediction perfectly matches the numerical results. 85

- *Figure 2.14 Variation of the global coefficient of friction as a function of wear and roughness levels. Every outer level is influenced by the inner one, so that wear induces a reduction of each global coefficient of friction associated to a certain level i. After a time equal to T_W the innermost level becomes flat, so that the coefficient of friction of each level at the end of this wear cycle tends to its local friction coefficient. Level 0 is the local coefficient of friction. 87*
- *Figure 3.1 Stribeck curve generalized for ice friction: the friction coefficient is a non-linear function of the sliding velocity (proportional to the thickness of lubricant (water). Three regimes are highlighted, due to different asperity interaction and increasing water layer thickness h. 90*
- *Figure 3.2 Optical microscopy image of an ice surface replica. The magnification shows the characteristic 120° angles formed by the grain boundaries at almost each cross. Etch pits are also visible. 92*
- *Figure 3.3 3D surface profile of the stainless-steel pins. a) Pin #1, which is characterized by the smoothest surfaces. b) Pin #2 and c) pin #3. 94*
- *Figure 3.4 Friction coefficient results obtained from the pin-on-disc tests at increasing sliding velocity. a) pin #1, (b) pin #2 and (c) pin #3. The tests have been performed at various temperatures from -2 °C to -17 °C. 96*
- *Figure 3.5 Schematic illustration of the contact between ice and steel pin. To compute the coefficient of local friction a number of contacts n of length b and width a is assumed. The sliding velocity is v. 99*
- *Figure 3.6 a) Schematic illustration of the contact between ice and steel pin and b) how it is converted into the 1D-ALSFM developed in Chapter 1. The*

interaction between ice and steel is modelled by a set of springs with only longitudinal compliance. 102

- *Figure 3.7 Best fits of the experimental data obtained for pin 1# with the 1D-ALSFM (red line) for all the tested temperatures. It is evident that the model is not able to predict pin 1# friction regime, due to the model hypotheses which assume the pin in a mixed lubrication regime. 105*
- *Figure 3.8 Best fits of the experimental data obtained for pin 2# with the 1D-ALSFM for all the tested temperatures (blue line represents the upper values for the coefficient of friction, while red line is for the lower values). 105*
- *Figure 3.9 Best fits of the experimental data obtained for pin 3# with the 1D-ALSFM for all the tested temperatures (blue line represents the upper values for the coefficient of friction, while red line is for the lower values). 106*
- *Figure 3.10 Correlation between the model surface and the bearing ratio curve (BRC). 107*
- *Figure 3.11 A comparison between fitted and estimated contact length a. These results show a good agreement between the fitted values of the contact length a with respect to the contact length obtained from the geometrical calculation. After this validation, it is possible to infer that the values provided from the fit are reliable values 108*
- *Figure 3.12 Comparison between the friction coefficient results obtained from the resin pin tests performed at -2°C (black dots) and the results from the steel pin #1 tests (red dots) performed at the same temperature. 109*
- *Figure 4.1 (A) Sample holder with a glued sample. (B) SEM image of a flat surface. (C) SEM image of sample A. (D) SEM image of sample B. (E) SEM image of sample C. (F) SEM image of sample S. (G) SEM image of sample S, enlargement of a single hole. These samples were tested along x and y directions. All scale bars are equal to 20 μm. 115*
- *Figure 4.2 A) Details of the custom built setup. A black flat polycarbonate surface is fixed to a tensile machine (a). A transparent sample holder (b) can*

slide on the polycarbonate surface, thanks to two inextensible wires (c), which are connected to the grip of the tensile machine. A frictionless roller transmits the imposed velocity from the machine to the sample holder (d). Each PDMS surface is anchored to the transparent support (e) and loaded with different known weights. B) Overview of the setup. 116

- *Figure 4.3 Examples of friction tests with the described setup; friction force (T) is normalized with respect to the peak value of the respective test, which corresponds to the static friction force (T_{max}): (A) Friction test for a flat PDMS surface . (B) Friction test for sample A. (C) Friction test for sample B. (D) Friction test for sample C. (E) Friction test for sample S, along x- and y-directions. All scale bars are equal to 20 μm. 118*
- *Figure 4.4 Experimental friction test results. Plots report the ratio between static and dynamic friction force (T) and the applied normal load (N) as a function of the normal pressure p (N/A_{th}). (A) Static friction coefficients of flat surfaces and samples A, B and C. (B) Dynamic friction coefficients of flat surfaces and samples A, B and C. (C) Static friction coefficients of samples S, along both x and y directions. (D) Static friction coefficients of samples S, along both x and y directions. 119*
- *Figure 4.5 Static friction force T as a function of the applied normal load (N): experimental data (blue circles), linear fit (red line), rescaled fit (yellow dotted line). (A) Flat surface; (B) A sample;(C) B sample; (D) C sample; (E) S sample - sliding along the x direction; (F) S sample - sliding along the y direction. 120*
- *Figure 4.6 Dynamic friction force T as a function of the applied normal load (N): experimental data (blue circles), linear fit (red line), rescaled fit (yellow dotted line). (A) Flat surface; (B) A sample;(C) B sample; (D) C sample; (E) S sample - sliding along the x direction; (F) S sample - sliding along the y direction. 121*

- *Figure 4.7 Comparison between the fitted parameters for the static coefficient of friction μ and $\tau 0$ with respect to the prediction by adopting Eq.(4.2). A linear fit of both the parameters show a decresing trend with decresing AF. 122*
- *Figure 4.8 Comparison between the fitted parameters for the dynamic coefficient of friction μ and $\tau 0$ with respect to the prediction by adopting Eq.(4.2). A linear fit of both the parameters show a decresing trend with decresing AF. 122*
- *Figure 4.9 A) Sketch of patterned surface, where the main sliding direction is set to $\alpha=0°$.B) Schematic of the 2D spring-block model with the notation used in the text. Mesh of the internal springs on the surface, the shear springs are not shown. C) Side view showing the slider moving at constant velocity v and the shear springs. D) Outputs of the numerical simulations, showing the evolution of the coefficient of friction in time. 126*
- *Figure 4.10 Numerical and experimental results of the static coefficient of friction. the ratio between the static friction force (T) and the applied normal load (N) as a function of the nominal pressure (p = N/A) is reported for all the case studies. (A) Flat surfaces; (B) A samples;(C) B samples; (D) C samples; (E) S samples - sliding along the x direction; (F) S samples - sliding along the y direction. All scale bars are equal to 20 μm. 129*
- *Figure 4.11 Numerical and experimental results of dynamic friction tests in term of the ratio between the static friction force (T) and the applied normal load (N) as a function of the nominal pressure (p = N/A) for all the case studies. (A) A samples;(B) B samples; (C) S samples - sliding along the x direction; (D) S samples - sliding along the y direction. All scale bars are equal to 20 μm. 130*
- *Figure 5.1 Our silkworm silk fibres were extracted from a) the cocoon as is, (the silkworm produces the cocoon to protect itself during the metamorphosis)*

or b) after the degumming process, where the sericin, a protein, is removed. Scale bars 1 cm. 135

- *Figure 5.2 a) A natural fibre of silk formed by two brins coated and bended together by a layer of sericin, removed after the degumming process. b) Cross section of a natural silk fibre. c) Cross section of a degummed silk fibre. Scale bars 10 µm.137*
- *Figure 5.3 a) A degummed silk fibre, provided with an optimized knot, spanning over a paper frame prepared for nanotensile testing. The knot, either single (STSK) or double (DTSK) turned slip knot, is characterized by two main parameters, the loop length, l_p, and the knot diameter, as shown in the zoomed view (b). 137*
- *Figure 5.4 Stress-strain curves derived from tensile tests carried out on single untreated baves (black line) and degummed fibres (green line), both showing significant variability. 138*
- *Figure 5.5 Gallery of knots implemented in single silk fibres. (a) SEM picture of the Noose with a schematic on top. (b) SEM picture of the Overhand Loop with a schematic on top. (c) SEM picture of the Chain Knot with two chains and a schematic on top. (d) SEM picture of the X-Knot with a schematic on top. Scale bar: 10 µm. 141*
- *Figure 5.6 (a) Stress-strain curve of an unknotted natural fibre with length l. (b) Stress-strain curve of a knotted natural fibre with length l and distance between its opposite ends l_0, which was extracted from a cocoon region adjacent to the unknotted fibre (a). The presence of the knot modifies the shape of the stress-strain curve (a), introducing a plastic-like plateau and leaving a final region (highlighted) almost corresponding to the stress-strain curve of the same fibre with unknotted configuration. The strain interval within this final region appears larger than in (a) since it is computed with respect to l_0 instead of l. 143*

- *Figure 5.7 Untightening mechanism of the (a) Noose, (b) Overhand Loop, (c) Chain Knot (in this schematic with two chains) and (d) X-Knot. When the fibre opposite ends are pulled apart, the loop is sucked into its closest chain until this is completely released, thus forcing the knot to collapse into a simple noose. If the fibre ends are pulled further apart, the noose loosens until the knot is completely untightened. On the contrary, the Overhand Loop becomes tighter as the fibre is pulled. In an X-knot, the fibre appears to be turned twice at the bottom of its loop. When its opposite ends are pulled apart, the turn closer to the loop tends to tie, causing friction against the fibre sliding, while the other one loosens. In this way, the knot can unfasten completely although a significant amount of energy can be dissipated.* *144*
- *Figure 5.8 (a) Stress-strain curves of natural and degummed silk fibres with optimized Noose or Overhand Loop slip knots. Comparison between the normalized stress-strain curves obtained for natural and degummed single silk fibres provided with optimized knots. Stress values are normalized with respect to fracture strength. Comparison between the stress-strain curves derived from samples with an X-Knot and a Chain Knot with either 2, 4 or 6 chains, respectively. Here, stress values are normalized with respect to the fracture stress of each fiber.* *148*
- *Figure 5.9 a) Unfastening mechanism of the Noose, which tends to loosen as the fiber ends are pulled apart. Such knot can always be released, even when extremely tight, as shown in the SEM image. b) Unfastening mechanism of the Overhand Loop, which tends to further tie as the fiber ends are pulled apart. Thus, if this knot is too tight at the beginning of the test, it cannot be released, as occurred in the natural silk fiber reported in the SEM image (b), which broke at the knot entrance. The sericin coating looks significantly damaged by friction. c) SEM image of a fiber with a Chain Knot with four chains visibly damaged by preparation, which caused superficial exfoliation. (d) SEM*

image of a fiber with a Chain Knot with six chains not uniformly tightened during preparation. Scale bars: 10 μm 150

- *Figure A.1 a) Raman spectra of GNPs. b) The data of FWHM with respect to 2D peak positions. 184*
- *Figure A.2 (a) Stress-strain curves of the prepared samples. (b) Modulus at different strains and maximum strength of the prepared samples. 185*
- *Figure A.3 Elongation at break of the prepared samples. 186*
- *Figure A.4 Dynamic and static coefficient of friction measured of the prepared samples. 187*
- *Figure A.5 Set-up of the impact test. The impact area is a metallic plate where the sample to be tested has been fastened to. The sample was hit by a percussion which excites the vibration. A shock accelerometer positioned in the back plate is thus excited and the response is recorded and digitalized via high performance data acquisition system. b) Peak acceleration measured by the accelerometer in the impact test of the prepared samples. 188*
- *Figure A.6 (a) Set up of the thermal conductivity measurements. (b) Thermal conductivity values as a function of the GNPs/CB content. 189*
- *Figure A.7 X-ray diffraction patterns of (a) EPDM nanocomposites with different GNPs/CB content and (b) CB, GNPs and neat EPDM. 190*
- *Figure A.8 FESEM images of the a) EPDM-6 and b) EPDM-7 samples. The arrows in Figure A.6 a) shows the CB agglomerates on a GNP sheet. The scale bars indicate 1 μm. 191*
- *Figure A.9 a) Total cylindrical volume of the EPDM-6 sample (348 micron in diameter and 360 micron in height); b) and c) Detail of segmented CT images showing the distribution of the graphite nanoplatelets and carbon black aggregates, respectively (scale bar is 50 microns). d) Detail of segmented CT images showing the whole distribution of the graphite nanoplatelets (in red) and carbon black aggregates (in blue indicated by the arrows) (scale bar is 50 microns). 192*

List of Tables

- *Table 3.1 Roughness parameters for the stainless-steel pins: average roughness (Ra), RMS slope (Rdq), skewness (Sk), kurtosis (Ku), fractal dimension (D) and contact angle (θc). 94*
- *Table 3.2 List of used symbols and their numerical values; i=1 for ice, i=2 for slider. The contact length a is calculated from data analysis in the next section. 101*
- *Table 4.1 Geometrical characteristics of considered samples 114*
- *Table 4.2 Results obtained from the fits following Eq. (4.1). 123*
- *Table 4.3 Adhesion terms expressed as force for unit surface deduced from experimental results for each sample. 127*
- *Table 5.1 Strength and toughness modulus (T_u) of unknotted control fibres. Strength, toughness modulus (T_k) and toughness modulus after unfastening (T_u') of fibres with the Noose and the Overhand Loop (O. L.) (the toughness modulus was computed considering a density of 1.4 g/cm3 (Pérez-Rigueiro et al. 2001)). For each knot topology, two sets of data are provided, corresponding to samples with average stress in the strain interval 0%-40% of their strain at break (i.e., friction stress) above or below the 8% of their strength. Such threshold value was considered as the minimum friction stress required for knots to be efficiently implemented. 145*
- *Table 5.2 Comparison (*) between the toughness increases and strength decreases provided by different knot topologies with respect to unknotted single silk fibres (average strength of 514 ± 103 MPa and average toughness modulus: 32 ± 14 J/g computed considering a density of 1.4 g/cm^3 [32]). 146*
- *Table 5.3 Raw silk fibers with single turned slip knot: Strength, average friction stress/strength over 0% - 40% of the strain at break, toughness*

modulus (T_k), toughness modulus after knot unfastening of knotted fibers (T_u'), toughness modulus of reference unknotted samples (T_u). 153

- *Table 5.4 Raw silk fibers with double turned slip knot: Strength, average friction stress/strength over 0% - 40% of the strain at break, toughness modulus (T_k), toughness modulus after knot unfastening of knotted fibers (T_u'). 154*
- *Table 5.5 Degummed silk fibers with single turned slip knot: Strength, average friction stress/strength over 0% - 40% of the strain at break, toughness modulus (T_k), toughness modulus after knot unfastening of knotted fibers (T_u'). 155*
- *Table 5.6 Degummed silk fibers with double turned slip knot: Strength, average friction stress/strength over 0% - 40% of the strain at break, toughness modulus (T_k), toughness modulus after knot unfastening of knotted fibers (T_u'). 156*
- *Table 5.7 Strength and toughness modulus of control raw silk unknotted fibers. 156*
- *Table 5.8 Strength and toughness modulus of control degummed silk unknotted fibers. 156*
- *Table A.1 Recipes of the rubber compounds (indicated in phr: parts per hundred of rubber). The %weight content of GNPs/CB is reported below the name of each sample. 181*

List of Papers

1) M.F. Pantano, A. Berardo, N. Pugno. Tightening slip knots in raw and degummed silk to increase toughness without losing strength. SCIENTIFIC REPORTS (2016), 6, 18222.

2) A. Berardo, M.F. Pantano, N. Pugno. Slip knots and unfastening topologies enhance toughness without reducing strength of silk fibroin fibres. INTERFACE FOCUS (2016), 6, 20150060.

3) L. Valentini, S. Bittolo Bon, M.A. Lopez-Manchado, R. Verdejo, L. Pappalardo, A. Bolognini, A. Alvino, S. Borsini, A. Berardo, N. Pugno. Synergistic effect of graphene nanoplatelets and carbon black in multifunctional EPDM nanocomposites. COMPOSITES SCIENCE AND TECHNOLOGY (2016), 128, 123-130.

4) A. Spagni, A. Berardo, D. Marchetto, E. Gualtieri, N. Pugno, S. Valeri. Friction of rough surfaces on ice: Experiments and modeling. WEAR (2016), 368-369, 258-266.

5) G. Salerno, A. Berardo, T. Ozawa, H. Price, L. Taxis, N. Pugno, I. Carusotto. Spin-orbit coupling in a hexagonal ring of pendula. NEW JOURNAL OF PHYSICS (2017), 19, 055001.

6) A. Berardo, G. Costagliola, S. Ghio, F. Bosia, N. Pugno. A coupled experimental-numerical study of friction of micro-patterned surfaces. To be submitted.

7) A. Berardo, N. Pugno. A model for hierarchical anisotropic friction, adhesion and wear. Under drafting.

Summary

Whenever two bodies are in contact and one is sliding against the other, a tangential force arises, opposed to the motion. This force is called *friction force*, and involves different mechanisms, such as asperity interactions, energy dissipation, chemical and physical alterations of the surface topography and wear (Greenwood and Williamson 1966; Persson et al. 2005; Popova and Popov 2015; Vakis et al. 2018). The friction coefficient is defined as the ratio between the friction force and the applied normal load. Despite this apparently simple definition, friction is a very complex phenomenon, which also involves several aspects at both the micro- and nano-scale, including adhesion and phase transformations (Nosonovsky and Bhushan 2008; Spagni et al. 2016; Valentini et al. 2016). Friction plays a key role in a variety of systems, and can be either enhanced (e.g. for locomotion) or minimized (e.g. in bearings), depending on the application.

Considering friction as a multiscale problem, an analytical model is herein proposed to describe friction in the presence of anisotropy, adhesion and wear between surfaces with hierarchical (e.g. self-similar) structures. This model has been developed starting from others in the literature (Mróz and Stupkiewicz 1994), extended to take into account adhesion, wear and hierarchy. This Anisotropic Lattice Spring Friction Model (ALSFM) has been implemented in a MATLAB code for the design of the tribological properties of hierarchical surfaces.

Such a model has been applied to describe the frictional behaviour between ice and steel and to assess the influence of the surface roughness.

Furthermore, it has been studied how a particular isotropic or anisotropic surface morphology (e.g., microholes of different shapes and sizes) can influence the static and dynamic friction coefficients with respect to its flat counterpart. In

particular, it has been proved that the presence of grooves on surfaces can decrease the friction coefficients and, thus, reduce wear and energy dissipation. Experimental tests were performed with a setup realized *ad hoc* and the results were compared with full numerical simulations by using codes developed in our group (Capozza and Pugno 2015; Costagliola, Bosia, and Pugno 2016, 2018).

Tough some applications require a reduction in sliding friction, others could require an increase in energy dissipation, e.g. to enhance toughness of microfibers. In particular, the applied method consists of introducing sliding frictional elements (sliding knots) (Pugno 2014) in biological (silkworm silk, natural or degummed) and synthetic fibres (Berardo, Pantano, and Pugno 2016; Bosia et al. 2016; Pantano, Berardo, and Pugno 2016). This procedure reproduces the presence of sacrificial bonds in molecules, which provides higher toughness to the molecular backbone, thanks to a hidden length that occurs after their breakage. A variety of slip knot topologies with different unfastening mechanisms have been investigated, including even complex knots usually adopted in the textile industry. The knots were made by the manipulation of fibres with tweezers and the resulting knotted fibres were characterized through nanotensile tests to obtain their stress-strain curve until failure. The presence of sliding knots strongly increases the dissipated energy per unit mass, without compromising the structural integrity of the fibre itself. Slip knots with optimized shape and size resulted in a significant enhancement of fibres toughness, up to 300-400% for natural silkworm silk fibres, without affecting their load bearing capacity.

Introduction

Tribology is the science of interacting surfaces in relative motion and of related subjects. The interactions that take place at the moving interface define the friction, wear, and lubrication behaviour. Since friction occurs in everyday life, understanding the nature of these interactions at micro and nano scale may solve the technological problems associated with the interfacial phenomena. This constitutes the essence of tribology. In addition, tribological problems must be considered with a multidisciplinary approach, due to the presence of several mechanisms, such as mechanics, energy dissipation, adhesion, physical and chemical alterations of the surface, materials science third body lubrication, thin films and coating, phase transitions, wear (Archard 1953; Greenwood and Williamson 1966; Makkonen 1997; Persson et al. 2005; Popova and Popov 2015; Shu 1986; Vakis et al. 2018). In the field of tribology, some considerable progress has been recently achieved since the frictional behaviour of many components in industrial and everyday applications is of great importance to their functionality, from a macroscopic to a microscopic point of view.

In particular, frictional surfaces can be also found on different scales in nature, with developed efficient solutions to minimise or maximise friction, depending on the needs. For example, ultra low friction is achieved in lubricated systems as synovial joints while ultra-high friction or even controlled adaptable friction can be found in the gecko feet, providing hierarchical structures with maximum adhesion (Baum et al. 2014; Boesel et al. 2010; Filippov and Gorb 2013; Jin and Dowson 2013; Liskiewicz, Morina, and Neville 2008). The study of these optimized structures and materials is of great interest for the development of nature-based solutions from an engineering point of view.

For these reasons, the main goals of my PhD research are to acquire further knowledge in the wide field of tribology. The results aim to pave the way for

further investigations on how to increase and/or reduce friction to achieve optimized frictional and mechanical properties. My interests are the description of friction in the presence of rough surfaces in order to highlight the effects of anisotropic friction and tunable properties. Moreover, adhesion, wear, lubrication and hierarchical structures are also objects of this study to obtain a general overview of the main aspects related to tribology and bio-tribology. After a numerical part and model developing, experimental analyses in two different systems are shown to provide examples of how to exploit friction, by taking inspiration from nature.

State of the art

Although it has been studied for centuries, friction still includes various open questions, due to the many aspects occurring at the interface between bodies in relative motion.

Leonardo da Vinci first proposed the "laws of dry friction", then reformulated and collected by Amontons in the so-called four "laws of friction", which are the basic qualitative concepts related to this very complex phenomenon, even if in a qualitative way (Dowson 1979; Popova and Popov 2015).

Despite their simplicity, these laws resulted in the Amontons-Coulomb constitutive laws of friction (Coulomb 1821; Bo N. J. Persson 2000; Stewart Gillmor 1971). They can be summarized as follows:

- The friction resistance increases or decreases proportionally to the applied pressure;
- The friction coefficient (which is the ratio between the friction force and the normal load) is independent of sliding velocity, contact area and the surface roughness (Coulomb 1821; B N J Persson 2000; Popova and Popov 2015; Stewart Gillmor 1971).

Coulomb stated that "*Friction and cohesion are not active forces like gravity, but only passive forces*"(Popova and Popov 2015), highlighting that they arise only in

the presence of an incipient relative motion (static friction force) or during the sliding (dynamic friction force). He also generalized the relationship between the tangential force and the applied load, by introducing a cohesive contribution, independent of the normal pressure.

In terms of stresses, it is expressed as follows:

$$\tau = \tau_0 + \mu\sigma_N$$

where τ is the frictional stress, τ_0 is the cohesive component, σ_N is the normal pressure and μ is the internal coefficient of friction.

The Coulomb's law is still considered the basis for the description of dry friction in classical mechanics, even though recent studies have proved that some deviations may occur (Capozza and Pugno 2015; Carbone and Bottiglione 2008, 2011; C Caroli and Nozières 1998). For example, it does not consider the presence of anisotropy, i.e. when the friction force depends on the direction of sliding, or how the normal load depends on the real contact area.

Over the years, analytical models have been introduced to study the complicated problem of friction. One of the main contact theories was introduced by Hertz (Hertz 1882), which paved the way for the development of more recent models for contact mechanics, such as the one proposed by Greenwood and Williamson (GW) (Greenwood and Williamson 1966), the so called *multi-asperity model* and related studies by Majumdar and Bhusham (Bhushan and Majumdar 1992; Majumdar and Bhushan 1991), or alternative solutions, such as Persson's theory (Bo N. J. Persson 2000; Persson 2001, 2006). They presented different approaches to compute the response of a rough surface in contact with a flat substrate, due to a normal load. Greenwood and Williamson developed the Archard's studies, assuming a surface formed by *n* elastic spherical caps with same radii but different heights and provided the solution for the contact area after pressing this multi-asperity surface against a rigid plane (Archard 1953; Greenwood and Williamson 1966; Whitehouse and Archard 1970). They found that the area of real contact, usually smaller than the apparent contact area (B N J Persson 2000), is

proportional to the load, while the average size of micro contacts is independent of the load. Indeed, when the load increases, new contact spots are generated. On the contrary, Persson referred to surface roughness by defining the power spectral density of the undeformed rough surface and studied the contact mechanics between this rough rigid surface and a semi-infinite elastic solid.

Other models have been developed during the years to study the interaction between the asperities of rough surfaces in contact. The one proposed by Caroli and Nozières (C. Caroli and Nozières 1998) studied velocity independent friction in a dry system and found that it is generated by hysteretic behaviour, while the elastic interactions between the asperities play a minor role in solid friction of multicontact interfaces. Mroz and Stupkiewicz also reported a friction model for anisotropic friction, which is the starting point for the development of the model I present within this work. Further details are pointed out in Chapter 1.

An overview about tribological modelling and theories has been recently published (Vakis et al. 2018), which compares multiple theories and shows different approaches to this intriguing topic.

Overview

Since friction depends on numerous factors, my research activity has been organized into two main parts.

In the first part, an analytical model for anisotropic dynamic friction has been introduced, which directly connects roughness with the friction coefficient and extends the study presented in (Mróz and Stupkiewicz 1994). Then, its adaptability has been enhanced by introducing one-dimensional and two-dimensional roughness (1D and 2D Analytical Lattice Spring Friction Model), wear as a process which modifies the contact surface, adhesion and hierarchy. The model is based on the local validity of the classical Coulomb's law (B N J Persson 2000) and considers parallel springs to simulate the interaction between rough surfaces.

I implemented a mechanism simulating wear, which modifies the roughness profile, according to Archard's law (Archard 1953). As a first approach, wear smooths the asperities. Then, adhesion has been modelled as a tensile force, which increases its effects during surfaces separation. Since nature provides optimized surfaces with hierarchical structures, I extended the model to describe surfaces using *n* levels of hierarchy in order to study their contribution to the frictional response of the system (Nosonovsky and Bhushan 2008; Pugno, Yin, et al. 2013). This has also been applied to the complex topic of ice friction, introducing lubrication and phase changes. Over a century of scientific research on the sliding friction of ice has not been sufficient to find an exhaustive explanation for the tribological behaviour of frozen water. It has been noticed that ice shows different friction regimes, but a detailed description of all the different processes occurring at the interface, including the effect of surface roughness of both the ice and the sliding material, was still missing.

For this reason, in my thesis, the effects of surface morphology on the friction of steel/ice interfaces are discussed. Different degrees of random roughness are introduced on the steel surface and the friction coefficient is determined over a wide range of temperature and sliding velocities. The correlation between the surface roughness, the lubrication regime and the friction coefficient variation is described, by applying the 1D-ALSFM.

The second part of this thesis is devoted to experimental activities, as a bio-inspired approach to reduce friction in dry contacts, thanks to micro-textured surfaces, and a mechanical procedure to enhance the toughness of one-dimensional materials (i.e. fibres), taking advantage of friction on the fibre lateral surface.

Indeed, since friction depends on surface topography as well as on material mechanical parameters, new possibilities have emerged to control frictional properties by exploiting microscale surface patterning with sub-micrometer-precision fabrication techniques. In order to design surfaces with the desired

characteristics, it is important to understand this relationship and to predict the final behaviour. In this thesis, I investigated with a custom-made setup how micropatterns affect the friction coefficient of surfaces and then verified the reliability of one numerical model, i.e. the 2D Spring Block model (Costagliola et al. 2016, 2018). In particular, experimental tests on various polymer substrates with isotropic and anisotropic patterns have been performed and compared to the corresponding numerical predictions for static and dynamic friction. In this experimental part, I could not apply my model for hierarchical surfaces due to its limits, which to date can not describe friction on surfaces with discontinuities (e.g. holes or pillars).

However, friction could also be enhanced to improve the contacts between bodies or to dissipate more energy during the sliding. For this reason, a mechanical method is introduced to increase the energy dissipation of one-dimensional elements (silkworm silk fibres). The combination of high strength and high toughness is a desirable feature that structural materials should display. While in the past engineers were forced to reach a compromise, new toughening strategies are available. In this thesis, I reported my study on one of such strategies, which requires no chemical treatment, but only the implementation of slip knots with optimized shape and size in the chosen material fibres. Knots are fascinating topological elements, which can be found in both natural and artificial systems. In particular, a variety of slip knot topologies with different unfastening mechanisms has been investigated, including complex knots usually used in the textile industry and their efficiency in enhancing toughness of silk fibres has been reported. Potential knotted structures have been exploited to artificially increase the toughness of silkworm, thanks to the friction involved during the unfastening process. This method reproduces at the microscale the same toughening function, which sacrificial bonds have in highly coiled macromolecules. As the breakage of weak bonds (i.e., sacrificial bonds) reveals a hidden length in macromolecules, which can be further stretched without breaking their backbones, the unfastened

knots in our samples provided silk fibres with additional length, which can thus be further elongated before failure.

Accordingly, this thesis is organised as follows: in Chapter 1, I introduce the analytical Anisotropic Lattice Spring Friction Model, starting from the one-dimensional description and then exploiting it to the two-dimensional surface roughness.
In Chapter 2, I introduce multiple effects related to dry friction phenomena as the presence of adhesion, sliding wear and hierarchy, providing an overall description of a typical tribological system.
In Chapter 3, I report a study in collaboration with the University of Modena and Reggio Emilia relative to the ice friction. Both experiments and analytical modelling are described and the aforementioned 1D-ALSFM is applied to correlate the roughness of surfaces to the friction behaviour in different regimes.
In Chapter 4, surface textures are analysed from an experimental point of view, then the results are applied to validate the spring-block model developed in collaboration with the University of Turin (Costagliola et al. 2018).
Finally, in Chapter 5, the experimental procedure of toughness enhancement through friction is proposed. I describe the method, the adopted material and main results, also reported in (Berardo et al. 2016; Pantano et al. 2016).
An additional related work is presented in Appendix, in which I performed tribological tests on Ethylene-propylene-diene termopolymer (EPDM) rubber based nanocomposites containing carbon black (CB), graphene nanoplatelets (GNPs) and mixtures of the two fillers, realized by University of Perugia. This work proposes the mechanical and thermal analysis of these composites.

Chapter 1

1. Modelling anisotropic friction in the presence of 1D and 2D roughness

Anisotropy in tribology can arise due to anisotropy of the surface roughness (e.g. textured surfaces, biological/bioinspired surfaces) or of the materials in contact (e.g. composites, crystals). The micromechanical modelling of friction anisotropy is a useful approach to study the interactions at the microscale and then to provide the overall behaviour at the macroscale. However, only few micromechanical models for anisotropic friction have been developed through the years, as the model for rubber friction (Carbone et al. 2009) and the model developed by Mroz and Stupkiewicz (Mróz and Stupkiewicz 1994). The first one assumes anisotropy due to orientation-dependent hysteretic contributions, while the second describes the contact between two surfaces (one represented by a parallel rigid wedge asperities and the other one flat) thanks to a set of longitudinal springs, which can deform only in the vertical direction. The Coulomb's friction law is assumed to be valid for local contacts.

Consistent with this last statement, I propose an analytical model, developed from the asperity model described in (Mróz and Stupkiewicz 1994), which is extended in this Chapter for general one-dimensional (1D) roughness and adapted to two-dimensional (2D) roughness (a simplified version of the presented model has already been applied in Spagni et al. 2016 and described in Chapter 3). For 1D roughness, a function of one variable is defined, in the form $z = f(x)$, while for 2D roughness, it is assumed that z depends on two variables, as $z = f(x,y)$.
In particular, in this Chapter, I have studied the interaction between two surfaces with a generic roughness in order to derive the expression of the global friction

force and the dynamic coefficient of friction. Their interaction is governed by a set of longitudinal springs to model the elastic forces acting between the surfaces. The analytical model is firstly proposed for two wedge surfaces, considering the effects of different geometries and direction of sliding. Secondly, surface roughness is described by continuous and derivative periodic functions for 1D and finally 2D asperities, to obtain how the general dynamic friction coefficient depends on these parameters. Finally, some case studies and their results are proposed and further discussed.

The presented model describes the interactions between rough surfacesduring the sliding, assuming that the two contact bodies are already in relative motion, without considering the static friction force.

Indeed, in this approach, attention is given to how roughness influences the dynamic friction forces, since continuous sliding for a long time is one of the main causes of wear and surface alterations. In addition, many industrial analyses of friction and wear on mechanical components are performed referring to the dynamic regime (Antoni et al. 2007; Bistac and Galliano 2005; Colbeck 1988; Spagni et al. 2016; Xing et al. 2017), thus this is why I primary focus on it. Some changes can be implemented within the model to extend its predictions also on the static phase; however, these are not object of this thesis.

1.1. Anisotropic Lattice Spring Friction Model for 1D roughness (1D-ALSFM)

The model described in (Mróz and Stupkiewicz 1994) considers two contacting surfaces as reported in Figure 1.1 a, in which their interaction is described by a set of longitudinal springs, with constant stiffness equal to k. This previous model assumes that one surface has long wedge-shaped asperities, while the other is flat, with attached isotropically distributed springs. When one surface is moving against the other, the springs deform and slide on the rough surface.

In this extended model, first of all, I changed the initial configuration, by assuming two rough surfaces. To detect this double roughness effect, the springs slide on both the upper and lower surface, being attached half to the lower surface and the other half to the upper surface respectively (Figure 1.1 b). This configuration allows the model to distinguish the coefficient of dynamic friction in the presence of two rough surfaces from the one of rough-flat contacts.

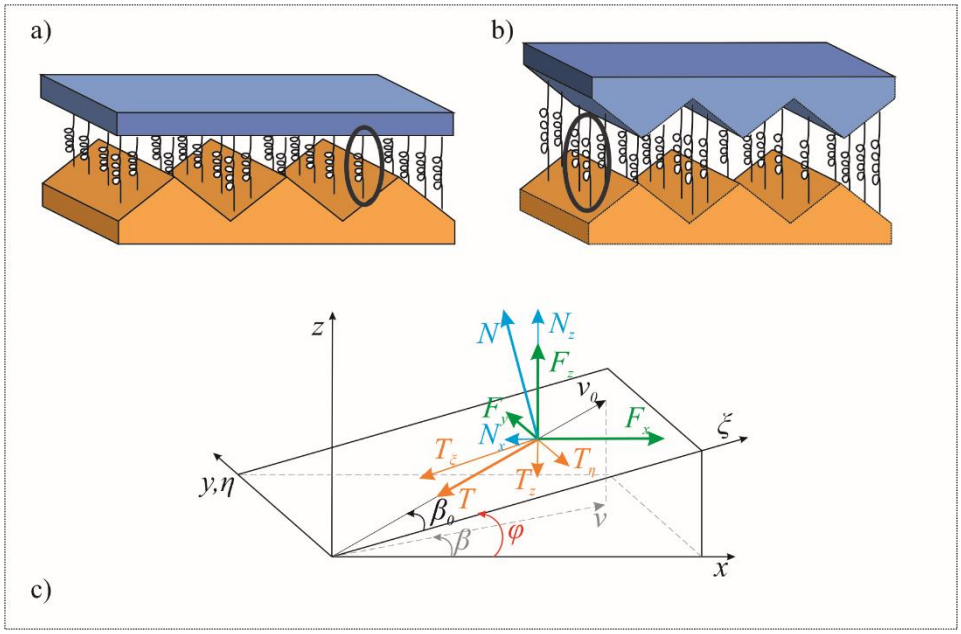

Figure 1.1 a) Asperity model for anisotropic friction as reported in (Mróz and Stupkiewicz 1994). *b) The asperity model for orthotropic friction as adopted for our model: the asperities can be asymmetric and can vary the slopes from top and bottom. c). By assuming a single spring, the equilibrium on the tilted plane is showed to obtain the reaction forces F_x and F_y in the global reference system.*

Firstly, the equilibrium of a single spring at point P on the tilted plane is considered, as reported in Figure 1.1 c. The spring length is equal to l_P, while the rest length is l_0. The sliding velocity on the asperity is identified by v_0, a vector in the *xy* plane. The direction of sliding is expressed by β_0, which can vary from 0° to 90°.

Due to its length variation, the single spring generates an elastic force, expressed as follows:

$$F_z(P) = uk_c > 0 \tag{1.1}$$

in case of compression, where $l_0 - l_P = u$.

The normal force *N* is the force perpendicular to the asperity (tilted by an angle $\varphi = \varphi_1$ with respect to the *xy* plane), and the tangential force *T* is the friction force, equal to $T = \mu_0 N$, where μ_0 is the local dynamic coefficient of friction. These forces are in equilibrium with the reaction forces F_x and F_y on the *xy* plane and by F_z in the vertical direction. From the equilibrium, the following equations are obtained:

$$F_z = N\cos\varphi_1 - T_\xi \sin\varphi_1 \tag{1.2}$$

$$F_x = N\sin\varphi_1 - T_\xi \cos\varphi_1 \tag{1.3}$$

$$F_y = T\sin\beta_0 \tag{1.4}$$

Where $T_\xi = T\cos\beta_0$ and $\tan\beta_0 = \tan\beta\cos\varphi_1$.

Referring to a generic plane tilted by any angle φ_1, from Eq. (1.2) to (1.4) the expression for *N* is obtained:

$$N = \frac{ku}{\cos\varphi - \dfrac{\mu_0 \tan\varphi_1 \cos\beta}{\sqrt{1+\tan^2\varphi_1\cos^2\beta}}} \tag{1.5}$$

The denominator must be different from zero, leading to $\varphi_1 \neq \frac{\pi}{2}$ and $\mu_0 \neq \cos\varphi_1$.

If F_z is a compressive force, it means $ku \geq 0$ and $\cos\varphi_1 - \frac{\mu_0 \tan\varphi_1 \cos\beta}{\sqrt{1+\tan^2\varphi_1\cos^2\beta}} > 0$.

This means that $l_0 - l_P$ is positive and that the local coefficient of friction μ_0 must be smaller than $\cot\varphi_1$. To satisfy Eq. (1.5), the more the material displays sharp roughness, the more the local friction coefficient must be small. In particular, for φ equal to 45°, μ_0 has to be minor than 1. From a physical point of

view, this implies that the model is suitable for elastomers, which usually display dynamic coefficient of friction around 1-2 (He, Chen, and Jane Wang 2008; Johnston et al. 2014; Rand and Crosby 2009; Valentini et al. 2016), until they show a smooth roughness (Figure 1.2).

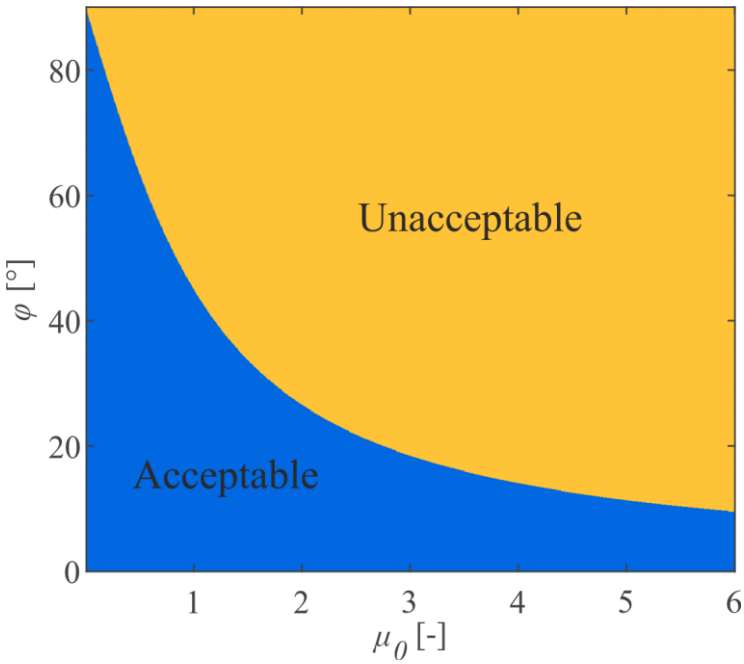

Figure 1.2 Field of model application: in order to have the normal force N > 0, μ_0 must be smaller than cotφ. This defines when the model is applicable (blue part).

From from Eq. (1.2) to (1.5)(1.4), the reaction forces acting in *x* and *y* directions are:

$$F_x = F_z \frac{\sin\varphi_1 \sqrt{1+\tan^2\varphi_1 \cos^2\beta} + \mu_0 \cos\beta}{\cos\varphi_1 \sqrt{1+\tan^2\varphi_1 \cos^2\beta} - \mu_0 \tan\varphi_1 \cos\beta} \tag{1.6}$$

$$F_y = F_z \frac{\mu_0 \sin\beta}{\cos\varphi_1 \sqrt{1+\tan^2\varphi_1 \cos^2\beta} - \mu_0 \tan\varphi_1 \cos\beta} \tag{1.7}$$

For simplicity, to recall the reaction forces F_x and F_y, the following expression are used:

$$F_x = F_z H_x(\mu_0, \varphi_1, \beta) \tag{1.8}$$

$$F_y = F_z H_y(\mu_0, \varphi_1, \beta) \tag{1.9}$$

where H_x and H_y include the contributions of the sliding direction β and the geometry, i.e. asperity slopes. When a single spring is considered, H_x and H_y are constant, until the spring slides on the plane tilted by φ_1 with the same orientation. To pass from a single spring interaction to the overall elastic response, a certain number n of springs is considered between two wedge asperities, formed byplanes tilted by φ_1, φ_2, φ_3, φ_4 respectively, with respect to the xy plane.

Since the average spring displacement is equal to $\frac{\sum_i^n \Delta l_i}{n}$, the average normal (elastic) force is $R_z = \frac{k\sum_i^n \Delta l_i}{n} = \frac{\sum_i^n k\Delta l_i}{n} = \frac{\sum_i^n F_z^i}{n}$ (thanks to the same spring stiffness). If the whole asperity is considered, the average normal elastic force R_z (in the z-direction) is the sum of the average elastic forces generated by the spring compression on each tilted plane. The average elastic forces are also weighted by their area of competence, thanks to the introduction of ψ and δ. The coefficient ½ remembers that the springs are fixed half on the upper and half on the lower surfaces.

$$R_z = \frac{1}{2}\frac{\psi}{1+\psi}R_z^{(1)} + \frac{1}{2}\frac{1}{1+\psi}R_z^{(2)} + \frac{1}{2}\frac{\delta}{1+\delta}R_z^{(3)} + \frac{1}{2}\frac{1}{1+\delta}R_z^{(4)} \tag{1.10}$$

$$\psi = \frac{\tan\varphi_2}{\tan\varphi_1} \qquad \delta = \frac{\tan\varphi_4}{\tan\varphi_3}$$

$R_z^{(1)}$(average normal force, acting on the tilted plane by φ_1), $R_z^{(2)}$(average normal force, acting on the tilted plane by φ_2), $R_z^{(3)}$(average normal force, acting on the tilted plane by φ_3) and $R_z^{(4)}$(average normal force, acting on the tilted plane by φ_4). In case of various wedge (i.e. triangular) asperities, these weights might be different, depending on the wedge slopes.

In this case, same expressions for the reaction forces R_x and R_y are obtained:

$$R_x = \frac{1}{2}\frac{\psi}{1+\psi}R_z^{(1)}H_x(\mu_0,\varphi_1,\beta) + \frac{1}{2}\frac{1}{1+\psi}R_z^{(2)}H_x(\mu_0,-\varphi_2,\beta)$$

$$+\frac{1}{2}\frac{\delta}{1+\delta}R_z^{(3)}H_x(\mu_0,\varphi_3,\beta) + \frac{1}{2}\frac{1}{1+\delta}R_z^{(4)}H_x(\mu_0,-\varphi_4,\beta) \qquad (1.11)$$

$$R_y = \frac{1}{2}\frac{\psi}{1+\psi}R_z^{(1)}H_y(\mu_0,\varphi_1,\beta) + \frac{1}{2}\frac{1}{1+\psi}R_z^{(2)}H_y(\mu_0,-\varphi_2,\beta)$$

$$+\frac{1}{2}\frac{\delta}{1+\delta}R_z^{(3)}H_y(\mu_0,\varphi_3,\beta) + \frac{1}{2}\frac{1}{1+\delta}R_z^{(4)}H_y(\mu_0,-\varphi_4,\beta) \qquad (1.12)$$

Finally, by computing the resulting tangential force on the *xy* plane, the global friction coefficient μ is equal to:

$$\mu = \frac{R_{x,y}}{R_z} \qquad (1.13)$$

If $\beta = 0$ the sliding motion is only in x direction, $\mu_y = 0$ and

$$\mu = \mu_x = \frac{R_x}{R_z} \qquad (1.14)$$

$$\mu_x = \frac{\frac{1}{2}\frac{\psi}{1+\psi}R_z^{(1)}\frac{\mu_0+\tan\varphi_1}{1-\mu_0\tan\varphi_1} + \frac{1}{2}\frac{\delta}{1+\delta}R_z^{(3)}\frac{\mu_0+\tan\varphi_3}{1-\mu_0\tan\varphi_3}}{R_z} +$$

$$+\frac{\frac{1}{2}\frac{1}{1+\psi}R_z^{(2)}\frac{\mu_0-\tan\varphi_2}{1+\mu_0\tan\varphi_2} + \frac{1}{2}\frac{1}{1+\delta}R_z^{(4)}\frac{\mu_0-\tan\varphi_4}{1+\mu_0\tan\varphi_4}}{R_z}$$

On the contrary, if $\beta = \frac{\pi}{2}$, $\mu_x = 0$ and

$$\mu = \mu_y = \frac{R_y}{R_z} \qquad (1.15)$$

$$\mu_y = \frac{\frac{1}{2}\frac{\psi}{1+\psi}R_z^{(1)}\frac{\mu_0}{\cos\varphi_1} + \frac{1}{2}\frac{\delta}{1+\delta}R_z^{(3)}\frac{\mu_0}{\cos\varphi_3} + \frac{1}{2}\frac{1}{1+\psi}R_z^{(2)}\frac{\mu_0}{\cos\varphi_2} + \frac{1}{2}\frac{1}{1+\delta}R_z^{(4)}\frac{\mu_0}{\cos\varphi_4}}{R_z}$$

1.2. Particular cases

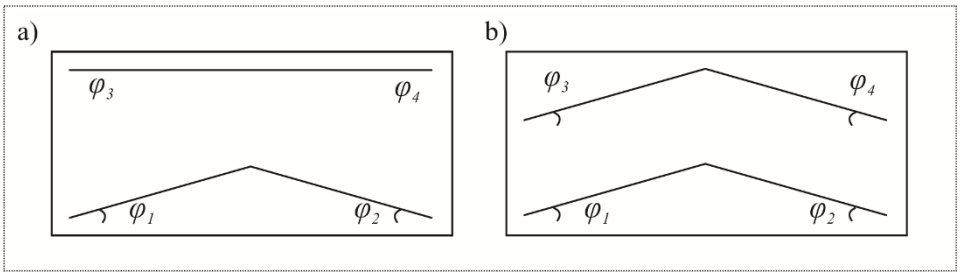

Figure 1.3 Particular cases: a) One flat surface sliding on a rough surface with symmetric wedge asperities. b) Two rough surfaces with the same symmetric wedge asperities.

- Case 1: $\varphi_1 = \varphi_2 = \varphi$, $\varphi_3 = \varphi_4 = 0$ and $\psi = \delta = 1$ (Figure 1.3 a)

This case is simplified when $\beta = 0$, so that the sliding motion is only in *x* direction, $\mu_y = 0$ and μ_x becomes:

$$\mu_x = \frac{\frac{1}{4}R_z^{(1)}\frac{\mu_0 + \tan\varphi}{1-\mu_0\tan\varphi} + \frac{1}{4}R_z^{(3)}\mu_0 + \frac{1}{4}R_z^{(2)}\frac{\mu_0 - \tan\varphi}{1+\mu_0\tan\varphi} + \frac{1}{4}R_z^{(4)}\mu_0}{R_z}$$

$$= \frac{\mu_0\left(2 - \sin^2\varphi\,(1+{\mu_0}^2)\right)}{2\left(1 - \sin^2\varphi\,(1+{\mu_0}^2)\right)} \qquad (1.16)$$

The contributions of the upper and lower surfaces are different, due to their roughness (or flatness). In the case of a flat surface, the reaction forces are equal to the tangential forces, since *N* is equal to F_z.

On the contrary, if β = 90°, the sliding motion is along *y* direction and it means that $\mu_x = 0$ and

$$\mu_y = \frac{\frac{1}{4}R_z^{(1)}\frac{\mu_0}{\cos\varphi} + \frac{1}{4}R_z^{(2)}\frac{\mu_0}{\cos\varphi} + \frac{1}{4}R_z^{(3)}\mu_0 + \frac{1}{4}R_z^{(4)}\mu_0}{R_z} = \frac{1}{2}\mu_0\left(\frac{1}{\cos\varphi} + 1\right) \quad (1.17)$$

Although these particular cases could seem very similar to the ones reported in (Mróz and Stupkiewicz 1994), slightly different values are obtained, as reported in Eq. (1.16) and (1.17). This is due to the different initial hypotheses. In particular, since the springs are fixed half on the lower surface and half on the upper surface, so that the average vertical force R_z is the mean of both upper and lower elastic forces, as in Eq. (1.10). On the contrary, in (Mróz and Stupkiewicz 1994) R_z was the mean of the elastic forces acting only on the lower surface, while the upper one does not contribute, resulting in different tangential forces. Thus, introducing in the ALSFM the same assumptions, the final values are the following:

$$R_z = \frac{\psi}{1+\psi}R_z^{(1)} + \frac{1}{1+\psi}R_z^{(2)} \quad (1.18)$$

$$\mu_x = \frac{\frac{1}{2}R_z^{(1)}\frac{\mu_0 + \tan\varphi}{1-\mu_0\tan\varphi} + \frac{1}{2}R_z^{(2)}\frac{\mu_0 - \tan\varphi}{1+\mu_0\tan\varphi}}{R_z} = \frac{\mu_0}{1-\sin^2\varphi\,(1+{\mu_0}^2)} \quad (1.19)$$

$$\mu_y = \frac{\frac{1}{2}R_z^{(1)}\frac{\mu_0}{\cos\varphi} + \frac{1}{2}R_z^{(2)}\frac{\mu_0}{\cos\varphi}}{R_z} = \frac{\mu_0}{\cos\varphi} \quad (1.20)$$

Where Eq. (1.19) refers to the global coefficient of friction when β = 0° and the sliding occurs along the *x*-direction while Eq. (1.20) refers to the global coefficient of friction when β = 90° and the sliding occurs along the *y*-direction. Eq. from (1.18) to (1.20) are obtained by assuming that only one surface

contributes to the calculation of the global coefficient of friction and the results are the same as reported in (Mróz and Stupkiewicz 1994).

Case 2: $\varphi_1 = \varphi_2 = \varphi_3 = \varphi_4 = \varphi$ and $\psi = \delta = 1$ (Figure 1.3 b)

This case is simplified when $\beta = 0$, the sliding motion occurs in *x* direction, $\mu_y = 0$ and:

$$\begin{aligned} \mu_x &= \frac{\frac{1}{4}R_z^{(1)}\frac{\mu_0 + \tan\varphi}{1 - \mu_0\tan\varphi} + \frac{1}{4}R_z^{(3)}\frac{\mu_0 + \tan\varphi}{1 - \mu_0\tan\varphi} + \frac{1}{4}R_z^{(2)}\frac{\mu_0 - \tan\varphi}{1 + \mu_0\tan\varphi} + \frac{1}{4}R_z^{(4)}\frac{\mu_0 - \tan\varphi}{1 + \mu_0\tan\varphi}}{R_z} \\ &= \frac{\mu_0}{1 - \sin^2\varphi\,(1 + {\mu_0}^2)} \end{aligned} \tag{1.21}$$

On the contrary, if $\beta = 90°$, $\mu_x = 0$ and

$$\mu_y = \frac{\frac{1}{4}R_z^{(1)}\frac{\mu_0}{\cos\varphi} + \frac{1}{4}R_z^{(3)}\frac{\mu_0}{\cos\varphi} + \frac{1}{4}R_z^{(2)}\frac{\mu_0}{\cos\varphi} + \frac{1}{4}R_z^{(4)}\frac{\mu_0}{\cos\varphi}}{R_z} = \frac{\mu_0}{\cos\varphi} \tag{1.22}$$

The coefficients found in Case 1 are smaller than in Case 2. This is reasonable, because Case 2 considers both the surfaces rough, thus, if one is flat (Case 1), there is a lower contribution to enhance the global friction coefficient.

In Case 2, when the lower and upper surfaces are defined by the same functions, the total elastic force is equally shared and all the tangential forces associated to each spring are influenced by the same roughness. This configuration refers to the one of (Mróz and Stupkiewicz 1994) and the same results are obtained.

The behaviour of the global coefficient of friction is reported in Figure 1.4, where we analysed six different roughness configurations with respect to the influence of the sliding direction (β). The direction of sliding non-linearly modifies the coefficient of friction μ.

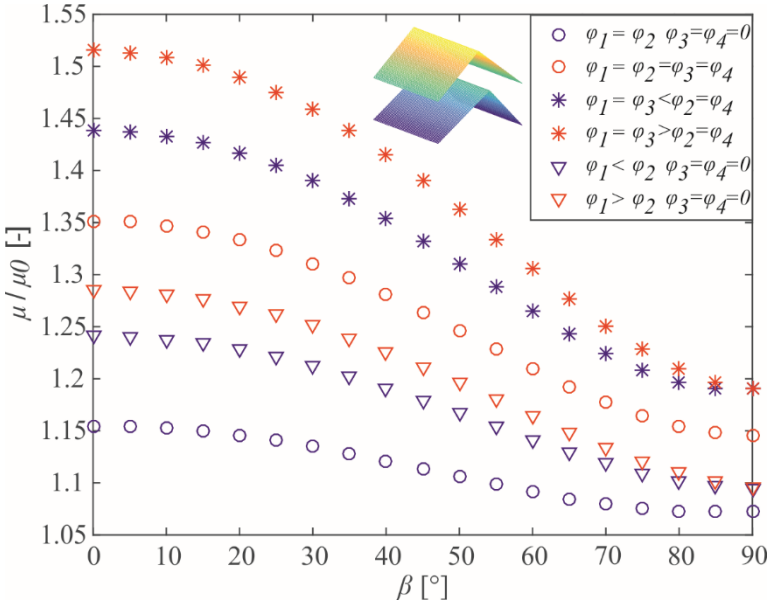

Figure 1.4 Coefficient of friction for different sliding directions (β) in the case of two wedge asperity surfaces. μ_0 is set equal to 0.3.

The largest coefficient of friction is reached when both the surfaces are rough and, in particular, when the first slope is greater of the two, which is the case of asymmetrical roughness (red stars in Figure 1.4). More broadly, contacts with both rough surfaces show a larger coefficient of friction, with respect to the rough-flat surface contacts. When β tends to 90°, some reported cases collapse: this is the case for $\varphi_1 = \varphi_3 > \varphi_2 = \varphi_4$ and $\varphi_1 = \varphi_3 < \varphi_2 = \varphi_4$, which have the same coefficient of friction if β is 90°. The same occurs for $\varphi_1 > \varphi_2$ $\varphi_3 = \varphi_4 = 0$ and $\varphi_1 < \varphi_2$ $\varphi_3 = \varphi_4 = 0$, where, in fact, the roughness asymmetry becomes negligible when the sliding is along the y direction. All these results confirm what was previously surmised from the analytical solutions. In Figure 1.4 values of μ are normalized by μ_0, the local coefficient of friction used in the isotropic Coulomb friction model.

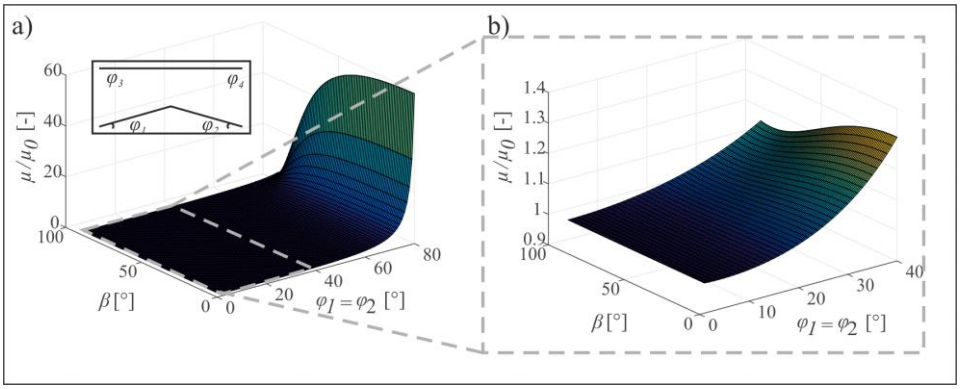

Figure 1.5 a) Variation of the global coefficient of friction by assuming one flat upper surface and one lower rough surface with respect to wedge slopes and the direction of sliding. b) Focus on the first part of the function: for smaller asperities slopes, reliable values of global coefficient of friction are obtained. This behaviour highlights the field of application of the model, which is suitable for asperities with small angles. μ_0 is set equal to 0.3.

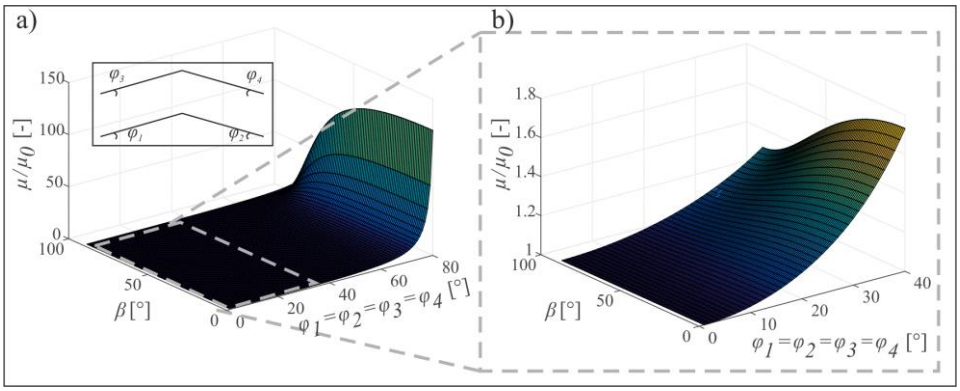

Figure 1.6 a) Variation of the global coefficient of friction by assuming both rough surfaces surface with respect to wedge slopes and the direction of sliding. b) Focus on the first part of the function: for smaller asperities slopes, reliable values of global coefficient of friction are obtained. This behaviour highlights the field of application of the model, which is suitable for asperities with small angles. μ_0 is set equal to 0.3.

In case of sharp-shaped asperities (φ = 60° or more), the global coefficient of friction μ becomes ten times higher and continues to increase, especially for small values of β (see Figure 1.5 and Figure 1.6). For φ = 90° it tends to an infinite value.. An angle φ close to 90° means that the asperities are vertical to the *xy*

plane, e.g. holes or pillar on a flat substrate. Indeed, in this situation, the tangential force arises to infinite values. Considering a single spring, sliding along the surface profile, when it faces the vertical asperity, its sliding is obstructed and an infinite value of the coefficient of friction is reached, meaning that the relative motion stops.

However, if one focused on the first parts of the graphs (dashed boxes) corresponding to smoother surfaces (φ < 45°), results are encouraging in the presence of both flat-rough or only rough surfaces and highlight that the model could be applied to smoother roughness.

1.3. ALSFM for 1D general roughness

Now consider two rough surfaces in contact, modelled as reported in Figure 1.7, so that roughness is expressed by a continuous and differentiable function with a defined periodicity.

The surfaces are defined as functions of the only variable x, while they are extruded along y direction: the slope φ is the inverse tangent of the derivative of function $z(x)$ obtained in P (φ_P)

These surfaces (the lower surface is identified by no. 1, while the upper is no. 2) are described by two functions, which can be expressed as:

$$z_1 = f_1(x) \tag{1.23}$$

$$z_2 = f_2(x). \tag{1.24}$$

As stated before, it is assumed that the isotropic Coulomb friction model describes the local friction between surfaces and that the surfaces in contact are modelled with a lattice of equally spaced longitudinal springs, which governs their interaction.

As stated previously, if no adhesion occurs, it is assumed that the springs are all characterized by the same longitudinal stiffness *k*, and the two bodies interact with normal elastic forces, which arise when the springs are compressed or elongated.

Firstly, the force equilibrium at point P ($P \in f(x)$) due to a single spring interaction is analysed (Figure 1.7.b).

β_0 identifies the direction of the sliding velocity vector v_0 on the π plane (Figure 1.7.a), which is the tangent plane in P, tilted by $\varphi = \varphi_P$ from the xy plane (φ_P is the intersection between the tangent plane in P and the xy plane), while v and β are the projected sliding velocity and the projection of β_0 on the xy plane, respectively.

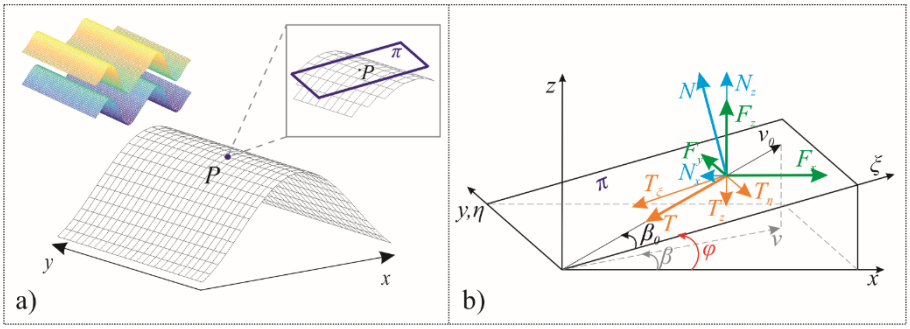

Figure 1.7 a) Detail of a surface with 1D roughness (along x direction): we consider the force equilibrium at point P, P ∈ f(x) due to the spring interaction. To obtain each force contribution, in this case the tangent plane (π) in P is considered. b) Force decomposition on π is considered with respect to the global system xyz in P. β_0 identifies the direction of the sliding velocity vector v_0 on the π plane, tilted by φ from the xy plane, while v is the projected sliding velocity and β the projection of β_0 on the xy plane.

A spring fixed on the upper asperity (surface z_2) is considered, while it is sliding on the lower one (surface z_1); l_0 is the spring length at rest: the actual spring length l depends on the geometrical shape of the asperities. Functions z_1 and z_2 describe the surface asperities; for a certain point P, the spring length is equal to:

$$l_p = z_2(x_p) - z_1(x_p) \tag{1.25}$$

Due to its length variation, the single spring generates an elastic force that can be expressed as follows:

$$F_z(P) = (l_0 - l_P)k_c \text{ in case of compression;}$$

$F_z(P) = 0$ in case of elongation (see Chapter 2 if adhesion occurs);

From force equilibrium, the expression for the local normal force *N*, acting on the π plane is obtained. The tangential force is equal to $T = \mu_0 N$, where μ_0 indicates the local coefficient of friction. The expression for *N* is similar to the previous one:

$$N = ku\left[\cos\varphi_P - \frac{\mu_0 \tan\varphi_P \cos\beta}{\sqrt{1+\tan^2\varphi_P\ \cos^2\beta}}\right]^{-1} \tag{1.26}$$

Where φ_P, β and μ_0 are defined as previously.

As before, the denominator should be different from zero, leading to the same limitations as in the previous case, which constrain the tilt of the wedge asperities. Referring to the global reference system, it is possible to express the tangential force with respect to the normal elastic force, similar to Eq. (1.6) and (1.7):

$$F_x = F_z \frac{\sin\varphi_P \sqrt{1+\tan^2\varphi_P \cos^2\beta} + \mu_0 \cos\beta}{\cos\varphi_P \sqrt{1+\tan^2\varphi_P \cos^2\beta} - \mu_0 \tan\varphi_P \cos\beta} = F_z H_x(\mu_0, \varphi_P, \beta) \tag{1.27}$$

$$F_y = F_z \frac{\mu_0 \sin\beta}{\cos\varphi_P \sqrt{1+\tan^2\varphi_P \cos^2\beta} - \mu_0 \tan\varphi_P \cos\beta} = F_z H_y(\mu_0, \varphi_P, \beta) \tag{1.28}$$

When one surface is moving against the other, each spring length changes in time, due to the anisotropy in *x* direction.

Consider now a certain number *n* of springs, acting on both asperities. The following equations can be adopted, where each number associated to a force identifies the surface on which it is applied.

If the whole asperity is considered, the total normal force R_z will be equal to:

$$R_z = \sum F_z^{(1)} + \sum F_z^{(2)} \tag{1.29}$$

$F_z^{(1)}$(normal forces acting on the lower surface), $F_z^{(2)}$(normal forces acting on the upper surface).

The same expressions are obtained for the tangential forces in both the principal directions R_x and R_y, following the same subdivision as in Eq. (1.8) and (1.9):

$$R_x^{(1)} = \sum F_x^{(1)} = \sum F_z^{(1)} H_x(\mu_0, \varphi_P, \beta) \tag{1.30}$$

$$R_y^{(1)} = \sum F_y^{(1)} = \sum F_z^{(1)} H_y(\mu_0, \varphi_P, \beta) \tag{1.31}$$

$$R_x^{(2)} = \sum F_x^{(2)} = \sum F_z^{(2)} H_x(\mu_0, \varphi_P, \beta) \tag{1.32}$$

$$R_y^{(2)} = \sum F_y^{(2)} = \sum F_z^{(2)} H_y(\mu_0, \varphi_P, \beta) \tag{1.33}$$

It is useful to observe that these expressions can be subdivided into two terms. The first is the elastic contribution, which depends on the length variation of the springs, on the function derivative in each point and on *v*. The second term (H_i) is a geometrical part, which depends on to one of the two asperities, on the velocity orientation β and on the local friction coefficient μ_0.

From the previous relationships, in the case of no adhesion, the coefficient of friction μ_x , μ_y and the global coefficient of friction μ are obtained as in Eq. (1.14), (1.15) and (1.13) respectively.

Following the Coulomb's law, the tangential force is proportional to the normal force applied to the surface. Thus, the tangential forces R_x and R_y can be expressed in the following form:

$$R_x = \sum F_z^{(1)} H_x(\mu_0, \varphi_P, \beta) + \sum F_z^{(2)} H_x(\mu_0, \varphi_P, \beta) \tag{1.34}$$

$$R_y = \sum F_z^{(1)} H_y(\mu_0, \varphi_P, \beta) + \sum F_z^{(2)} H_y(\mu_0, \varphi_P, \beta) \tag{1.35}$$

P represents each point in which the equilibrium between friction forces and elastic/reaction forces is considered. The equilibrium is calculated *n* times for a single time step, where *n* is the number of nodes in which the surfaces are discretized.

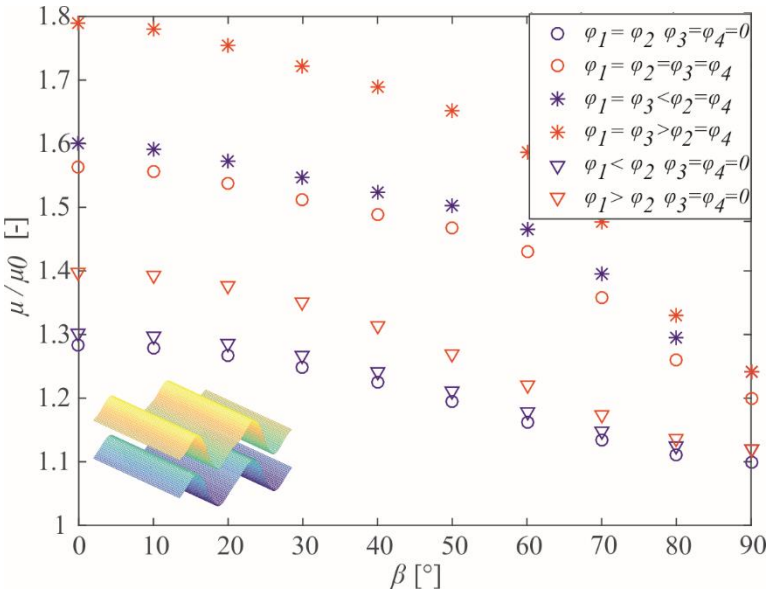

Figure 1.8 Coefficient of friction for six case studies reported in the box for two derivable periodic surfaces. As in the previous case, the coefficients are calculated by assuming different direction of sliding (β). μ_0 is set equal to 0.3.

Figure 1.8 shows the results of six different configurations of roughness with respect to the influence of the sliding direction (β). As reported, the direction of sliding strongly affects the coefficient of friction μ. Furthermore, it is stated that generic 1D roughness has globally a higher friction coefficient than the equivalent wedge asperities (for the generic 1D roughness we refer to φ_1, φ_2, etc., as the average slopes of the surface z_1 and z_2). As previously stated, some of these results collapse into the same value, if the sliding occurs along the *y* direction.

In Figure 1.9, the global friction coefficient μ is reported with respect to time (i.e. sliding distance if the sliding velocity is constant) in the presence of 1D symmetric sinusoidal shaped asperities. The graph shows the evolution of the global coefficient of friction with respect to the local coefficient μ_0 after a small sliding length. They highlight the influence of the surface profile, the contribution of the local coefficient of friction and the direction of sliding. By increasing the sliding distance, these oscillations recall the experimental results obtained from common

friction tests, as reported in Chapter 4, or in other works (Antoni et al. 2007; Gualtieri et al. 2009). The resulting global friction coefficients are the average values of these curves.

The average global coefficients of friction increase, following the local coefficient of friction. At the same time, as inferred previously, the sliding direction β strongly influences both the oscillations around the mean values and the mean values as well. With $\beta = 90°$ no oscillations occur due to the shape of the surfaces, which are extruded along the *y* direction in the *xy* plane.

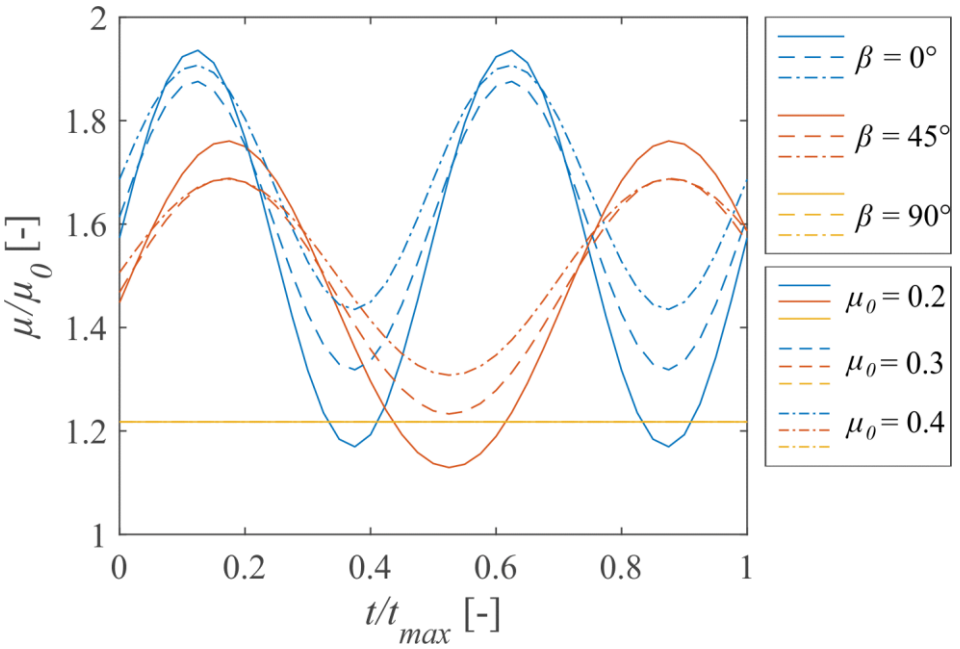

Figure 1.9 Friction coefficient μ with respect to time (i.e. sliding distance if the sliding velocity is constant) for two 1D symmetric sinusoidal shaped asperities. The graph shows the evolution in time of the global coefficient of friction with respect to the local coefficient μ_0. The average values increase, by increasing the local coefficient of friction. At the same time, the sliding direction β strongly influences both the oscillations around the mean values and the mean values as well. With β = 90° no oscillations occur due to the shape of the surfaces, which are extruded along the y direction in the xy plane.

1.4. Extended ALSFM for 2D roughness (2D-ALSFM)

The Anisotropic Lattice Spring Friction Model for 1D roughness is adapted in this section to surfaces characterized by two-dimensional (2D-ALSFM) roughness, which changes in both *x* and *y* directions.

The initial hypotheses are the same as in the previous studies: two rough surfaces in contact, modelled as reported in Figure 1.10, where roughness can be expressed by a continuous and differentiable function of *x* and *y* with a defined periodicity. These surfaces (as before, the lower surface is identified by no. 1, while the upper is no. 2) are described by two functions:

$$z_1 = f_1(x, y) \tag{1.36}$$

$$z_2 = f_2(x, y). \tag{1.37}$$

Due to the presence of vertical springs, the two bodies share normal elastic forces, which can be modified when the springs are compressed or elongated.

This configuration is adopted to consider the contributions of both rough surfaces to the global coefficient of friction.

Firstly, the force equilibrium at point $P \in f(x, y)$ in the presence of a single spring interaction is considered (Figure 1.10 b). To obtain each force contribution, the plane π (Figure 1.10 a), tangent to the surface in *P*, is considered, by Eq. (1.38):

$$(x - x_P)\frac{\partial G}{\partial x} + (y - y_P)\frac{\partial G}{\partial y} + (z - z_P)\frac{\partial G}{\partial z} = 0 \tag{1.38}$$

$$G: f(x, y) - z = 0 \tag{1.39}$$

G is the set of points, which satisfy the Eq. (1.39). From the equilibrium at point *P*, the forces are firstly referred to the rotated reference system *x'y'z*, where the *x'* axis and *y'* axis are the concurrent straight lines generating the tangent plane in *P* (*y'* correspond to the η axis, while *x'* is the projection of the ξ axis on the *x'y'z* reference system). Once the acting and reacting forces are estimated with respect

to the local system $x'y'z$ in P (Figure 1.10 c), to determine the final reactions in the global reference system xyz, the rotation matrix must be applied (α). β_0 identifies the direction of the sliding velocity vector v_0 on the π plane, tilted by $\varphi = \varphi_P$ from $x'y'$ plane, φ_P is the intersection between the tangent plane in P and the $x'y'$ plane), while v and β' are the projected sliding velocity and the projection of β_0 on the $x'y'$ plane, respectively. In the global reference system *xyz* the sliding direction is identified by β, with $\beta = \beta' + \alpha$.

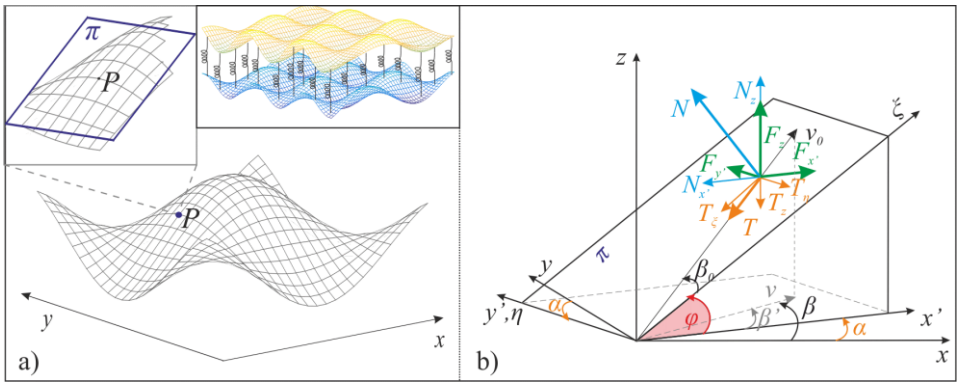

Figure 1.10 a) 2D roughness characterizes both surfaces in contact. A set of longitudinal springs governs the interaction at the interface. Details of one surface with 2D roughness: we consider the force equilibrium at point P, P ∈ f(x,y) due to the spring interaction. To obtain each force contribution, the tangent plane (π) in P is considered. b) Force decomposition on π is considered with respect to the local system x'y'z' in P. To obtain the overall reactions in the global reference system xyz, the rotation matrix must be applied (α). β_0 identifies the direction of the sliding velocity vector v_0 on the π plane, tilted by φ from the x'y' plane, while v is the projected sliding velocity and β' the projection of β_0 on the x'y' plane.

The equilibrium is considered for a spring fixed on the upper asperity (surface z_2) and slides on the lower (surface z_1); l_0 is the spring length at rest: the actual spring length l depends on the geometrical shape of the asperities. Functions z_1 and z_2 describe the surface asperities and, for a certain point P, the spring length is equal to:

$$l_p = z_2(x_p, y_p) - z_1(x_p, y_p) \tag{1.40}$$

As before, the single spring generates an elastic force:

$$F_z(P) = (l_0 - l_P)k_c \text{ in case of compression;}$$
$$F_z(P) = 0 \text{ in case of elongation (see Chapter 2 if adhesion occurs);}$$

Locally, the normal force *N* acting on the $\boldsymbol{\pi}$ plane is deducted. The tangential force is equal to $T = \mu_0 N$, where μ_0 is the local coefficient of friction (as for the previous cases the model follows the isotropic Coulomb's law to describe local friction).

The limitations obtained for *N* are the same as before.

Referring to the $x'y'$ plane, from the equilibrium, the tangential forces follow Eq. (1.27) and (1.28) but expressed in the rotated system, while the normal elastic force is still expressed by Eq. (1.1):

$$F_{x'} = F_z \frac{\sin\varphi_P \sqrt{1 + \tan^2\varphi_P \cos^2\beta'} + \mu_0 \cos\beta'}{\cos\varphi_P \sqrt{1 + \tan^2\varphi_P \cos^2\beta'} - \mu_0 \tan\varphi_P \cos\beta'} = F_z H_x(\mu_0, \varphi_P, \beta') \quad (1.41)$$

$$F_{y'} = F_z \frac{\mu_0 \sin\beta'}{\cos\varphi_P \sqrt{1 + \tan^2\varphi_P \cos^2\beta'} - \mu_0 \tan\varphi_P \cos\beta'} = F_z H_y(\mu_0, \varphi_P, \beta') \quad (1.42)$$

When one surface is moving against the other, each spring length changes in time, due to the variation in both *x* and *y* direction.

Finally, to achieve the reaction forces in *xyz* system (F_x and F_y), a rotation of the local reference system *x'y'z* is needed, thanks to the well-known relationship:

$$\begin{pmatrix} X_P \\ Y_P \end{pmatrix} = \begin{bmatrix} \cos\alpha_P & \sin\alpha_P \\ -\sin\alpha_P & \cos\alpha_P \end{bmatrix} \begin{pmatrix} X'_P \\ Y'_P \end{pmatrix}$$

Where α_P is the rotation of the local reference system in *P* with respect to the global system, while *X* and *Y* are the quantities to be led back to the global reference system.

This procedure must be adopted for each spring of the system.

Once all the local reaction forces in the *xyz*-system are calculated, equations from (1.29) to (1.35) are used to obtain R_z, R_x and R_y.

In the following graphs, some results in the case of 2D roughness are reported.

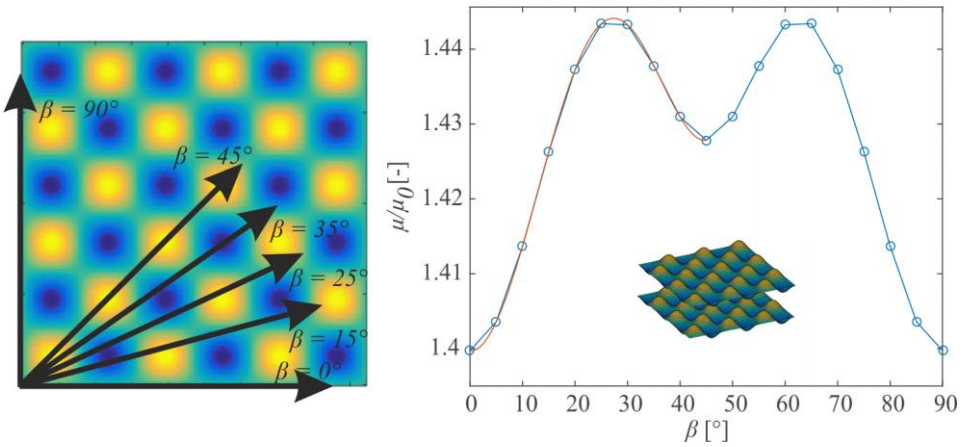

Figure 1.11 Variation of the coefficient of friction between two 2D rough surfaces with respect to the direction of sliding β. The upper and lower surfaces are the same and with symmetric roughness, thus the coefficient of friction μ varies between 0° and 45°. The blue line shows how the coefficient of friction changes between 0° and 90°, with a step Δβ equal to 5°, while the red line is the friction coefficient obtained for smaller steps. μ_0 is set equal to 0.3.

Firstly, the dependence of the friction coefficient with respect to various sliding directions (β) has been analysed (Figure 1.11). Two surfaces described by the same function, with symmetrical 2D asperities, both along *x* and *y* directions are analysed. Due to symmetry, the coefficient of friction is expected to be the same if one surface is sliding with β equal to 0° or β equal to 90°.

These results are reported in Figure 1.11.

In addition, the coefficient of friction in the 2D case does not vary as much as it does in the 1D roughness case with respect to the sliding direction. This is due to the different shape of the surfaces, where the succession of summits and valleys both along *x* and *y*-direction generate smaller frictional forces.

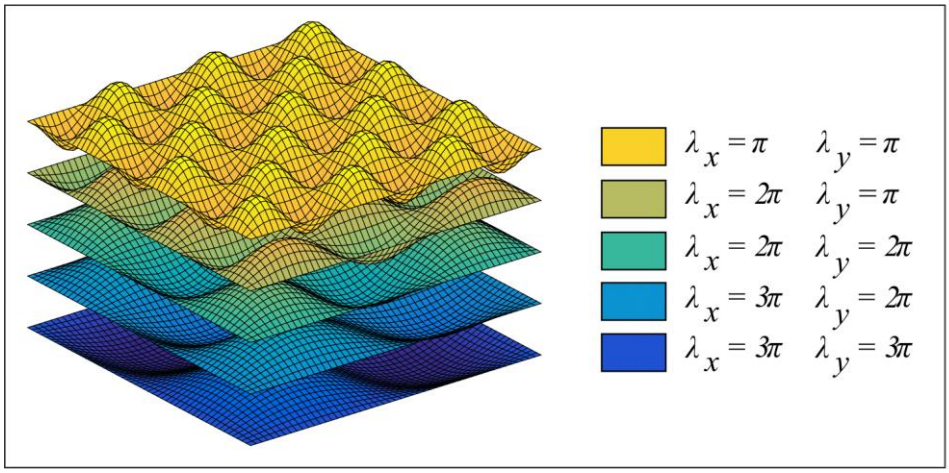

Figure 1.12 Some of the analyzed surfaces for the 2D roughness. The wavelengths vary along x and y (no differences occur between upper and lower surfaces) and the friction behavior is studied, due to these variations in both wavelength and sliding direction.

Since to slide up a summit implies a higher friction force rather than to slide down in a valley, the coefficient of global friction appears to be almost constant with respect to β. More changes may occur if the wavelength of the asperities are modified.

The coefficient of friction can increase/decrease by considering several combinations of wavelength in x and y directions (respectively λ_x and λ_y). Globally, 25 combinations are reported, each with sliding direction β from 0° (Figure 1.13 a), 45° (Figure 1.13 c) and 90° (Figure 1.13 b).

As in the previous case, the results are as expected. Figure 1.13 a) and b) are symmetrical and display the maximum coefficient of friction for the smallest wavelengths ($\lambda_x = \lambda_y = \pi$). In addition, the bigger coefficient of friction is reached if the smaller wavelength is the one in the direction of sliding. For example, in Figure 1.13 a), when $\lambda_x = \pi$ and the direction of sliding is along the x-axis ($\beta = 0$) the bigger coefficient of frictions are reached and appears to be slightly affected by variations in λ_y. On the contrary, with $\beta = 0$, μ varies significantly by changing λ_x. Opposite results are observed in Figure 1.13 b), due to $\beta = 90°$.

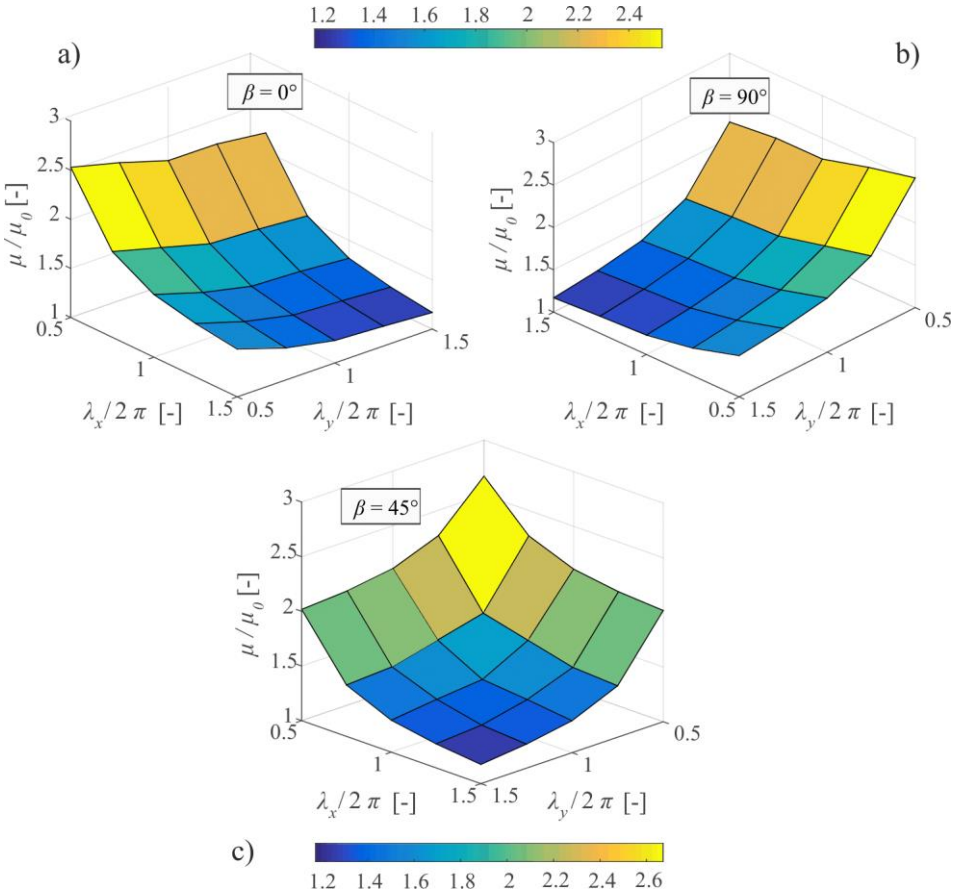

Figure 1.13 Changes in the friction coefficient by varying both wavelength in x and y directions (from $\lambda = \pi$ to $\lambda = 3\pi$) and sliding direction β from 0° (a) then 45° (c) and finally 90°(b). As expected, a) and b) are symmetrical and show the maximum coefficient of friction for the smallest wavelengths and this trend is preserved in the direction of sliding. Instead, the minimum value is reached for the biggest wavelengths. With β equal to 45°, the coefficient of friction is symmetrical with respect to the middle values. μ_0 is set equal to 0.3.

These insights may suggest that the wavelength that mainly governs the coefficient of friction is the one in the same direction as β, because the asperities that the surfaces are facing are predominant in influencing the coefficient of friction, and they become smoother as the wavelength increases. The increase in wavelength perpendicular to the motion slightly affects the values of μ, reaching the minimum value for both the largest wavelengths. If the direction of sliding β

is equal to 45°, the coefficient of friction shows a symmetrical behaviour with respect to the diagonal middle values. This is reasonable because both the wavelength play the same role in enhancing or decreasing the global coefficient of friction.

1.5. Preliminary conclusions

In Chapter 1, a theoretical model for anisotropic friction is described, which considers the interactions and effects of two rough surfaces in contact, when one is sliding with respect to the other.

This study shows that the friction coefficient strongly depends on the roughness of the surfaces involved and the case with $\varphi_1 = \varphi_3 > \varphi_2 = \varphi_4$ has the highest friction coefficient; if one surface is flat, it decreases. In general, generic 1D roughness shows higher dynamic friction coefficients than the saw tooth shape.

Furthermore, by introducing 2D roughness, the model appears to be more suitable for the description of generic roughness and numerous case studies are presented.

The results of this investigation prove that both roughness and sliding direction affect the global coefficient of friction: in particular, 1D roughness is easily influenced by both these quantities, while in the case of 2D roughness, it seems that μ is especially modified by the shape of surfaces, while the direction of sliding affects the results to a lesser extent.

Thus, the work described in this Chapter represents the starting point for the development of this friction model.

With respect to the model developed by Mroz and Stupkiewicz (Mróz and Stupkiewicz 1994), the ALSFM has been extended to surfaces with non-symmetrical roughness and to surfaces described by periodic functions with one or two variables. Moreover, it takes into account also the differences between rough-rough contact or rough-flat contact.

As in the previous model, the Coulomb's friction law is adopted as the local friction law and μ_0 must be smaller than $cot\varphi$. Equally, only a compressive behaviour of the springs is allowed at this point.

Accordingly, in Chapter 2, this model is expanded to include other tribological phenomena such as adhesion, wear and multiple hierarchical asperities in order to thoroughly analyse the effects of surface topology and hierarchy in the friction response of multilevel surfaces.

Chapter 2

2. Hierarchical HALSTM for 1D and 2D roughness

Systems and structures in nature draw a lot of attention thanks to their high efficiency and durability. Biological materials and systems, as bones and nacre, have optimized their mechanical properties by combining high strength and toughness (Du et al. 2015; Pugno 2006; Pugno and Carpinteri 2008). To date, the interest in transferring technologies from biological systems into engineering applications has been greatly pursued, also in the field of tribology.

Indeed, biological structures have efficient ways to minimize or maximize friction or to adapt to different environments depending on the goals (Jin and Dowson 2013; Liskiewicz et al. 2008). Synovial joints, gecko feet, hydra, are all examples in which a biological structure evolved to optimize the tribological performance, providing adhesion, improved slip or a perfect lubrication for motion (Autumn et al. 2000; Bhushan 2007; Boesel et al. 2010; Liskiewicz et al. 2008; McCarthy et al. 2012; Pugno et al. 2011; Pugno and Lepore 2008).

Usually these intriguing properties have been developed by biological systems thanks to a specific hierarchical structure. By changing their organization, variations in the mechanical and physical properties are possible.

In Figure 2.1 some examples of hierarchical structures are reported.

Friction is not only a macroscopic problem, but it also involves several effects that occur at the micro and nanoscale, from adhesion to asperity interactions (Nosonovsky and Bhushan 2007, 2008).

Contact between rough surfaces is an example of a multiscale problem, addressed in past and recent works (Capozza and Pugno 2015; Carbone et al. 2009; Carbone and Bottiglione 2008, 2011; C Caroli and Nozières 1998; Mróz and Stupkiewicz 1994; Persson, Bucher, and Chiaia 2002; Stupkiewicz, Lewandowski, and Lengiewicz 2014), sometimes resorting to self-affine shapes, leading to

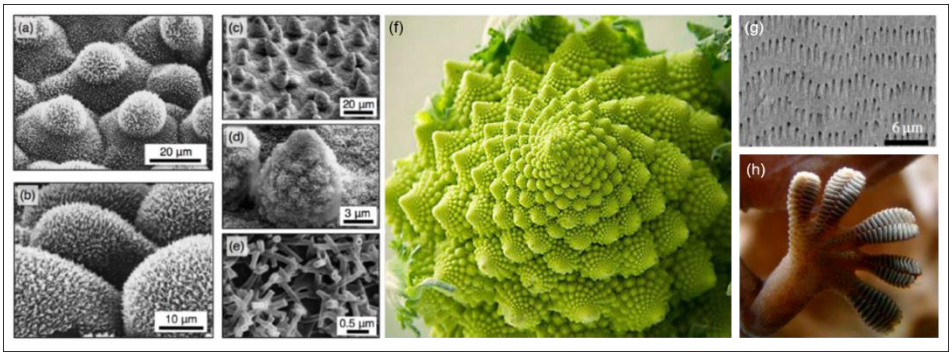

Figure 2.1 Some examples of hierarchical and biological surfaces, SEM images of the (a) taro plant (Colocasia esculenta), (b) parrot feather plant (Myriophyllum aquaticum), and (c)–(e) lotus plant (Nelumbo nucifera) at various scales (McCarthy et al. 2012). *In (f) the Brassica oleracea is an example of hierarchical and fractal surface (web source). A surface for anisotropic friction is reported in (g), with an example of snake skin microstructure (Lampropeltis getula californiae)*(Tramsen et al. 2018). *Finally, a gecko's foot, with a focus on the hierarchical morphology that covers its skin* (Liskiewicz et al. 2008).

hierarchical and fractal geometries (Borodich and Onishchenko 1999; Costagliola et al. 2016; Gagnepain and Roques-Carmes 1986; Popov and Dimaki 2011; Vakis et al. 2018).

In order to take into account the multiscale aspect of friction, in this Chapter the concept of hierarchical friction is introduced in the ALSFM, by analysing multilevel surfaces. Furthermore, to describe other phenomena associated to sliding friction, adhesion is included, as well as wear, by adopting the Archard's wear model (Archard 1953) to describe the evolution of the contact surface during multiple sliding.

2.1. Introducing adhesion in the ALSFM

Many times adhesion has been neglected, due to the presence of surface roughness (Fuller and Tabor 1975; Persson et al. 2005), which can remove the adhesive forces. However, even if roughness vanishes the adhesion contribution, the area of real contact is still affected by its presence (B N J Persson 2000). In addition,

adhesion must be considered, if the surface is characterized by a smooth roughness.

The most common analytical models developed to study adhesive contacts are the Johnson-Kendall-Roberts (JKR) model and the Derjaguin-Muller-Toporov (DMT) model, with related studies (Derjaguin, Muller, and Toporov 1975; Greenwood 1997; Johnson, Kendall, and Roberts 1971; Tabor 1977). JKR model assumes an elastic sphere in contact with a flat substrate with a free energy per unit area, which occurs when the contact is reached (Johnson et al. 1971; B N J Persson 2000). Due to this energy, a contact spot with finite radius remains even if the external load is zero. This contact breaks at a critical pull-out force. The model gives the values of the contact force and the minimum contact radius at which a mechanical instability breaks the bond. If no free surface energy is present, the model collapses into the Hertz's model (Hertz 1882; Johnson et al. 1971; B N J Persson 2000). The JKR model is accurate for soft materials and high surface energy, otherwise the DMT model must be applied , which has been formulated for adhesion between hard spheres (B N J Persson 2000).

In particular, due to a wide interest in bioinspired applications, in the last decades there has been an increase in research on adhesion (Autumn et al. 2000; Boesel et al. 2010; Jung and Bhushan 2006; Kim and Bhushan 2007; Pugno et al. 2011; Pugno and Lepore 2008; Varenberg, Pugno, and Gorb 2010; Yu et al. 2012). For example, further developments of the DMT theories have shown that adhesion generates an additional load around each asperity (Vakis et al. 2018).

Other works investigated the adhesion hysteresis contribution to friction (Carbone and Mangialardi 2004), adhesion between surfaces with smooth roughness (Persson et al. 2005), or simulating the gecko seta in contact with rough surfaces to obtain the efficiency of the attachment (Kim and Bhushan 2007; Yu et al. 2012).

In the Anisotropic Spring Lattice Friction Model (ASLFM) illustrated in this thesis, adhesion is introduced in the model by adding the contribution of tensile springs, which can elongate to a length l_T that is larger than the rest length l_0.

When the load *L* decreases, even to zero, the springs relax and the elastic compressive force decreases (from Figure 2.2.a and Figure 2.2.b the load *L* is reduced). Due to the shape of a rough profile, some springs can elongate when the distance between the two sliding surfaces is bigger than the spring rest length. This generates a portion of the contact area subjected to tensile elastic forces, i.e. adhesion forces. Since the real area of contact determines the sliding friction force, adhesion, where present, can affect and modify the frictional behaviour of solids (Figure 2.2 c).

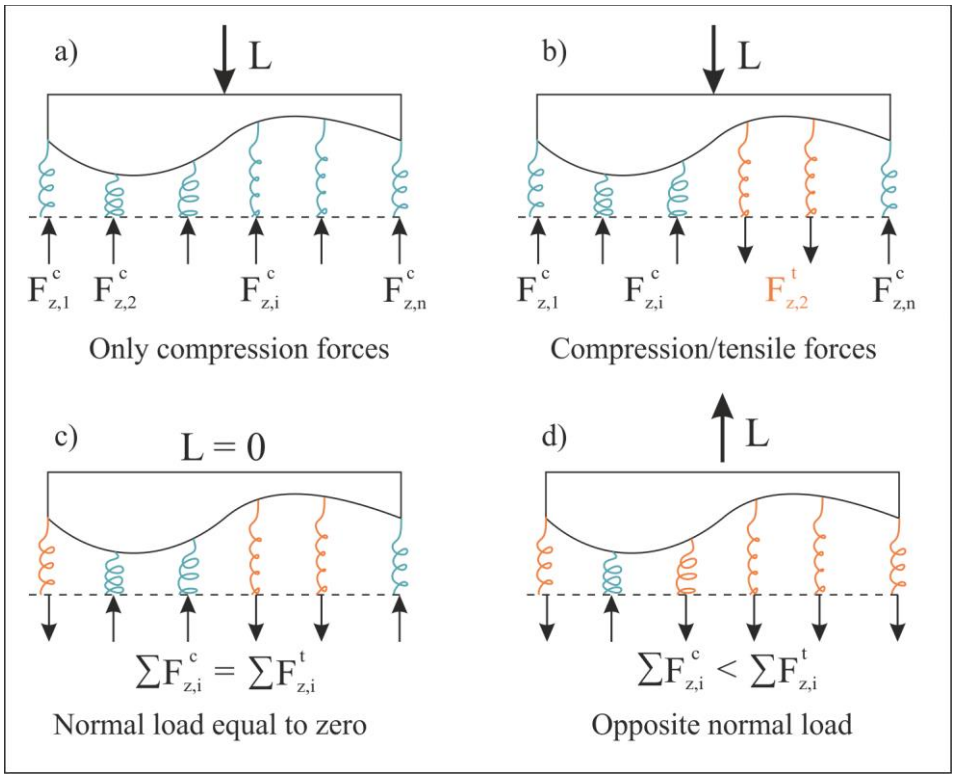

Figure 2.2 A 2D schematization of half model in various situations in the presence of adhesion, with decreasing L from a) to d). a) All the springs are compressed and the normal load is equal to the sum of all the spring axial forces. b) If some springs are elongated and L is the applied normal load, the sum of the compressive forces is larger than the load. c) In case of no external load, the sum of tensile and compressive forces on the springs is zero. d) In the case of a tensile load some compressed springs still generate friction.

The apparent normal load is:

$$L = \sum F_z^{(c)} + \sum F_z^{(t)} \tag{2.1}$$

Where $\sum F_z^{(c)}$ is the sum of all the compressive forces and $\sum F_z^{(t)}$ is the sum of the tensile forces, which have opposite directions. If no adhesion occurs, $\sum F_z^{(c)}$ is equal to the normal load L (Figure 2.2 a), otherwise $R_z^{(c)} = \sum F_z^{(c)}$ is larger.
It is assumed that the stretched springs do not generate a friction force by sliding, so that, the coefficient of friction is expressed as follows:

$$\mu_a = \frac{R_{x,y}\left(f\left(R_z^{(c)}\right)\right)}{L} \tag{2.2}$$

Where $R_{x,y}\,(\,f\,(R_z^{(c)}))$ indicates that the tangential force $R_{x,y}$ on the xy plane is generated only by the springs in compression, where f indicates that $R_{x,y}$ is a function of only the $R_z^{(c)}$ elastic forces. This means that the apparent coefficient of friction increases due to the presence of adhesion.
Springs are assumed with different compressive and tensile behaviours, by defining a compression stiffness and a tensile one, respectively k_c and $k_t = k_c/2$. With this assumption, the model takes into account a larger compression resistance than the tensile one. For a single spring in a certain point P, the elastic forces can be:

$$F_z(P) = (l_0 - l_P)k_c > 0 \text{ in case of compression;}$$
$$F_z(P) = \left(l_0 - l_{T,P}\right)k_t < 0 \text{ in case of elongation;}$$

In Figure 2.3, the model responses in the presence of adhesion for general 1D roughness (sinusoidal function) is reported.

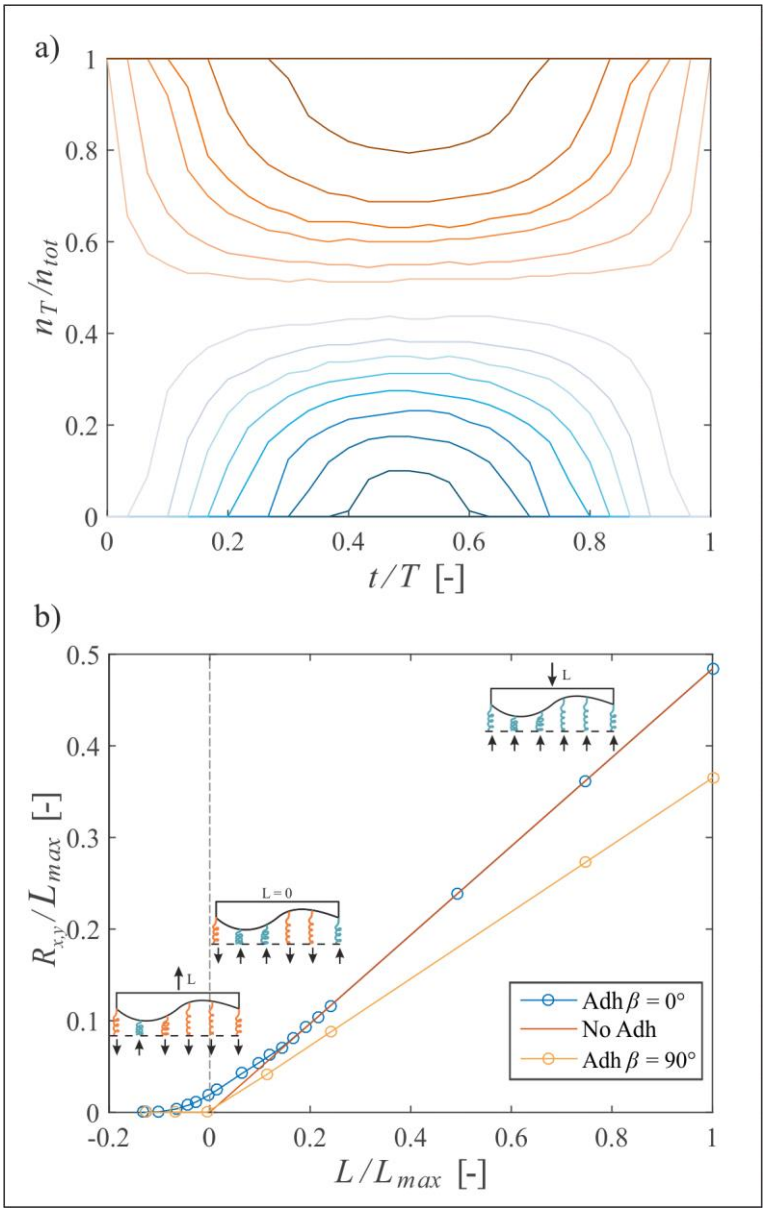

Figure 2.3 Effect of adhesion between 1D rough surfaces. a) Variation of springs elongation in time, normalized by the function period T. The number of stretched springs depends on the normal load. For each circular dot in b), a curve in a) is obtained. In the reported case, until the ratio L/Lmax is major than 0.3, the springs are all compressed (blue line in a), corresponding to zero for each time interval). After that value, some springs are elongated, and lines from blue to red show when and how many springs display a tensile force. When the upper and lower surfaces are both described by

the same function, and they are in phase, the number of elongated springs is described by lines with shades of blue, which refer to L>0. On the contrary, lines with shades of red describe the number of elongated springs once the load reduces and becomes tensile (L<0). b) Tangential force $R_{x,y}$ with respect to the applied normal load L. When no adhesion occurs, the coefficient of friction is the ratio between the two; on the contrary, when some springs become tensile,, a non-linear curve describes this relationship. In the presence of 1D roughness, adhesion does not affect the sliding with β=90°, because there is a swift transition from compressed to tensile springs along the y direction.

Several situations may occur, as shown from Figure 2.2 a-d: if all the springs are compressed, the sum of all the compression forces balance the applied normal load L. This is the case of the dots associated with high loads, (Figure 2.3 b). Then, if the load decreases, some springs may be elongated and these tensile forces are balanced by the remaining compressed springs (Figure 2.2 b). In Figure 2.3 a, the variation in time (normalized by the period of the functions T) of tensile springs (n_T) with respect to the total number of springs (n_{tot}) is reported (from blue to red curves).

The more the load reduces, the more the springs are elongated, until $L = 0$, in which the sum of the compression forces is equal in modulus to the sum of the tensile forces (opposite direction). If the surfaces are described by the same function *z (x,y)* and at $t = 0$ they are in phase, when the load is zero, the springs are no longer compressed at the beginning of sliding, following the red curves in Figure 2.3 a. By applying a negative load (tensile force), some springs could still be compressed (negative part of the graph in Figure 2.3 b).

When there is no spring elongation, the tangential force $R_{x,y}$ is linearly dependent on the normal force R_z, while if some springs start to elongate, the behaviour becomes non linear, due to adhesion effects. Moreover, adhesion appears to have a significant role only for small normal loads, as also reported in experimental works e.g. (He et al. 2008).

The presence of adhesion generates an (apparent) enhancement of the friction coefficient (or even a negative value, when the load has the opposite direction), if it is computed as in Eq. (2.2)

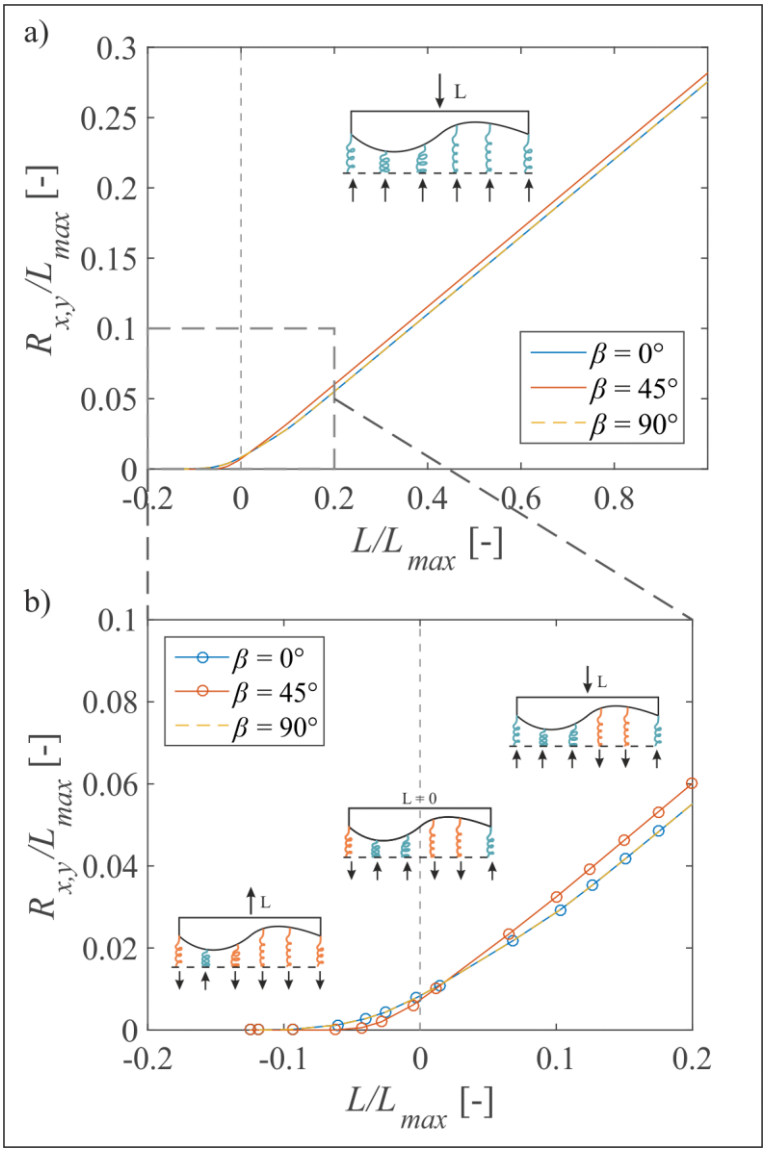

Figure 2.4 Effect of adhesion between 2D rough surfaces. a) Tangential force $R_{x,y}$ with respect to the applied normal load L, both normalized with respect to the maximum load L_{max}. Without adhesion effects, the coefficient of friction is the ratio of the two; when adhesion occurs, a non-linear relationship describes this relationship. In the presence of 2D symmetrical roughness, adhesion equally affects x and y directions of sliding (blue line and yellow dashed line). An

enlargement on the graph close to the origin is reported in b). With other sliding directions, e.g. β = 45°, the behaviour is without substantial differences from the previous cases.

When the surfaces are described by the same function, so that $z_1(x,y) = z_2(x,y)$, and the sliding direction β is equal to 90°, the springs do not modify their length along the sliding. In particular, if they are in phase at $t = 0$, adhesion does not influence the frictional behaviour (orange curve reported in Figure 2.3 b).

The roughness anisotropy clearly influences the frictional response, as the curves in Figure 2.3 b show. The sliding direction that mainly contributes in enhancing the effects of adhesion is $\beta = 0°$.

The effect of adhesion is different if we assume a 2D roughness.

The case of a 2D symmetrical roughness (sinusoidal function in both x and y directions) for both the upper and the lower surfaces in contact is reported. By displaying the tangential force $R_{x,y}$ with respect to the applied normal load L (Figure 2.4), it is evident that there is no significant dependence on the direction of sliding. Furthermore, adhesion equally affects x and y directions of sliding (blue line and yellow dashed line). Without adhesion effects, the coefficient of friction is the ratio of the two; when adhesion occurs, a non-linear relationship describes friction between rough surfaces. Figure 2.4 b) shows an enlargement on the graph close to zero. When the load L is equal to zero, a frictional force is still noticeable, due to some springs that are compressed and thus generate friction.

In the following figures (Figure 2.5, Figure 2.6 and Figure 2.7), the evolution of the contact surface during the sliding in the presence of an adhesive contribution is reported. In these graphs, roughness is described with the same function $z(x,y) = sin(x)*sin(y)$ for both upper and lower surfaces. During sliding, it is possible to notice two simultaneous situations: on the one hand, when the distance between the surfaces is larger than the rest length of the springs, tensile forces (yellow zones) characterize the associated area.

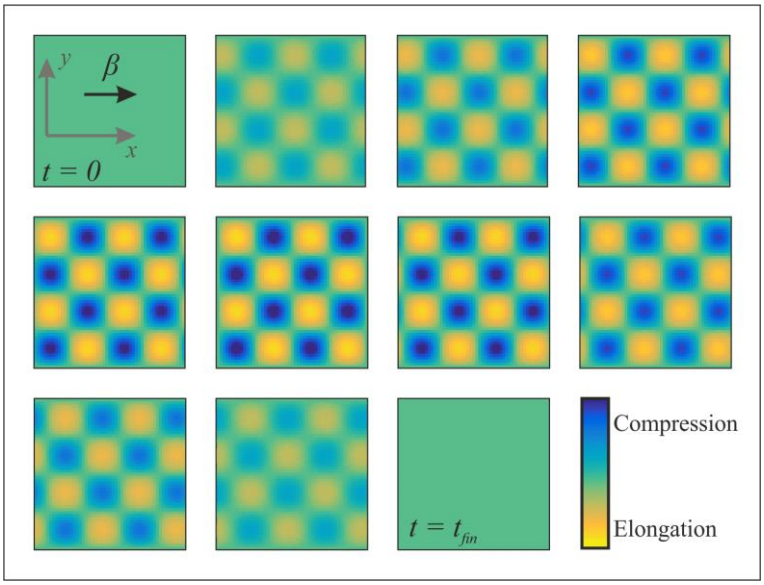

Figure 2.5 Surface distribution of both compressed (blue) and tensile (yellow) springs when the relative motion between two 2D rough surfaces is along the x direction. Only the compressed springs contribute to the calculation of the frictional force.

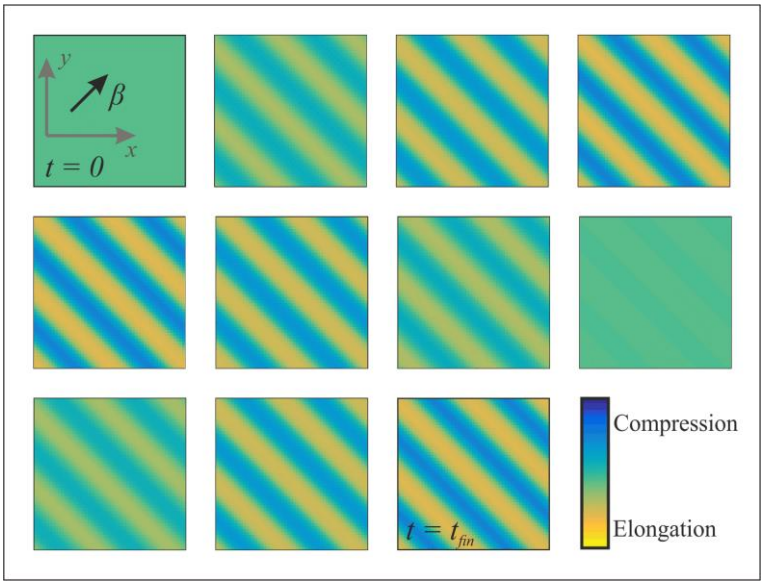

Figure 2.6 Surface distribution of compressed (blue) and tensile (yellow) springs when the sliding direction β is 45°. As stated before, only the compressed springs are assumed to contribute to

obtaining the frictional force. These tensile or compressed zones are perpendicular to the sliding motion, thanks to the simmetry of the surface roughness.

On the other hand, springs with a length smaller than the rest length determine areas with compressed forces (blue zones).

Only the compressed springs contribute to obtaining the tangential force $R_{x,y}$. For a certain applied load L, the compression forces grow to satisfy the equilibrium when some portions of the contact area are characterized by tensile forces.

From Figure 2.5 to Figure 2.7, it is also possible to see the evolution of the contact area as a function with the direction of sliding.

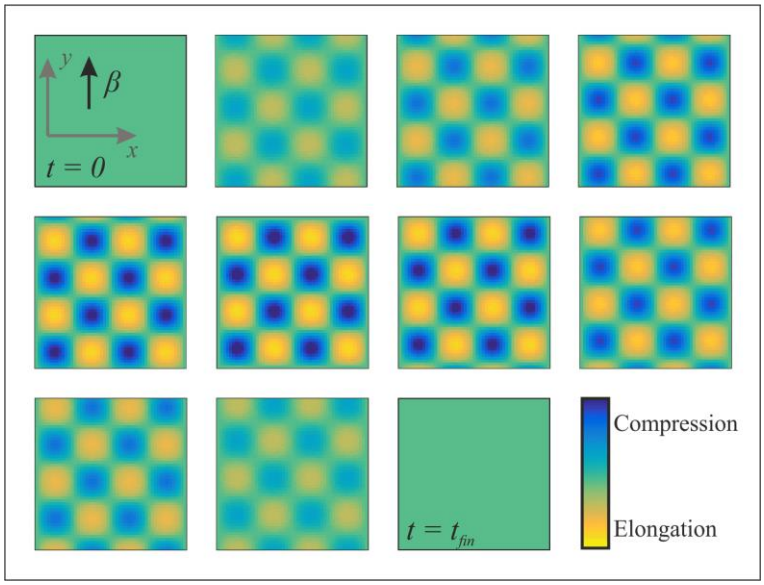

Figure 2.7 Surface distribution of compressed (blue) and tensile (yellow) springs when the relative motion between two 2D rough surfaces is along the y direction.

2.2. Introducing wear in the ALSFM

Among the various tribological phenomena related to sliding friction, one of the most significant is wear. As for friction, wear involves different physical and chemical processes occurring over different time and length scales. Several

empirical models have been developed, from the well-known Archard's model to recent works. Empirical models, experimental studies with wear track observations with Scanning Electron Microscope or Atomic Force Microscope, and recently numerical simulations have been performed to obtain the surface evolution during the sliding and the correlations between sliding velocity, mechanical parameters and wear volume (Archard 1953; Meng and Ludema 1995; B N J Persson 2000; Shu 1986; Vakis et al. 2018).

In this dissertation, wear is considered as a process affecting the contact surface as a function of time. This means that the more two surfaces are in a relative sliding motion, the more they modify their topography, due to material consumption. Thus, since the ALSFM describes the dependence of the coefficient of friction with respect to surface roughness, and roughness is modified by wear, its evolution in time is of great importance.

Wear is modelled as a dynamic process and, in order to predict it, Archard's wear law is adopted (Archard 1953):

$$\frac{V}{S} = K\frac{L}{H} \tag{2.3}$$

Where V is the total wear (transferred) volume, S is the sliding distance, L is the normal load, H is the surface hardness and K is the wear coefficient.

In this thesis, it is assumed that wear changes the shape of the asperities by reducing their initial amplitude until zero, so that a rough surface becomes flat. Rough surfaces become flat after a certain time T_W, which is the estimated time to completely smooth the surfaces, assuming a certain wear rate $W = V/S$ and a constant applied load, which does not change during the wear process (Figure 2.8).

In the presence of 2D roughness, the total transferred volume can also be expressed as follows (with $S = v_x t$ and $W = V/S$ is the *wear rate*):

$$\Delta V = \iint_{x_0,y_0}^{x_f,y_f} z(x,y)\,dx\,dy - B\iint_{x_0,y_0}^{x_f,y_f} z(x,y)\,dx\,dy = Wv_x\Delta t \tag{2.4}$$

$$B = 1 - \frac{Wv_x\Delta t}{\iint_{x_0,y_0}^{x_f,y_f} z(x,y)\,dx\,dy} \tag{2.5}$$

B is a reduction coefficient for the roughness amplitude and varies between 0 and 1. $B = 1$ means that wear has not modified the roughness yet, so that the transferred volume is zero. On the contrary, $B = 0$ implies that the rough surfaces become smooth, as a result of the wear mechanism.

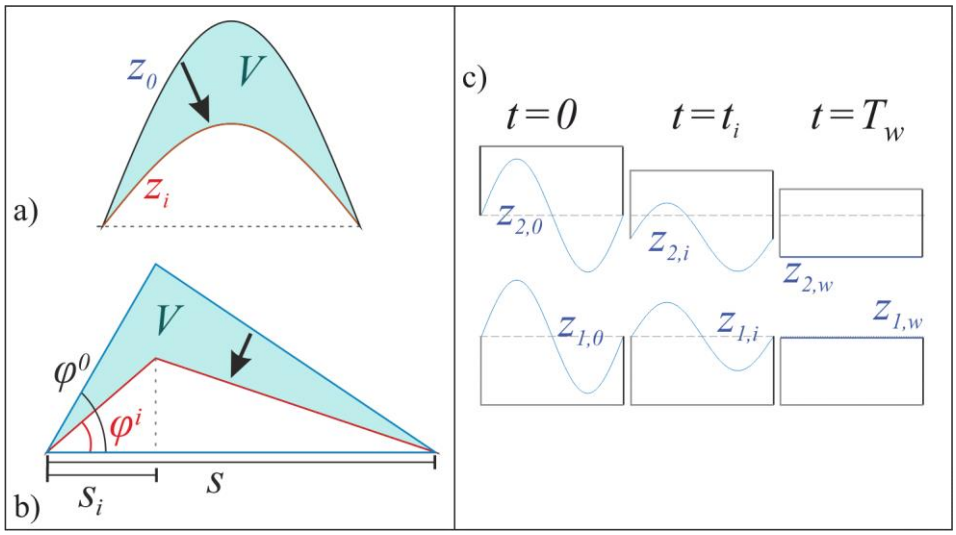

Figure 2.8 a) A schematization of the surface levelling after the wear process. z_0 is the initial surface shape, while z_i is the surface profile after a certain time t_i. At the end of the wear mechanism, the surface will be flat. b) A scheme of the surface levelling in case of 1D wedge asperities; φ^0 is the initial surface tilt angle, while φ^i is the smoothed surface after a certain time t_i. c) Surface roughness changing in time.

As stated in the previous Chapter, the 2D-ALSFM predictions for the global coefficient of friction are slightly affected by the direction of sliding, especially for symmetric asperities. This is also observed in Figure 2.9, where the first point

of each curve represents the global coefficient of friction (normalized by the local coefficient) without wear effects. These values are similar and, by adopting a local coefficient of friction $\mu_0 = 0.3$, the same results reported in Chapter 1 are achieved (Figure 1.11). Then, when the wear mechanism starts modifying the shape of surfaces, the coefficient of friction decreases non-linearly, until it reaches the value of the local coefficient μ_0, meaning that the surfaces become flat.

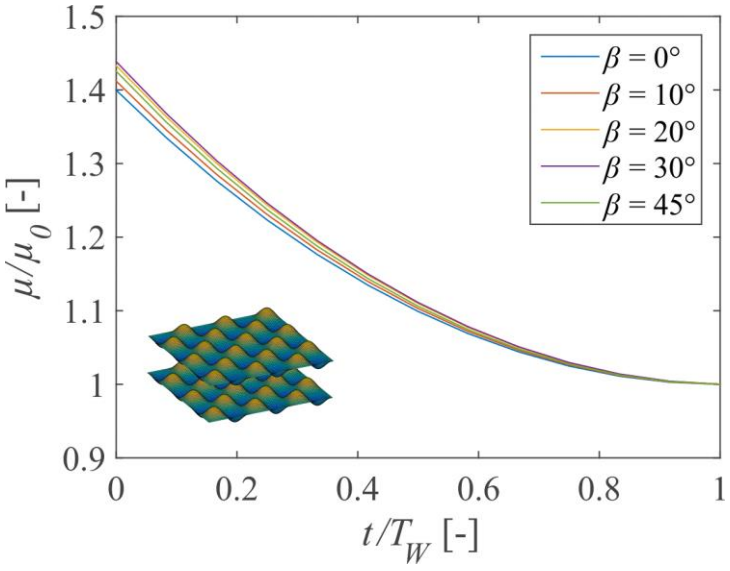

Figure 2.9 Variation in time of the friction coefficient between 2D rough symmetrical asperities. Five different directions of sliding (β) have been considered, from 0° to 45° (it has been demonstrated that from 45° to 90° the behavior is the same, due to symmetry. After a time equal to T_W the surfaces become flat, so that the friction coefficient tends to the local friction coefficient μ_0. μ_0 is set equal to 0.3.

When 1D roughness is considered, the previous formula changes as follows:

$$\Delta V = \Delta A \cdot Y = Y \cdot \left(\int_a^b z(x)\, dx - B \int_a^b z(x)\, dx \right) = W v_x \Delta t \qquad (2.6)$$

$$B = 1 - \frac{W v_x \Delta t}{Y \cdot \int_a^b z(x)\, dx} \tag{2.7}$$

Where Y is the asperity depth (y direction), ΔA refers to the total transferred volume per unit depth and B is the reduction coefficient for the roughness amplitude.

In the presence of 1D wedge asperities, wear reduces the slopes of the asperities from the initial tilt angles φ^0 to zero (flat surfaces, Figure 2.8 b).

The total wear volume can also be expressed as a function of the wedge asperity angles, finding the following relationship (with $S = vt$ and $W = V/S$):

$$\frac{d\, tan\, \varphi}{dt} = -\frac{2Wv}{{s_i}^2 Y} \tag{2.8}$$

It is possible to express the removed material as the volume V due to an angle reduction from the initial value φ_i^0 at time t_0 to φ_i^1 at a certain time t_i as follows:

$$tan\, \varphi_i^1 = -\frac{2Wv}{{s_i}^2 Y} t_i + tan\, \varphi_i^0 \tag{2.9}$$

In Figure 2.10, the effect of sliding wear is displayed, due to the variation in time of surface roughness and consequently of the friction coefficient. By supposing a certain wear rate W (order of magnitude $10^{-3}\,\mathrm{mm}^3/\mathrm{m}$, as reported in Shu 1986 for metals), after a time equal to T_W, the surfaces become flat and the friction coefficient tends to the local friction coefficient μ_0. The influence of the sliding direction β is more evident, with respect to Figure 2.9.

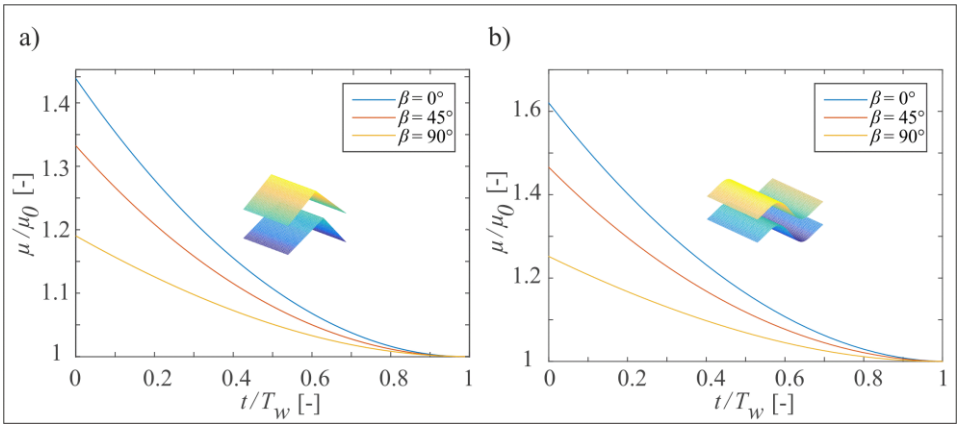

Figure 2.10 a) Variation in time of the friction coefficient between two wedge asperities. Three different directions of sliding (β) have been considered. After a time equal to T_W the surfaces become flat, so that the friction coefficient tends to the local friction coefficient μ_0. b) Variation in time of the friction coefficient between two asperities with generic 1D roughness, again for three different directions of sliding (β). After a time equal to T_W, the surfaces become flat, causing the friction coefficient to assume the local friction coefficient μ_0. As observed in Figure 1.8, the generic 1D roughness gives a higher friction coefficient, with respect to the equivalent wedge case.

2.3. Hierarchical ALSFM

As previously stated, friction is a multiscale phenomenon. When friction involves rough surfaces, the multiscale nature of their profiles can significantly affect the global coefficient of friction. For this reason, Archard proposed an hierarchical approach to describe friction in the presence of rough self-affine surfaces (Archard 1957). Hierarchical profiles and fractals have been adopted to describe also fractures in rock mechanics (Brown 1987), to give an overall characterization of surface roughness (Gagnepain and Roques-Carmes 1986; Majumdar and Bhushan 1991; Majumdar and Tien 1990) and to model friction and contact (Bhushan and Majumdar 1992; Borodich and Onishchenko 1999; Majumdar and Bhushan 1991; Popov and Dimaki 2011; Putignano et al. 2012).

In this context, the 1D and 2D-ALSFM are extended to study the effects of roughness surfaces characterized by a hierarchical structure. In this mechanical formulation, upper level characteristics depend on the previous lower level ones.

It is assumed that each asperity presents multiple levels of roughness, one inside the other. In this way, the surface is described with a certain number of sublevels *n*, which appear to be linked together. By applying the Hierarchical ALSFM, the global friction coefficient of the level *n* depends on the local friction coefficient μ_{n-1}, meaning that the sublevel influences the dynamic friction coefficient of the upper level.

At each roughness level, the springs are characterized by longitudinal motion. Indeed some simplifications need to be introduced. The isotropic Coulomb friction model is assumed to be valid in every sublevel, μ_0 is the local coefficient of friction for the lowest 1-level, $\mu_1 = f_1(\mu_0, z_1, z_2, \beta)$ is the global coefficient of friction at the 1-level and the local coefficient of friction in the 2-level, and similarly for the others. By adopting a surface roughness formed by some hierarchical self-similar levels, the periodic function in variables *x* and *y* is expressed as follows:

$$z = A^a * \sin\left(\frac{2\pi}{\lambda_x} B^b x\right) * \sin\left(\frac{2\pi}{\lambda_y} C^c y\right) \tag{2.10}$$

Where *A, B* and *C* are the coefficients that modulate the shape of the surfaces, while *a, b* and *c* depend on the level of roughness. In these studies $A = B = C$ are assumed equal to 10 and $b = c = (n - n_i)$ while $a = -(n-n_i)$,with *n* number of levels, n_i number of the *i* sublevel ($i = 1$ is for the innermost, and then it increases until the biggest external level).

This means that, at the *i*-level, μ_{i-1} is the local coefficient of friction and following the same concept:

$$\mu_i = f_i(\mu_{i-1}, z_1, z_2, \beta) = \gamma[f_1(\mu_0, z_1, z_2, \beta)] \tag{2.11}$$

$$F_x = F_z \frac{\sin\varphi_P \sqrt{1 + \tan^2\varphi_P \cos^2\beta} + \mu_{i-1}\cos\beta}{\cos\varphi_P \sqrt{1 + \tan^2\varphi_P \cos^2\beta} - \mu_{i-1}\tan\varphi_P \cos\beta} = F_z H_x(\mu_{i-1}, \varphi_P, \beta) \tag{2.12}$$

$$F_y = F_z \frac{\mu_{i-1}\sin\beta}{\cos\varphi_P \sqrt{1 + \tan^2\varphi_P \cos^2\beta} - \mu_{i-1}\tan\varphi_P \cos\beta} = F_z H_y(\mu_{i-1}, \varphi_P, \beta) \tag{2.13}$$

$$F_z = K_i u \tag{2.14}$$

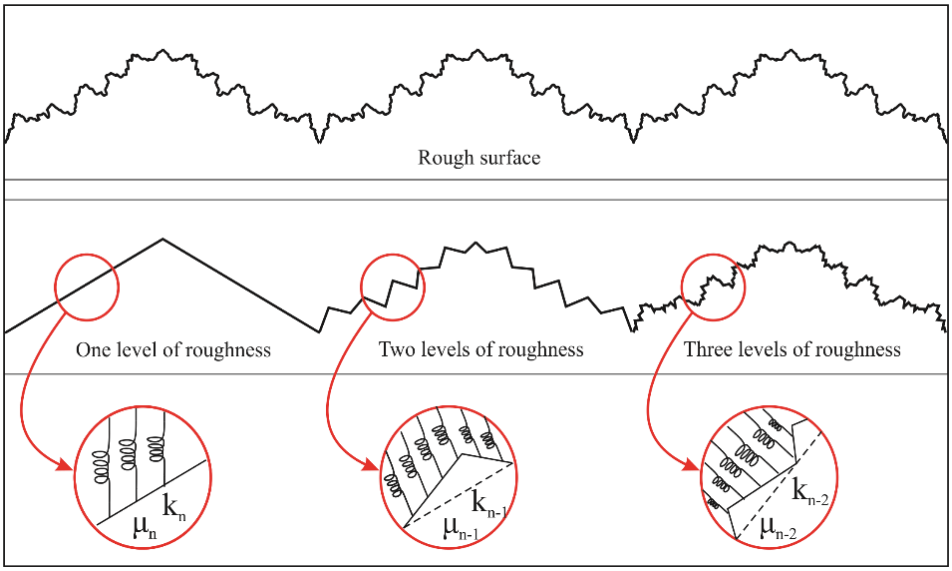

Figure 2.11 How to model different levels of roughness.

The function γ contains all the contributions of levels from 2 to i. This means that the coefficient of friction of level i always depends on the local coefficient of friction of the innermost level.

The reaction forces for the whole asperity are expressed as follows:

$$R_x = R_z^{(1)}\left(\frac{\sin\varphi_{P,1}\sqrt{1+\tan^2\varphi_{P,1}\cos^2\beta}+\mu_{i-1}\cos\beta}{\cos\varphi_{P,1}\sqrt{1+\tan^2\varphi_{P,1}\cos^2\beta}-\mu_{i-1}\tan\varphi_{P,1}\cos\beta}\right) + R_z^{(2)}\left(\frac{+\sin\varphi_{P,2}\sqrt{1+\tan^2\varphi_{P,2}\cos^2\beta}+\mu_{i-1}\cos\beta}{\cos\varphi_{P,2}\sqrt{1+\tan^2\varphi_{P,2}\cos^2\beta}-\mu_{i-1}\tan\varphi_{P,2}\cos\beta}\right) \tag{2.15}$$

$$R_y = R_z^{(1)}\left(\frac{\mu_{i-1}\sin\beta}{\cos\varphi_{P,1}\sqrt{1+\tan^2\varphi_{P,1}\cos^2\beta}-\mu_{i-1}\tan\varphi_{P,1}\cos\beta}\right) + R_z^{(2)}\left(\frac{\mu_{i-1}\sin\beta}{\cos\varphi_{P,2}\sqrt{1+\tan^2\varphi_{P,2}\cos^2\beta}-\mu_{i-1}\tan\varphi_{P,2}\cos\beta}\right) \tag{2.16}$$

In particular, if $\beta = 90°$ and the surfaces are defined as triangular asperities, the upper surface slides perpendicularly (along the y direction) on the other, these expressions can be simplified into:

$$\begin{cases} \mu_n = \dfrac{\mu_0}{2^n}\left[\dfrac{\psi}{\cos\varphi} + 1\right]^n & \varphi_1 = \varphi_2 \quad \varphi_3 = \varphi_4 = 0 \end{cases} \tag{2.17}$$

$$\begin{cases} \mu_n = \dfrac{\mu_0}{(\cos\varphi)^n} & \varphi_1 = \varphi_2 = \varphi_3 = \varphi_4 \end{cases} \tag{2.18}$$

Thanks to the introduction of hierarchy, the HASLFM firstly computes the friction coefficient of the inner level (on the smallest scale), and then the coefficient of the others. Changing a level means hypothetically changing the scale of the problem (supposing that the physics and the geometry of the problem are preserved). To obtain this effect, different reference lengths characterize each level (between two consecutive levels they differ in one order of magnitude). As in the previous cases, these results are obtained for distinct values of β, for both 2D and 1D roughness (wedge asperities or generic shape).

Hierarchy non-linearly enhances the friction coefficient, and the coefficient of each level depends on the previous one. By defining hierarchical sublevels in both upper and lower surfaces, the friction coefficient increases faster than in the case of one hierarchical surface and a second single-level surface.

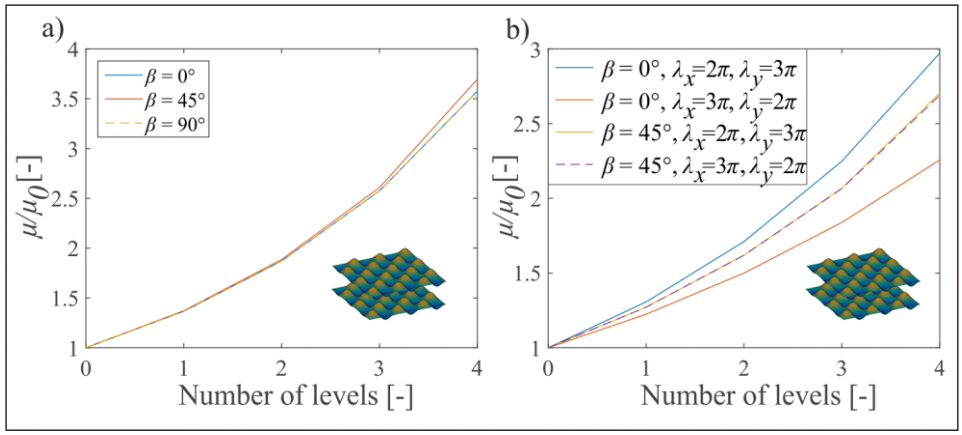

Figure 2.12 Hierarchical friction for 2D roughness. a) Variation of the friction coefficient between two symmetric self-similar hierarchical asperities. Three different directions of sliding (β) are

considered.. b) Variation of the friction coefficient between two asymmetric self-similar hierarchical asperities. Two different directions of sliding (β) have been considered as a prof that, if the asperities are not symmetric, the frictional response varies in a more significant way with respect to β.

In Figure 2.12, the variation of the friction coefficient between two symmetric or asymmetric self-similar hierarchical asperities is reported. Three different directions of sliding (β) are considered in Figure 2.12 a. For surfaces with 2D symmetric roughness, the same behaviour is found with relative sliding along x and y directions, proving again that the frictional response is symmetric. However, similar results are obtained also for other β, e.g. 45°, meaning that the sliding direction is not the preponderant factor modifying the friction coefficient, even in the presence of hierarchical surfaces. On the contrary, if asymmetric asperities are adopted, the frictional response varies in a more significant way with respect to β. In particular, the results obtained for β equal to 0° or 45°, with surfaces characterized by $\lambda_x = 2\pi$ and $\lambda_y = 3\pi$, or by $\lambda_x = 3\pi$ and $\lambda_y = 2\pi$ are reported. The difference among the sliding directions is more significant, while the results for $\beta = 45°$ are the same, as shown in Figure 1.13 c.

The effects of hierarchy in the presence of 1D sinusoidal asperities are also studied (Figure 2.13 a-b) and wedge asperities (Figure 2.13 c-d), both in case of the same shape or in the presence of one flat surface. For wedge asperities it is possible to compare the numerical results with the analytical solutions previously obtained (closed solution only for $\beta = 90°$).

By adopting the same simplified solution in the case of sinusoidal roughness (where we adopted the average of the slopes as φ), it is possible to make a qualitative prediction of the variation of the friction coefficient in a hierarchical surface, even if underestimated (red curves in Figure 2.13 a-b), due to the slope approximation.

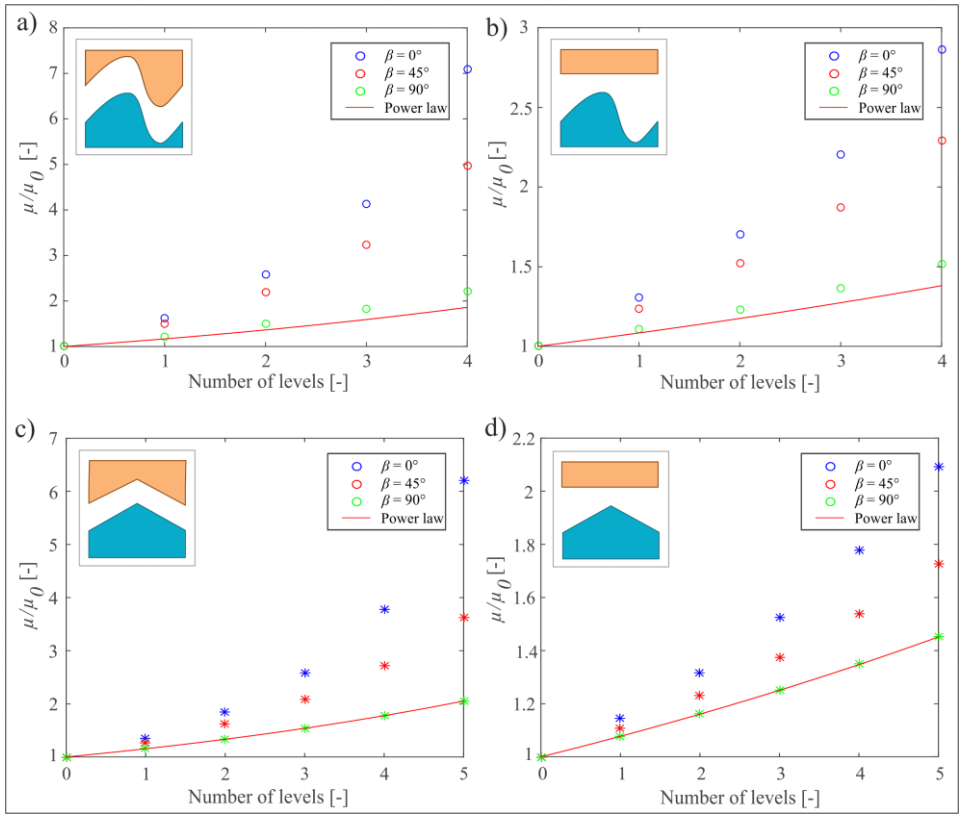

Figure 2.13 Hierarchical friction. a) Variation of the friction coefficient between two sinusoidal hierarchical asperities. Three different directions of sliding (β) are considered. The theoretical prediction, which is the exact solution in case of wedge asperities, is reported (red curve). b) Variation of the friction coefficient between a sinusoidal hierarchical surface and a flat surface. Three different directions of sliding (β) are reported. The theoretical prediction, which is the exact solution in case of wedge asperities, is reported (red curve). Hierarchical friction. c) If the surfaces are modelled as hierarchical wedges, friction coefficient is the same as obtained from the power law. Also other directions of sliding (β) have been reported. d) Variation of the friction coefficient between hierarchical wedge asperities. Three different directions of sliding (β) have been considered. In this casetoo, the theoretical prediction perfectly matches the numerical results.

2.4. Coupling hierarchy and wear effects in ALSTM

In the work of Whitehouse and Archard in 1970, it was found that from the profile of a rough surface after a single passage of a lubricated slider, the fine roughness (i.e. the roughness associated to the smaller levels) was removed, while the main roughness was preserved. Following the concept of such experiments, the effect of hierarchy is coupled with wear mechanisms, to provide a model that can describe and predict the variation of the frictional behaviour after a certain sliding distance, in the presence of sliding wear.

It is assumed that, if wear affects hierarchical surfaces, the first consumed sublevel is the innermost one. When its roughness is removed, the second to last levels begins to be subjected to wear.

This means that the coefficient of friction of the innermost level tends to its local coefficient of friction μ_0 and each level follows, until the external level is worn and thus the global coefficient of friction becomes that of a flat surface (μ_0):

$$\mu_n \rightarrow \mu_{n-1} \rightarrow \cdots \rightarrow \mu_1 \rightarrow \mu_0$$

After a time equal to T_w ($B = 0, t_0 = 0$), the global coefficient of friction of a certain level *i* is reduced to its local coefficient of friction $\mu_{0,i}$ (and the number of hierarchical levels decreases from *n* to *n-1*).

In the presence of 2D roughness, the time needed to wear away a certain level *i* is obtained from the expression of the reduction coefficient *B*, when the latter is equal to zero:

$$T_{w,i} = \frac{\iint_{x_0,y_0}^{x_f,y_f} z(x,y)\, dx\, dy}{Wv} \tag{2.19}$$

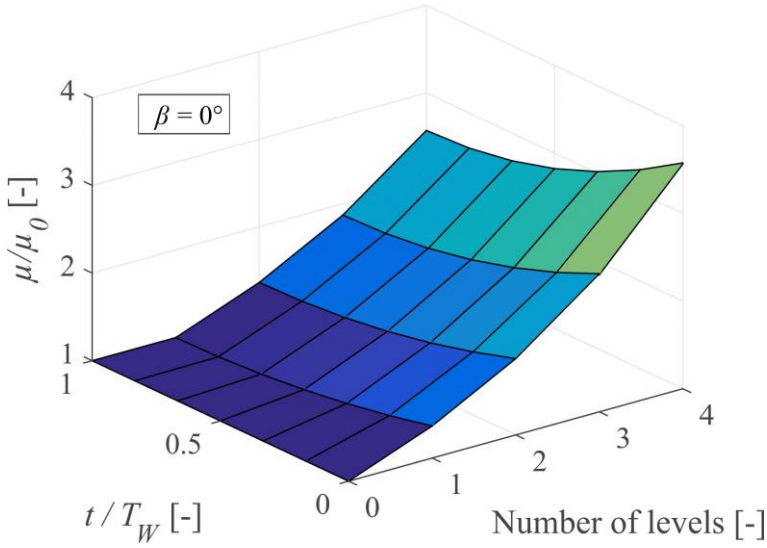

Figure 2.14 Variation of the global coefficient of friction as a function of wear and roughness levels. Every outer level is influenced by the inner one, so that wear induces a reduction of each global coefficient of friction associated to a certain level i. After a time equal to T_W the innermost level becomes flat, so that the coefficient of friction of each level at the end of this wear cycle tends to its local friction coefficient. Level 0 is the local coefficient of friction.

The effect of hierarchical wear is introduced within the HASLFM, in order to show the decrease in the global coefficient of friction associated to each roughness level. In Figure 2.14, the frictional and wear behaviour between two 2D rough hierarchical surfaces is reported. T_W is the time needed to wear away the innermost level (level 1). As stated before, each outer level is linked to the previous ones and influences the following. A change in the friction coefficient at a certain level *i* affects all the upper levels, as it is clearly visible in Figure 2.14. In particular, after a time equal to T_W, the global coefficient of the level *i* tends to the local coefficient of friction of that level, i.e. the global coefficient of friction of the level *i-1*.

2.5. Conclusions

In this Chapter, some aspects related to friction are introduced, as the effects of adhesion and wear, studying the case of both sinusoidal 2D and 1D roughness,

and extending it to wedge roughness. Hierarchy has been included, since friction can be considered a multiscale hierarchical phenomenon.

This study shows that, since the friction coefficient strongly depends on the roughness of the involved surfaces, if multiple self-similar hierarchical levels are present, they contribute to enhancing the friction coefficient in a non-linear way, which collapses in a power law in the particular case of $\beta = 90°$ and wedge shaped asperities.

Adhesion occurs when springs in tension are introduced to model the interaction at the interface. This leads to an increase in the total compression force acting on the asperities, resulting in an increase in the apparent friction coefficient and providing a tangential force even when the applied load is equal to zero.

Furthermore, wear has been described as a process that reduces the friction coefficient and smooths the asperities. The effect is more evident if the sliding occurs in the *x* direction for 1D roughness ($\beta = 0$).

Finally, by combining wear and hierarchy, it is possible to model how the friction coefficient of hierarchical surfaces is modified due to sliding wear, providing useful insights into this complex field.

Chapter 3

3. Modelling the ice friction of rough surfaces: an application of the 1D-ALSFM to experiments

The study of friction between metals and ice is as complicated as it is important in a wide range of fields, from ice sports to motorized traffic (Colbeck et al. 1975; Higgins et al. 2008; Roberts and Richardson 1981). That being said, the debate behind the origin of the low friction coefficient characterizing ice surfaces is still open even after decades of experimental and theoretical research on both saline and freshwater ice (Hatton, Sammonds, and Feltham 2009; Jacobsen, Scherer, and Schulson 2015; Kietzig, Hatzikiriakos, and Englezos 2010; Lishman, Sammonds, and Feltham 2011; Schulson 2015; Schulson and Fortt 2012; Wallen-Russell and Lishman 2016).

The friction coefficient of a solid surface sliding on ice is related to the existence of a thin layer of water between the slider and the ice itself. There are three main mechanisms governing the formation of this layer (Kietzig et al. 2010): *surface melting*, *pressure melting* and *frictional melting*. *Surface melting* is a spontaneous generation of a thin layer of melted ice (with thickness in the order of magnitude of few nanometers) without any contact with other bodies and without any applied pressure, when the temperature approaches the melting value. The origin of this phenomenon, observed in a number of solid surfaces, is still under debate, although the most prevailing theories indicate the minimization of free surface energy as the main cause (Kietzig et al. 2010). The *pressure melting* is responsible for the decrease of the melting ice temperature by applying a pressure. The *frictional melting* is generated by the heat dissipated by the friction force; this heat increases the interface temperature and is considered as the most relevant mechanism in the formation of water at the interface in sliding systems (Bowden

and Hughes 1939; Fülöp and Tuononen 2013; Higgins et al. 2008; Kriston et al. 2016; Nyberg et al. 2013). The thickness of the water layer defines the lubrication regime of a given sliding system and is influenced by temperature, normal force and sliding velocity (Kietzig et al. 2010; Klapproth et al. 2016; Stamboulides, Englezos, and Hatzikiriakos 2012). Consequently, by varying the experimental parameters, it is possible to explore all lubrication regimes, from boundary to hydrodynamic (Figure 3.1). According to the literature, surface roughness has a great importance since it defines the height of the asperities interacting with each other (Ducret et al. 2005; Kietzig et al. 2010; Sukhorukov and Marchenko 2014).

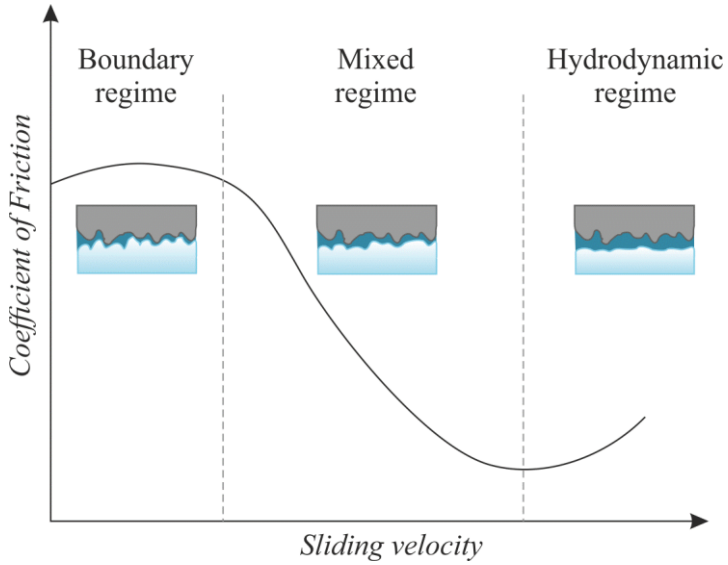

Figure 3.1 Stribeck curve generalized for ice friction: the friction coefficient is a non-linear function of the sliding velocity (proportional to the thickness of lubricant (water). Three regimes are highlighted, due to different asperity interaction and increasing water layer thickness h.

In *boundary* (or *dry*) lubrication regime the frictional behaviour is governed by the real contact area between the solids, in which adhesion is the main source of friction and heat dissipation (Bowden, Tabor, and Palmer 1951; Kietzig et al. 2010; Makkonen 2012; Bo N. J. Persson 2000). In this regime, the thickness of the liquid water is very small, in the order of magnitude of few molecular layers (Makkonen and Tikanmäki 2014; Petrenko and Whitworth 1999). By increasing

the sliding velocity, the thickness of this liquid-like layer increases and supports the load of the slider; this condition is typical of the *mixed* lubrication regime. The interfacial conditions of this lubrication regime are still not fully clarified although there are different theories (Kietzig et al. 2010; Makkonen and Tikanmäki 2014). In particular, Kietzig et al. 2010 assume that mixed lubrication occurs when the temperature at the contact point is greater than the melting temperature of ice, but the thickness of the water layer is still smaller than the roughness of the counterpart's surface. With this assumption, both solid-solid and lubricated contact coexist at the interface. In contrast, Makkonen and Tikanmäki 2014 assume that at the actual contact point the temperature rises to the melting point, but not over this value. The contact is,therefore fully lubricated, even with very low thickness of the layer of water, and there is no longer solid-solid interaction between the surfaces. All the experimental data reveal a dependence of the coefficient of friction (μ) on sliding velocity (v) as $\mu \sim 1/\sqrt{v}$ (Bäurle et al. 2007; Marmo, Blackford, and Jeffree 2005).

In the *hydrodynamic regime*, the coefficient of friction increases proportionally with $\sqrt{v}$ (Albracht 2004; Jones et al. 1994; de Koning, de Groot, and van Ingen Schenau 1992). Kietzig et al. 2010 estimate that this regime starts when the thickness of the water layer becomes greater than the average roughness of the involved surfaces.

In this Chapter, a study undertaken with the collaboration of the University of Modena and Reggio Emilia (Spagni et al. 2016) is presented, in which the role played by the surface of the slider in terms of roughness and topography on the friction regimes is examined. Tribological tests of steel-ice contacts have been performed, by varying temperature and sliding velocity. Furthermore, the dependence of friction on surface morphology has been studied by inducing different degrees of roughness on stainless steel surfaces. Then, the analytical 1D-ALSFM has been applied to the experimental data, directly correlating the surface roughness to the friction coefficient.

3.1. Experimental procedure

The ice samples are obtained by freezing distilled water in a commercial freezer unit at -8 C. Thin layers of water are frozen on the top of each other in order to minimize cracking and bubble formation and to produce a polycrystalline surface (Kietzig et al. 2010). Figure 3.2 shows an optical image of the surface replica. Curved grain boundaries of ice and their characteristic 120° angles are clearly visible. In Figure 3.2, sublimation pits ("etch pits") are visible as well. These spots are created by a higher sublimation speed at locations where dislocation slip lines cross the surface (Fülöp and Tuononen 2013; Kriston et al. 2016) and the ice surface does not go through a long aging process, so no frost deposition is visible. The average roughness (R_a) of the ice is measured by stylus profilometer on a replica of the surface, prepared using a vinylpolysiloxane-based liquid thermo-polymer (Bäurle et al. 2007), obtaining a value of 100±10 nm.

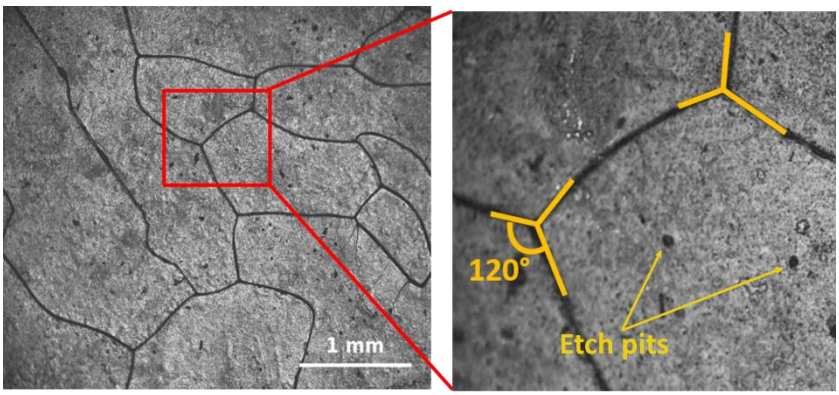

Figure 3.2 Optical microscopy image of an ice surface replica. The magnification shows the characteristic 120° angles formed by the grain boundaries at almost each cross. Etch pits are also visible.

On the stainless-steel pins, a controlled surface roughness is induced through mechanical polishing and sand-blasting. Three different pins are produced, labelled #1, #2 and #3. The pin #1 is polished with alumina slurry (1-3 µm

diameter), while pins #2 and #3 are grinded through sand-blasting (grit 320 and 180 respectively).

As before, surface morphology is measured through a stylus profilometer (3D profiles shown in Figure 3.2). Different parameters are used to characterize the surface roughness (Table 3.1), briefly described in the following:

- Average roughness, R_a: it gives a good general description of the height variation along the profile, but without any information about its morphology;
- RMS slope profile R_{dq}: it is calculated as the root mean square of the slope of the profile over the assessment length;
- Skewness S_k: it gives an overview of the symmetry of the profile with respect to the mean line, and it is sensitive to the presence of deep valleys and high peaks. A perfect symmetrical distribution shows $S_k = 0$;
- Kurtosis K_u: it measures the sharpness of the profile amplitude probability density function $p(y)$. It can be useful to differentiate surfaces with the same R_a but different shape;
- Fractal dimension D: it is a quantity related to fractal geometry. It is related to the scaling structure of the roughness profile and to its self-similarity;
- Contact angle θ_c: quantifies the wettability of a solid surface.

All of these parameters show a monotonic trend, except for the contact angle which is characterized by the same value (within the experimental error) for each sample. R_a and R_{dq} of pin #1 are one order of magnitude lower than those of pin #2 and #3. Furthermore, the roughness of pin #1 is almost the same as the one of the ice surface (see below).

The tribological tests are performed in pin-on-disc configuration on a UMT3-CETR tribometer (http://www.cetr.com/eng/products/umt-3.html) enclosed in a thermally insulated chamber, where the temperature is controlled by a flow of cold dry air. The system reached temperatures down to -25°C, with an error of ±1°C. All the tribological tests are performed with a constant normal load of 15 N,

(nominal pressure of 0.085 MPa), constant environmental temperature (between -17°C and -2°C) and increasing sliding velocity in consecutive steps (from 0.025 m/s to 1m/s), each one of 2 minutes length for a total duration of 16 minutes (8 different speeds were tested).

Pin	R_a [µm]	R_{dq} [°]	S_k	K_u	D	θ_c
#1	0.11±0.02	7.3±1.0	2.35±0.05	9.3±0.4	2.763±0.005	52±2
#2	1.4±0.1	27.2±1.5	1.2±0.3	6.4±1.2	2.359±0.005	63±10
#3	2.6±0.1	33.6±1.1	0.9±0.3	3.4±0.9	2.276±0.005	55±8

Table 3.1 Roughness parameters for the stainless-steel pins: average roughness (Ra), RMS slope (Rdq), skewness (Sk), kurtosis (Ku), fractal dimension (D) and contact angle (θc).

Unfortunately, the temperature of the ice can not be measured. However, the ice sample is left in the tribometer chamber for about one hour, which is enough for the ice to reach the same temperature of the surrounding environment.

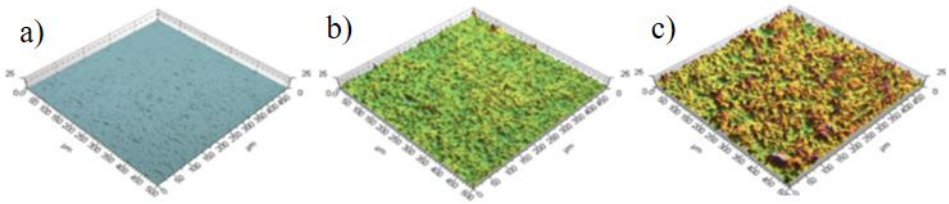

Figure 3.3 3D surface profile of the stainless-steel pins. a) Pin #1, which is characterized by the smoothest surfaces. b) Pin #2 and c) pin #3.

3.2. Experimental results

To improve the accuracy and reliability of the experimental results and to avoid systematic errors, for each test a newly prepared ice surface wias used and four different measurements are made for each temperature. Here, the average of all measurements is reported (Figure 3.4). At the beginning of each test, a short sliding run is done on the ice surface, in order to remove or reduce ice macroscopic

asperities that could compromise the stability of the tests. This preliminary run is characterised by a load of 2 N and a 3-time rotation of the disk.

Figure 3.4 shows values of friction coefficient obtained for steel on ice versus the sliding velocity for the three pins, at different ambient temperatures between -2° and -17° C.

One of the first deductions is that the operating temperature (presumably, the bulk temperature of slider and ice) does not significantly affect the values of the friction coefficient, probably due to the experimental setup. Using a pin-on-disc configuration, the repeated passages of the pin on the same circular track result in frictional heat dissipation causing an increase in temperature at the steel-ice interface.

From the thermal equilibrium of the dissipation of frictional heat during the contact and the refreezing between two consecutive passages, the interface temperature saturates at a value larger than the one of the steel, of the ice bulk and of the surrounding environment (Dash 2003). A quick calculation demonstrates that, with a speed of 0.1 m/s (80 rpm), the time between two passages over the same spot is less than 1 second. This caused an increase in the temperature of the ice surface and of the steel slider surface until the achievement of balance. Thus, basically, after a short initial phase, the coefficient of friction reaches a steady state where both the interface temperature and all the other conditions do not vary. The thickness of the water layer produced by melting in this state is independent on the initial conditions, thanks to the two competitive effects contributing to his formation, that is the frictional melting and the squeeze-out of the water (as stated by (Colbeck 1988)).

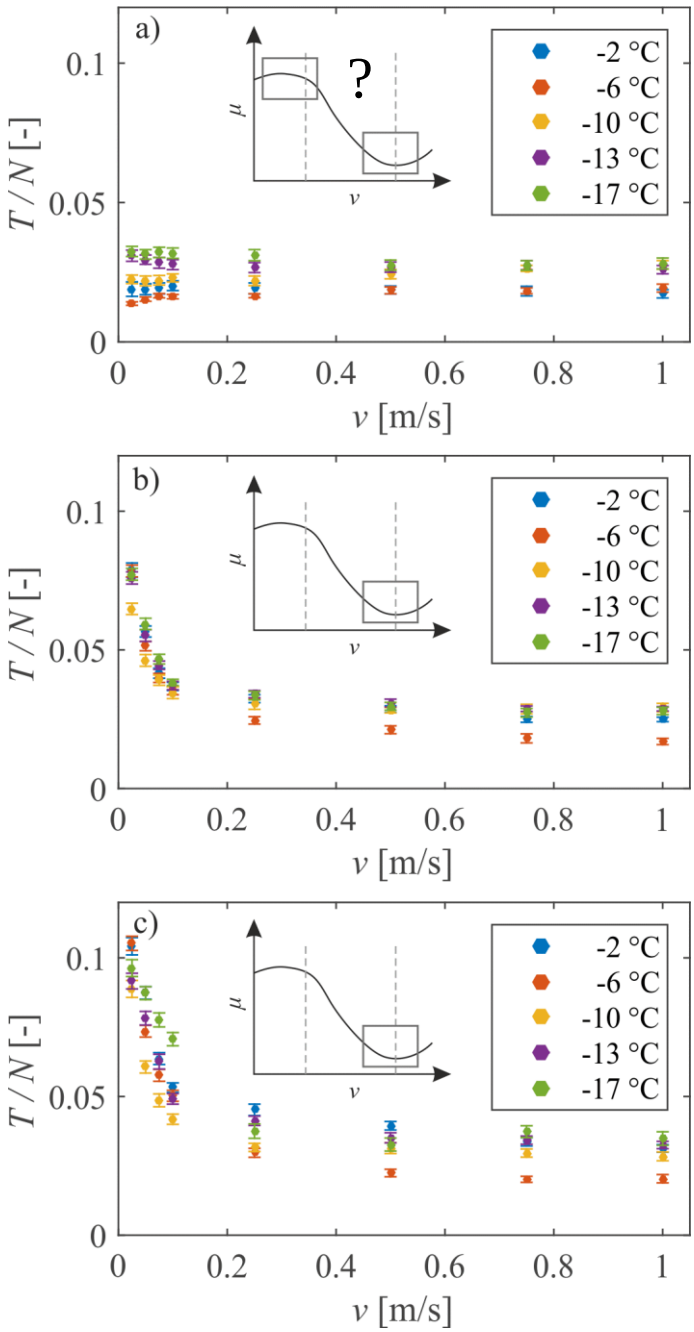

Figure 3.4 Friction coefficient results obtained from the pin-on-disc tests at increasing sliding velocity. a) pin #1, (b) pin #2 and (c) pin #3. The tests have been performed at various temperatures from -2 °C to -17 °C.

Another consequence, inferred from Figure 3.4, is that the frictional behaviour is quite different for pin #1 (the smoothest one) and pin #2 and #3, (roughness about 1 order of magnitude larger).

Results from pin #2 and #3 shows decreasing friction coefficient values as the sliding velocity increases, in which the decrease is initially quite sharp. Between 0.025 m/s and 0.3 m/s, the coefficient of friction decreases from 0.09÷0.11 (pin #3) and 0.06÷0.08 (pin #2) down to 0.03÷0.05. Then, the dependence of the coefficient of friction on the sliding velocity markedly reduces and the friction curve becomes almost flat, with values of 0.02÷0.04. This trend is typical of the transition region between mixed and hydrodynamic friction regimes, as highlighted by the grey squares in the insets of Figure 3.4 b and c.

Despite the very similar trends, the difference of friction coefficients between pin #2 and pin #3 is a consequence of the roughness difference between the two steel surfaces.

On the contrary, the results from pin #1 showed a nearly constant coefficient of friction (roughly between 0.02 and 0.03) along the entire sliding velocity range, indicating that the system is probably in a different lubrication regime. However, the assignment to a specific lubrication regime is quite difficult because a constant coefficient of friction behaviour is typical of either the boundary friction regime or the minimum between the mixed and the hydrodynamic regime (see the grey squares in Figure 3.4 a with the question mark). The small values of coefficient of friction seem to support the second hypothesis because they are typical of the mixed lubrication regime. Nevertheless, in the absence of high wear effects (e.g. ploughing friction or cracking), the low shear stress of ice is characterised by low values of coefficient of friction, even in the dry lubrication regime. This condition could actually be applied in the present case, thanks to the very low roughness of pin #1 and to the low applied pressure. The pin has nearly the same roughness of the ice surface, and its low waviness leads to a high real contact area and, furthermore, the roughness profile is quite broad (R_{dq} = 7.3, Table 3.1). These

features, matched with a nominal applied pressure of 0.085 MPa (nearly two orders of magnitude below the breaking pressure of ice), suggest that phenomena like ploughing friction and cracking of the ice bulk close to the surface are negligible.

3.3. Extended 1D-ALSFM to the ice friction

Ice friction model

In the literature there are several theoretical models describing ice tribology (Colbeck 1988; Evans, Nye, and Cheeseman 1976; Kietzig, Hatzikiriakos, and Englezos 2009; Klapproth et al. 2016; Makkonen and Tikanmäki 2014; Oksanen and Keinonen 1982), each attempting to estimate the coefficient of friction of ice and accounting for the interdependence of the different involved parameters.

One of the most complete models was developed by Makkonen (Makkonen and Tikanmäki 2014), where the only source of friction is the shear strength τ of the water layer, due to its viscosity:

$$T = \tau A = \frac{\eta v}{h} A \tag{3.1}$$

$$\mu_{wet} = \frac{T}{N} = \frac{\eta v A}{h N} \tag{3.2}$$

where A is the real contact area, v is the sliding velocity, N is the applied normal load, η and h are respectively the viscosity and the thickness of the liquid-like layer.

One of the most difficult parameters to estimate is the thickness of this layer of melted ice. The problem may be solved by considering the thermal balance between ice and steel.

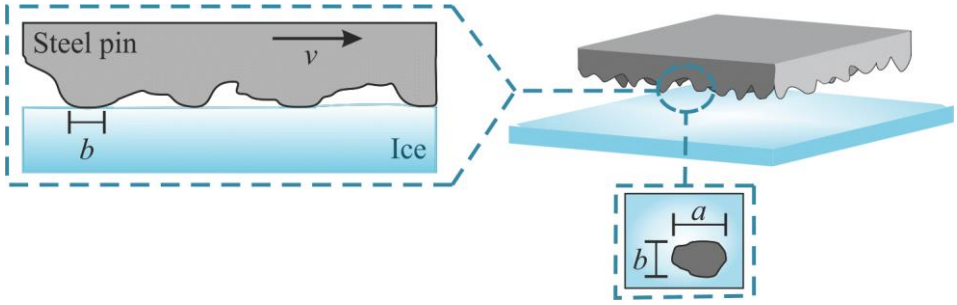

Figure 3.5 Schematic illustration of the contact between ice and steel pin. To compute the coefficient of local friction a number of contacts n of length b and width a is assumed. The sliding velocity is v.

A rectangular contact asperity moving on ice at a certain sliding velocity v is assumed (Figure 3.5) and the frictional energy produced per unit contact is (Makkonen and Tikanmäki 2014; Oksanen and Keinonen 1982):

$$Q_f = \frac{\mu N b}{n} \tag{3.3}$$

In addition, if the temperature of the steel-ice interface is the same as the ice melting temperature, the generated heat flux is the sum of the energy flow from the contact to ice (Q_{c1}) and the energy flow from the contact into the pin (Q_{c2}):

$$Q_c = Q_{c1} + Q_{c2} = ab\Delta T_1 \sqrt{\frac{b}{2v}}\sqrt{k_1 c_1 \rho_1} + ab\Delta T_2 \sqrt{\frac{b}{2v}}\sqrt{k_2 c_2 \rho_2} \tag{3.4}$$

a and b are respectively the width and the length of the contact, while all the other terms are reported in Table 3.2. Finally, Q_m is the energy required to generate a liquid like layer of thickness h, length b and width a:

$$Q_m = abhL\rho \tag{3.5}$$

(see Table 3.2. for parameters explanations).

The thermal equilibrium imposes that the energy dissipated through friction is equal to the sum of the heat flux and the melting energy (Makkonen and Tikanmäki 2014):

$$Q_f = Q_c + Q_m \tag{3.6}$$

From this equilibrium, it is possible to estimate the thickness of the liquid like layer h produced during the sliding and then the friction coefficient μ_{wet}, by assuming $a = b$ and the hardness of ice $H_i = N/A = N/(nab)$ (Makkonen and Tikanmäki 2014):

$$h = \frac{1}{l\rho}\left(\frac{\mu N}{na} - \sqrt{\frac{b}{2v}}\gamma\right) \tag{3.7}$$

$$\mu_{wet} = \frac{1}{H_1\sqrt{a}} \cdot \frac{1}{2\sqrt{2v}}\left(\gamma + \sqrt{\gamma + 8\eta L\rho v^2}\right) \tag{3.8}$$

Where

$$\gamma = \Delta T_1\sqrt{c_1 k_1 \rho_1} + \Delta T_2\sqrt{c_2 k_2 \rho_2} \tag{3.9}$$

$$\Delta T_i = T_i - T_m \tag{3.10}$$

In the model presented by Makkonen (Makkonen and Tikanmäki 2014), the role of the surface morphology is included in an approximate manner as it occurs only in the definition of *a*, the characteristic length of the real area of contact between the ice and the slider, which was fixed to 1 mm. With such a great contact length, the dependence on the roughness of the slider is not included in the model and so only the low-frequency waviness of the surface affects the tribological behaviour of the system.

In order to include the contribution of the surface roughness to the tribological behaviour of the system, the 1D-ALSFM described in Chapter 1 is applied and validated with the present study.

List of symbols		Numerical values		
		Ice	Steel	Water
a	Contact length			

T_i	Temperature (°C)	-17 to -2			
T_m	Melting temperature of ice (°C)	(Kriston et al. 2016)			
v	Sliding velocity (m/s)	0.025 to 1			
H_i	Ice hardness (MPa)	(Kriston et al. 2016)			
$\boldsymbol{\rho}_i$	Density (Kg m^{-3})		916	7750	
$\boldsymbol{\rho}_w$	Water density at 0°C (Kg m^{-3})				1000
$\boldsymbol{\eta}_w$	Water viscosity at 0°C (Kg m^{-1} s^{-1})				$1.76 \cdot 10^{-3}$
k_i	Thermal conductivity (W m^{-1} K^{-1})		2.2	20	
c_i	Specific heat (J Kg^{-1} K^{-1})		2090	460	
L	Water latent heat (J Kg^{-1})				$330 \cdot 10^3$

Table 3.2 List of used symbols and their numerical values; i=1 for ice, i=2 for slider. The contact length a is calculated from data analysis in the next section.

Surface roughness

The ALSFM considers the sliding motion between rough surfaces and directly correlates the effects of different roughness to the friction coefficient. This model has been introduced and described in Chapter 1, in which the contact between two surfaces has been modelled by a set of springs with only longitudinal compliance. During the sliding of one surface on the other, the vertical springs have to comply with the movement, by modifying their length, becoming compressed or elongated. This length variation is reflected on the elastic forces that the two surfaces exchange. Furthermore, the moving surface can change the direction of sliding (v_0 is the sliding velocity), so that it could be perpendicular or not to the asperities of the fixed surface (Figure 3.6).

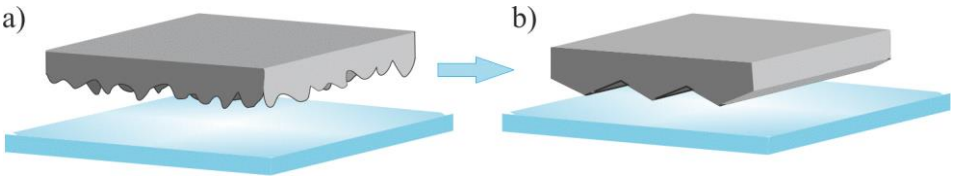

Figure 3.6 a) Schematic illustration of the contact between ice and steel pin and b) how it is converted into the 1D-ALSFM developed in Chapter 1. The interaction between ice and steel is modelled by a set of springs with only longitudinal compliance.

Being R_z the global reaction force along the vertical direction and $R_{x,y}$ the global reaction force acting on the ice-plane, the total coefficient of friction f is expressed as in Eq. (1.13).

In order to evaluate this friction coefficient, it is necessary to determine the reaction forces in the global reference system *xyz*, by analysing at first the contribution of a single spring. All the details of the calculation are reported in Chapter 1.

This model considers the local interaction between the two surfaces through the introduction of a generic local coefficient of friction (named μ_0), which does not consider any morphological effect and does not specify any physical mechanism at its base. In order to contextualize the model to the previous ice friction model (Makkonen and Tikanmäki 2014), the generic local Coefficient of friction μ_0 was substituted with μ_{wet} ,which is the coefficient obtained previously in Eq. (3.8) and does not consider the effects of surface roughness.

3.4. Results

To apply the 1D-ALSFM to the tribological system reported in this work, two particular cases are selected, namely $\beta = 0°$ and $\beta = 90°$, where β is the direction of sliding. In both cases, the steel asperities are considered symmetrical, adopting $\varphi_1 = \varphi_2 = \varphi$ while the ice (whose roughness is negligible with respect to the steel roughness) is assumed to be flat ($\varphi_3 = \varphi_4 = 0$). The asperity slope refers to the pin roughness, thus equal to R_{qd}, one of the parameters obtained from a stylus

profilometer. For $\beta = 0°$, the sliding appears to be against the wedge asperities and the coefficient of friction is maximum. On the contrary, $\beta = 90°$ leads to the minimum coefficient of friction.

The expressions for these two cases refer to Chapter 1 and are here reported:

$$f^u = \frac{\mu_{wet}\left(2 - \sin^2\varphi\,(1 + {\mu_0}^2)\right)}{2\left(1 - \sin^2\varphi\,(1 + {\mu_0}^2)\right)} \tag{3.11}$$

$$f^l = \frac{1}{2}\mu_{wet}\left(\frac{1}{\cos\varphi} + 1\right) \tag{3.12}$$

where f^u and f^l are respectively the upper and the lower limit of the coefficient of friction. All the possible orientations of the sliding motion are thus automatically considered and the real value of the coefficient of friction is included between these upper and lower limits.

Since the shear strength of a liquid layer is the only source of friction in this picture, a further hypothesis is introduced, assuming that the real contact area is entirely covered by a water layer and the contact during the sliding motion is fully lubricated. This hypothesis does not exclude the presence of ploughing by the slider asperities into the ice, but it consideres this presence to be mediated by a thin layer of water.

Furthermore, the model describes the motion along a straight line,while friction experiments are performed in pin-on-disc configuration. One of the hypotheses of the model is that the slider always runs on a new ice surface, whose surface temperature is the same as the bulk. In the rotational real case, conversely, the slider performs periodically repeated passages over each point of the ice track, with a short refreezing time due to the short radius of the track and to the sliding speed. With these conditions, the interface temperature of the ice increases, since every passage of the slider dissipates frictional heat. After a few rotations, the temperature at the interface can be considered homogenous and close to the melting point of ice and, accordingly, the terms T_1 and T_2 can be neglected. This

assumption is justified by the very weak temperature dependence of the tribological tests, shown in Figure 3.4.

While the interface temperature is considered as homogenous at melting point of ice, the bulk temperature is not and neither is the hardness of the ice. This parameter is calculated with the bulk temperature since the depth of the stress, caused by the indentation of micrometric asperities, is expected to be of the order of a few microns, while the melting process affects a much lower thickness, very close to the interface. The values of ice hardness in this paper are based on the work of (Makkonen and Tikanmäki 2014), following the relation

$$H_i = C_1 T + C_2 \tag{3.13}$$

with C_1 = -5.08 MPa/K and C_2 = 15.19 MPa.

After all these assumptions, the experimental data are fitted with both Eq. (3.11) and Eq. (3.12), using the contact length a as the only fitting parameter. The best fits are reported in Figure 3.7, Figure 3.8 and Figure 3.9.

The first outcome is that the model fits quite well the experimental results obtained with pins #2 and #3. In the explored range of sliding velocities, both the trends and the absolute values of coefficient of friction are satisfactorily described by the model. It must be stressed that the model introduces the shear stress of the liquid like layer as the only source of friction; therefore, its ability to fit results from pins to #2 and #3 confirms that these sliders operate in a lubricated regime.

On the contrary, the model does not fit satisfactorily the experimental results of pin #1, confirming that, in this case, the system experiences a different lubrication regime.

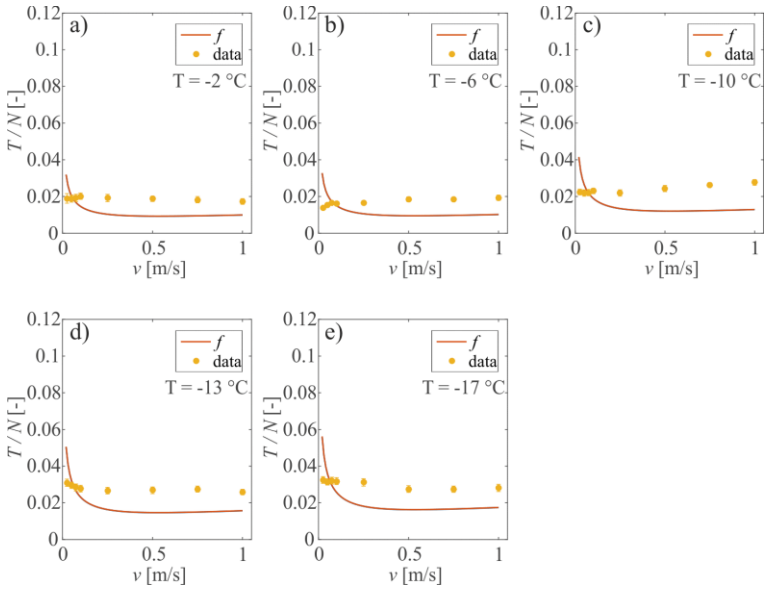

Figure 3.7 Best fits of the experimental data obtained for pin 1# with the 1D-ALSFM (red line) for all the tested temperatures. It is evident that the model is not able to predict pin 1# friction regime, due to the model hypotheses which assume the pin in a mixed lubrication regime.

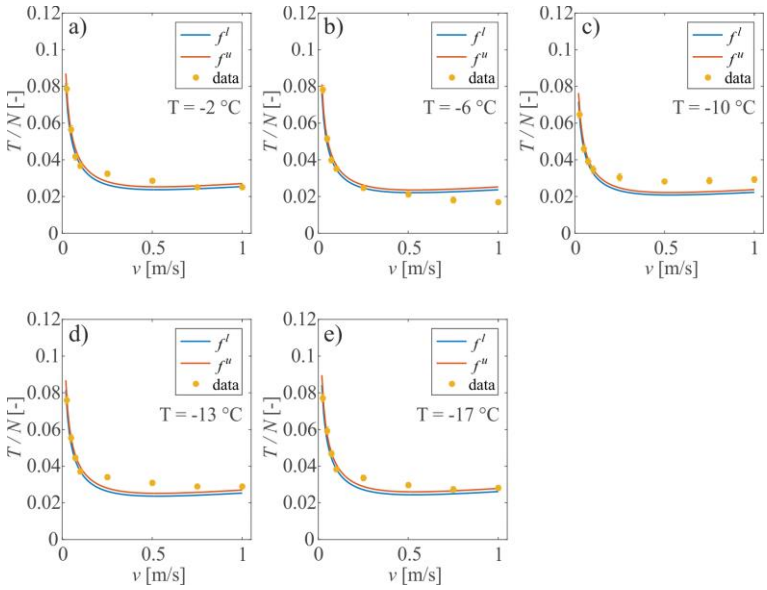

Figure 3.8 Best fits of the experimental data obtained for pin 2# with the 1D-ALSFM for all the tested temperatures (blue line represents the upper values for the coefficient of friction, while red line is for the lower values).

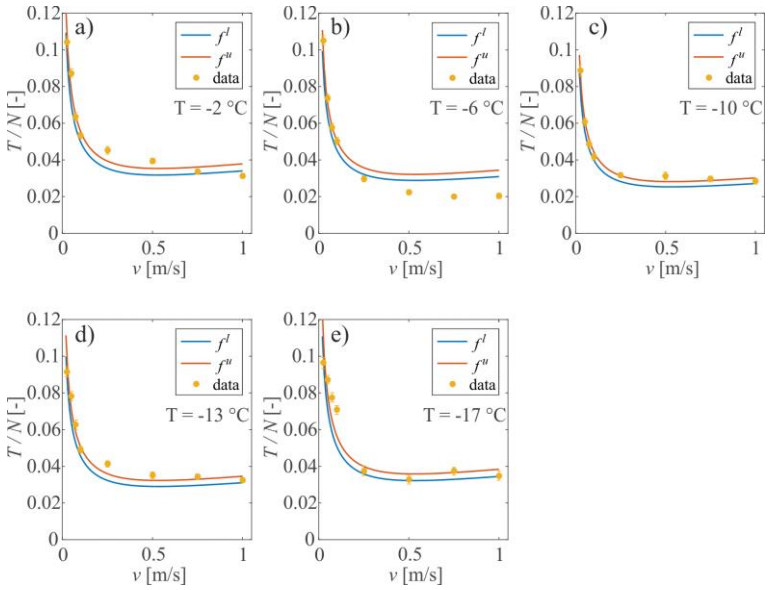

Figure 3.9 Best fits of the experimental data obtained for pin 3# with the 1D-ALSFM for all the tested temperatures (blue line represents the upper values for the coefficient of friction, while red line is for the lower values).

Actual and nominal contact area

In order to compare the results of a obtained with the fitting procedure, a realistic value of the contact length is evaluated. For this purpose, the topography of the surface is approximated with a regular pattern of triangular asperities (Figure 3.10) with the same R_{dq} of the real random surface used in the experimental tests. When that surface is indented with a load N on a flat ice surface, the tips of the asperities penetrate into the ice, both through melting and elasto-plastic deformations. The real contact area (A_{real}) is inversely proportional to the hardness of the ice H_1 (Archard 1957; Makkonen and Tikanmäki 2014), while the nominal contact area (A_{nom}) is inversely proportional to the applied pressure σ (B N J Persson 2000).

$$A_{real} = \frac{N}{H_1} \qquad A_{nom} = \frac{N}{\sigma}$$

It is therefore possible to write the ratio ΔA which represents the ratio between the nominal and real contact area:

$$\Delta A = \frac{A_{real}}{A_{nom}} = \frac{\sigma}{H_1} \tag{3.14}$$

By taking the bearing-ratio curve of the real surface, it is possible to correlate ΔA with the average indentation depth of the triangular asperities.

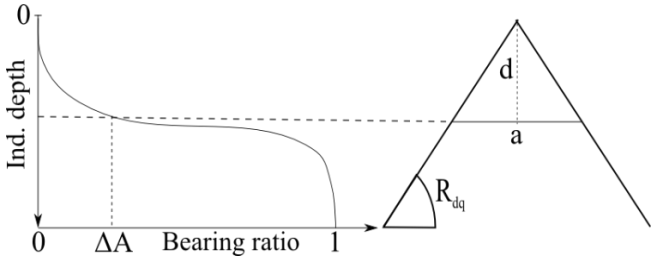

Figure 3.10 Correlation between the model surface and the bearing ratio curve (BRC).

The bearing ratio curve (or Abbott-Firestone curve) describes the texture of the surface profile. It is the cumulative probability density function of the height of the surface profile. This curve is directly obtained from the profilometer and it is correlated with the other roughness parameters reported in Table 3.1. Knowing the percentage of real area with respect to the nominal contact area, Eq.(3.14), the indentation depth associated to that normal load is obtained (Figure 3.10).
With simple geometrical calculations, by assuming a symmetrical wedge asperity, an average value of the contact area length at the interface is found:

$$a = 2\frac{d}{\tan R_{dq}} \tag{3.15}$$

As shown in Figure 3.11, there is good agreement between the values obtained from the fits and from the bearing ratio curve.
Since the ice is considered as a flat surface and the pin material as rigid, the value of a is expected to be of the same order of magnitude as R_a, due to low normal load and thus small plastic deformations.

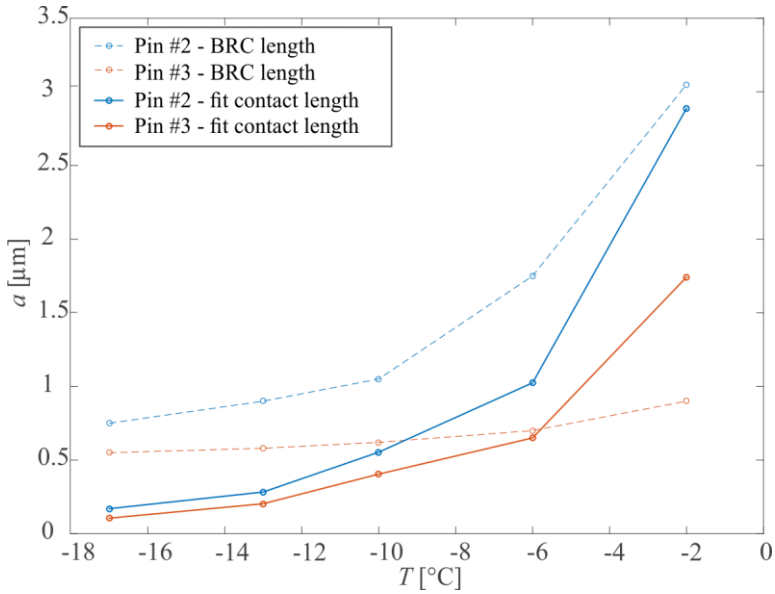

Figure 3.11 A comparison between fitted and estimated contact length a. These results show a good agreement between the fitted values of the contact length a with respect to the contact length obtained from the geometrical calculation. After this validation, it is possible to infer that the values provided from the fit are reliable values

Friction regime for pin #1

As previously stated, the theoretical model, obtained by coupling μ_{wet} and the 1D-ALSFM, is not suitable to fit the behaviour of pin #1, leading to infer that the lubricated regime could be different from the ones of pin #2 and #3. Indeed, the low roughness of pin #1 compared to pins #2 and #3 is expected to induce a lower frictional interface heat and, consequently, a reduced frictional melting. Considering the frictional melting the most relevant mechanism in the formation of the water layer in sliding systems (Bowden and Hughes 1939), pin #1 is expected to work in an almost dry lubrication regime.

Such a description assigns a key role to the interface heating during the sliding and outlines the contribution of the interface roughness in the determination of the interface temperature. It is confirmed by exploring another relevant parameter affecting the interface temperature, namely the thermal conductivity of the slider.

Preliminary tests are performed with a pin made of hard phenolic resin. From the mechanical point of view, the resin is softer than steel (by a factor 10), but it is still much harder than ice (by a factor close to 15). The hypotheses on the contact mechanics of the system are still valid, in particular the dependence of the contact area on the softer material at the interface (the ice). From the thermal point of view, however, a conductor (steel has a thermal conductivity of about 20 W/mK) is replaced by an insulator (resin has a thermal conductivity of about 0.2 W/mK). The resin pin is prepared with a roughness R_a of 0.13 μm, close to the roughness of steel pin #1, and the measurements of the coefficient of friction are performed with the same experimental conditions used for the experiments with steel sliders. The values of the friction coefficient obtained at T=-2°C are reported in Figure 3.12, with the corresponding data from steel pin #1. Results from resin pin show decreasing values of the coefficient of friction as the sliding velocity increases, indicating a clear transition from dry to a mixed lubrication regime, thanks to the formation of a water layer in association with the higher interface temperature.

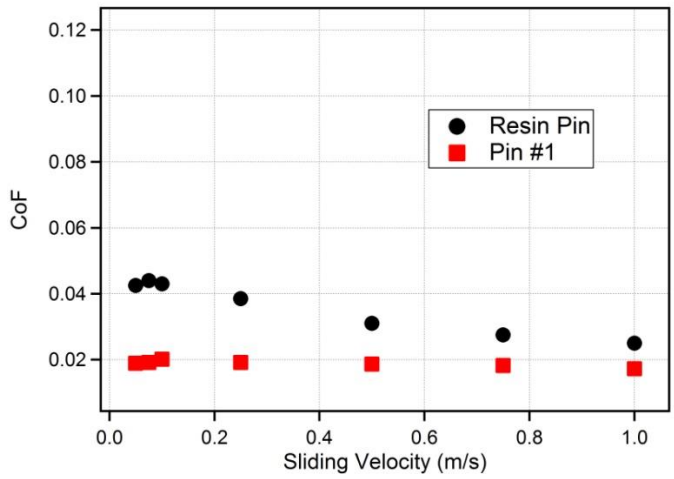

Figure 3.12 Comparison between the friction coefficient results obtained from the resin pin tests performed at -2°C (black dots) and the results from the steel pin #1 tests (red dots) performed at the same temperature.

Since the thermal conductivity of the resin is much lower than the one of steel, the conclusion is that the steel pin with the smoothest roughness works in boundary lubrication regime.

3.5. Conclusions

The two roughest pins clearly exhibited a mixed lubrication regime behaviour, so that the 1D-ALSFM modified for ice friction is able to replicate the experimental data and provides good approximations of the contact length a (in the range of tested velocities). Conversely, the smoothest pin shows a different behaviour that can not be fitted with the model in its current status of development. The trend of the coefficient of friction of the smoothest pin is clarified performing the same tests with a pin made of resin with the same surface roughness. Since this resin pin displays a mixed lubrication behaviour and the thermal conductivity of steel is bigger, the steel pin #1 is proved to work in the boundary lubrication regime. Therefore, the interplay between the surface roughness and the thermal conductivity of the counterpart of the ice surface determines the range of applicability of the proposed model.

Chapter 4

4. Friction of micro-patterned surfaces: experimental and numerical investigation

Recent experimental results about the frictional behaviour of sliding patterned surfaces have been obtained in the presence of non-trivial geometric features, e.g. microstructures like grooves, dimples, pillars or honeycomb patterns (Baum et al. 2014; Greiner et al. 2014; He et al. 2008; Li et al. 2016; Maegawa, Itoigawa, and Nakamura 2016; Murarash, Itovich, and Varenberg 2011; Tramsen et al. 2018). The goal of these studies is to explore the possibility of modifying the macroscopic friction properties by exploiting specific surface structures, both in dry and lubricated conditions, rather than through modification of the material chemistry.

Surface patterning has been studied for several years due to the possibilities it provides to accentuate the hydrophilic or hydrophobic properties of surfaces (Ghio et al. 2015; Hsu et al. 2014; Jung and Bhushan 2006; Pettersson and Jacobson 2004). Thus, it is of great interest to explore the effect of surface patterning on the frictional properties of surfaces, including those applications where control of water-repellent or adhesive behaviour is also required.

Friction between nominally flat surfaces at macroscale is the result of interactions at different length scales spanning from atomic forces to mesoscale and macroscale effects (Nosonovsky and Bhushan 2007; Vakis et al. 2018), as also pointed out in Chapter 2. In the case of micro-patterned surfaces, the characteristic lengths of the structures also play a role, so that it is difficult to separate the contributions of surface roughness, heterogeneity and patterning, and to identify the dominant mechanisms determining the emergent frictional behaviour. Thus, theoretical and numerical modelling must be associated to experimental results in

order to explain the effects induced by surface textures and to predict the most suitable configurations for specific purposes.

Models addressing the effect of surface patterning on macroscopic frictional behaviour have been developed for specific cases to be compared with some experiments (Filippov and Gorb 2013; Maegawa et al. 2016; Nguyen et al. 2013). Another option consists in developing a general simplified model, including the relevant features at the mesoscale and taking into account the microscale by means of effective laws (Vanossi et al. 2013) e.g. the Frenkel-Kontorova model (Braun and Kivshar 2004), describing the emergent superlubric transition due to incommensurate lattice lengths of two sliding layers (Mandelli et al. 2015; Norell, Fasolino, and De Wijn 2016). Another example is the so-called spring-block model, which has been implemented in 1D and 2D to investigate how friction properties can be modified by surface textures (Capozza and Pugno 2015; Costagliola et al. 2016; Costagliola, Bosia, and Pugno 2017; Costagliola et al. 2018). In particular, the model can provide useful insights on the transition between static and dynamic friction in the presence of structures that modify the surface stress distribution at the onset of sliding. Thanks to its simplicity, the model can qualitative describes the effects taking place, but due to the adopted approximations, its reliability for precise quantitative predictions is still to be evaluated. In (Costagliola et al. 2018) qualitative trends consistent with those obtained by experiments for surface structures were obtained, suggesting that some effects are quite general and may depend on parameters such as structure and dimensions of the surface textures rather than on specific material properties

In order to physically realize various surface patterns, several techniques have been developed and optimized in the past years, including laser surface texturing (Erdemir 2005; Etsion 2004, 2005, Gualtieri et al. 2009, 2011; Ranjan et al. 1991), which seems to provide high precision and speed of manufacturing , especially for applications with metallic surfaces. However, micromoulding techniques are a simple and effective alternative to the high costs of laser texturing (He et al. 2008;

Rand and Crosby 2009; Yu et al. 2012). These consist in casting an elastomer by using a mould formed by a lithographic technique, and thus transferring the pattern on the elastomer substrate.

In this Chapter, this method has been applied to realize microscale surface texturing in different shapes and sizes, including anisotropic patterns. Variable contact area fractions are considered to account for a wide range of potential applications. Friction tests are then performed on the patterned elastomer substrates against a flat polycarbonate surface and results are compared to the predictions of a 2D version of the Spring-Block model, (Costagliola et al. 2018) thanks to a collaboration with the University of Turin, evaluating for the first time the limits of its qualitative predictions towards a precise tribological design of the microscopic surface texture. In this Chapter, the ALSFM is not applied due to its limitations in the presence of discontinuities.

4.1. Bespoke setup for friction tests

Samples preparation

Surface samples are made of polydemethilsiloxane (PDMS) and are realized by direct copy of a patterned silicon substrate. This material is widely used in applications where a precise reproduction of a surface design is required (e.g. in microfluidics and in vitro biology applications). The PDMS (Sylgard184) is supplied as two different compounds: a cross-linking curing agent and a pre-polymer base. Polymerization begins when the two liquids are mixed together. Then, it is degassed a first time for 30 minutes directly after mixing and a second time 30 minutes after deposition on the silicon substrate. The Silicon substrate is processed in a Metal-Oxide-Semiconductor (MOS) pilot line, involving soft-lithography and dry etching to realize micrometric surface structures. Before PDMS moulding the silicon substrate is coated with a silane Self-Assembly Monolayer (SAM) both to avoid sticking and to promote detachment after curing.

Samples are cured at temperature of 70° C for 50 minutes and PDMS surfaces are peeled from the silicon substrate after cooling.

The chosen surface patterns are periodic arrangements of micro-holes illustrated in Figure 4.1. In particular, three patterns are considered, each of them characterized by different hole diameter Φ, pitch distance between holes p and corresponding contact Area Fraction $AF = (A_{th} - A_r)/A_{th}$ values, where A_{th} is the theoretical contact area while A_r is the real contact area of samples. Table 4.1 reports the geometrical characteristics of the samples, which have been chosen thanks to their simplicity of fabrication in potential applications.

An additional pattern is considered to study the influence of anisotropy (Figure 4.1 F, sample S). This pattern presents asymmetric holes 40 x 200 µm in size, with pitch distance 120 µm in the shorter direction. Again, this geometry is chosen for its simplicity, while providing marked anisotropy. The holes are staggered in the longer direction. Both principal directions (*x* and *y* reported in Figure 4.1 G) are considered in friction tests.

Sample	***Φ* (µm)**	***p* (µm)**	***AF***
Type A	5	20	0.95
Type B	10	15	0.65
Type C	15	20	0.56
Type S	40 200	120 200	0.67

Table 4.1 Geometrical characteristics of considered samples

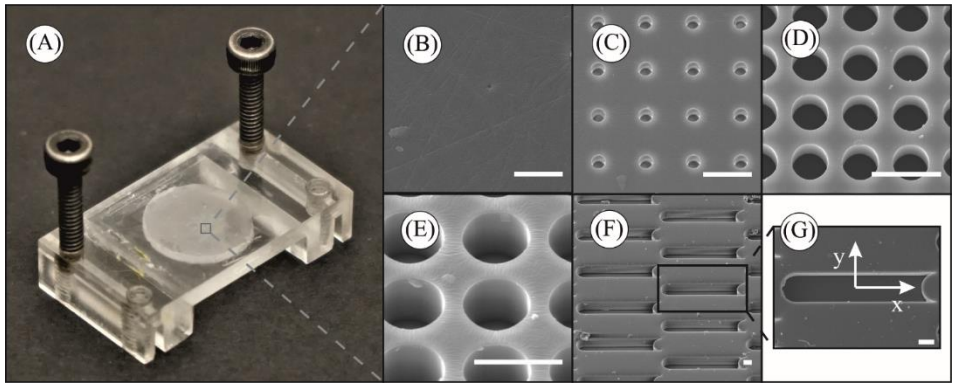

Figure 4.1 (A) Sample holder with a glued sample. (B) SEM image of a flat surface. (C) SEM image of sample A. (D) SEM image of sample B. (E) SEM image of sample C. (F) SEM image of sample S. (G) SEM image of sample S, enlargement of a single hole. These samples were tested along x and y directions. All scale bars are equal to 20 μm.

Setup for Tribological Tests

In order to obtain both the static and dynamic friction coefficients of the aforementioned surfaces, an *ad hoc* custom-built setup is used (Figure 4.2). It is composed of two main polycarbonate parts. The first component (Figure 4.2 A) is formed by a tensile machine and a lapped polycarbonate rigid surface, which is the reference surface where the samples can slide on. The other component is the sample holder and slider (enlargement in Figure 4.1 A). Samples are glued on the slider, with the surface to be tested in contact with the rigid polycarbonate base. The slider is pulled by a double inextensible wire, connected to the grip of the tensile machine. A weight of mass *m* is placed on the top of the slider to vary the normal applied force. The tensile machine records the wire pulling force transmitted by a frictionless roller, i.e. the friction force generated by the sample sliding on the polycarbonate base.

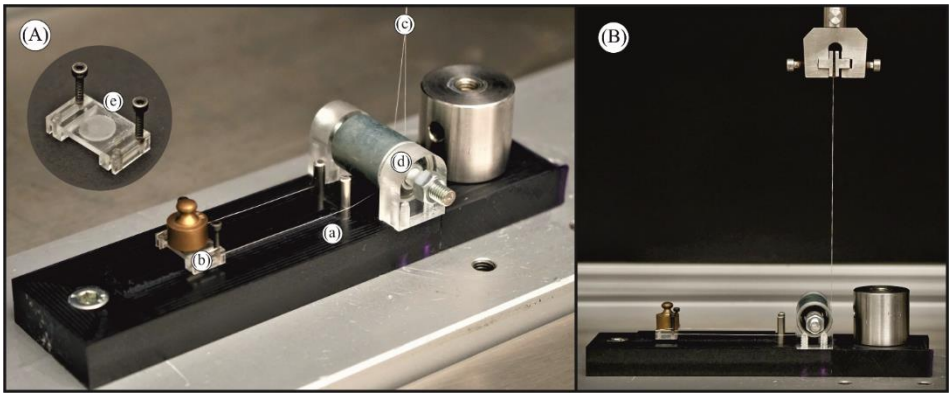

Figure 4.2 A) Details of the custom built setup. A black flat polycarbonate surface is fixed to a tensile machine (a). A transparent sample holder (b) can slide on the polycarbonate surface, thanks to two inextensible wires (c), which are connected to the grip of the tensile machine. A frictionless roller transmits the imposed velocity from the machine to the sample holder (d). Each PDMS surface is anchored to the transparent support (e) and loaded with different known weights. B) Overview of the setup.

Tribological Test Procedure

Samples are first glued to the sample holder. Both the surface to test and the polycarbonate base are cleaned with ethanol and dried, then a given mass is applied on the slider. The tests are then performed at constant puling speed of 0.2 mm/s, an average of values adopted in previous studies (Bistac and Galliano 2005; Galliano, Bistac, and Schultz 2003; Sahli et al. 2018). Once the detachment force is reached, at the static friction force value and corresponding to the first highest peak in the load-displacement curve, the sample starts moving at an approximately constant force value, that is the dynamic friction force. When this value stabilizes, the test is stopped. The dynamic friction force is considered as the mean value during the sliding phase.

Different masses are used during the friction tests, from 1.5 g (the mass of the sample holder without any additional mass) to about 140 g. Tests are repeated about ten times for each sample and mass (three samples per pattern type) to obtain sufficient statistics and all measurements are carried out at room temperature.

4.2. Experimental results

It is well known that frictional behaviour of elastomers is a complex phenomenon, usually governed by interfacial properties and dissipation mechanisms (Bistac and Galliano 2005; Carbone et al. 2009; Yu and Zhao 2009). Adhesion and friction are strictly correlated, and they both can depend on sliding velocity, applied normal load and molecular weight. The dependence on velocity of macroscopic friction is generally considered negligible (Bistac and Galliano 2005). In any case, in this study all friction tests are performed at the same sliding speed. On the contrary, the normal force affects the value of friction coefficients, with a decrease in the normal force leading to higher friction coefficients (Bistac and Galliano 2005; He et al. 2008).

Figure 4.3 shows the tangential force variation in time for different surface textures. As explained in the previous section, both the static and the dynamic friction forces can be determined from these friction tests. One friction test for each patterning type is reported, i.e. the friction force T normalized by the maximum friction force obtained in the same test (T_{max}), to highlight different behaviors between the samples. The tests illustrate considerable stick-slip behaviour between the polycarbonate and flat PDMS samples (Figure 4.3 A), especially at the beginning of sliding, but this effect becomes less evident with higher applied loads, as also reported in (He et al. 2008; Rand and Crosby 2009). The plots highlight some differences between patterns: in particular for sample C, static and dynamic friction forces are similar, with limited stick-slip effects.

In order to better point out the dependence of the friction force on the pattern type, Figure 4.4 shows the results for different applied pressures, both for static and dynamic friction. As found in previous works (Bistac and Galliano 2005; Galliano et al. 2003), macroscopic friction coefficients decrease non-linearly with increasing applied normal load.

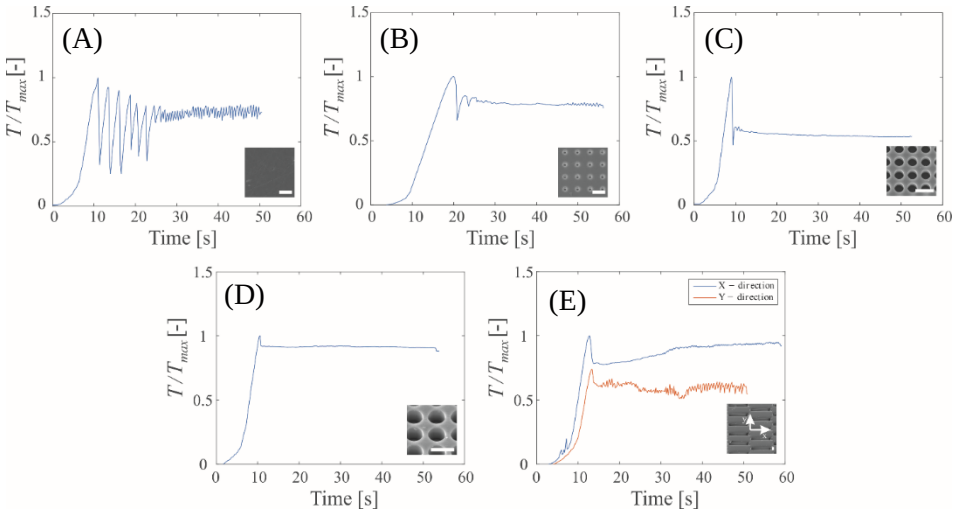

Figure 4.3 Examples of friction tests with the described setup; friction force (T) is normalized with respect to the peak value of the respective test, which corresponds to the static friction force (T_{max}): (A) Friction test for a flat PDMS surface . (B) Friction test for sample A. (C) Friction test for sample B. (D) Friction test for sample C. (E) Friction test for sample S, along x- and y- directions. All scale bars are equal to 20 μm.

For small or near-zero normal load, results present a large standard deviation, mainly due to difficulties in setting identical initial conditions for all the samples (samples were positioned on the setup by hand). Conversely, the standard deviation decreases for increasing normal load. This also applies to sample C, although some oscillations occur.

Results obtained for sample S highlight the effect of anisotropy. Friction along the *x* direction appears to be higher than friction along *y* direction. A similar result was found in (Rand and Crosby 2009), where they studied friction parallel and perpendicular to wrinkled surfaces.

From the experimental results, it can be deduced how surface patterns influence the frictional behaviour of the PDMS samples. Sample A is the one characterized by the smallest holes and larger spacing, thus its friction coefficients appear to be close to the flat samples.

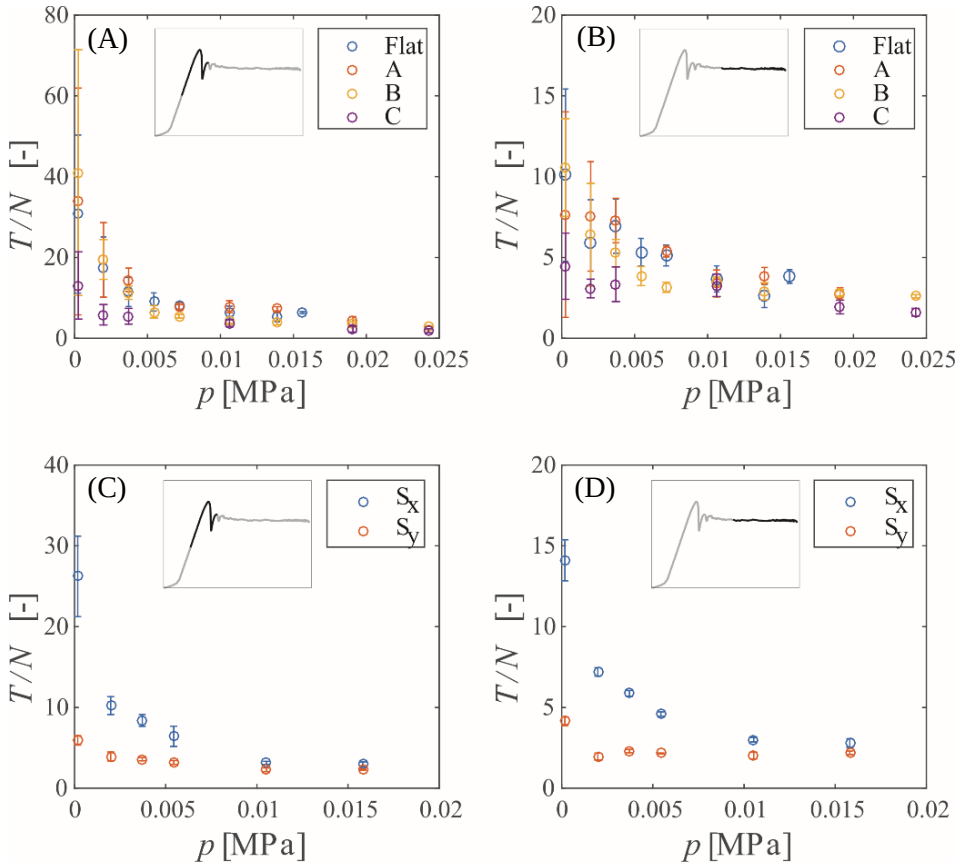

Figure 4.4 Experimental friction test results. Plots report the ratio between static and dynamic friction force (T) and the applied normal load (N) as a function of the normal pressure p (N/A_{th}). (A) Static friction coefficients of flat surfaces and samples A, B and C. (B) Dynamic friction coefficients of flat surfaces and samples A, B and C. (C) Static friction coefficients of samples S, along both x and y directions. (D) Static friction coefficients of samples S, along both x and y directions.

On the contrary, samples B and C have lower friction forces with respect to applied normal load.

This is partly due to a decrease in the real contact area of textured samples, as discussed in (He et al. 2008), but other aspects also contribute to this trend, including stress concentrations around surface features or the effect of adhesion,

which has a higher influence at lower loads, especially on the surfaces with higher texture density.

These results are described by the Coulomb's friction model, by fitting the experimental data with the equation:

$$\tau = \tau_0 + \mu p \tag{4.1}$$

Where p is the applied pressure, equal to N/A_{th}, while τ_0 and μ are the parameters to be fitted (red curves in Figure 4.5 and Figure 4.6).

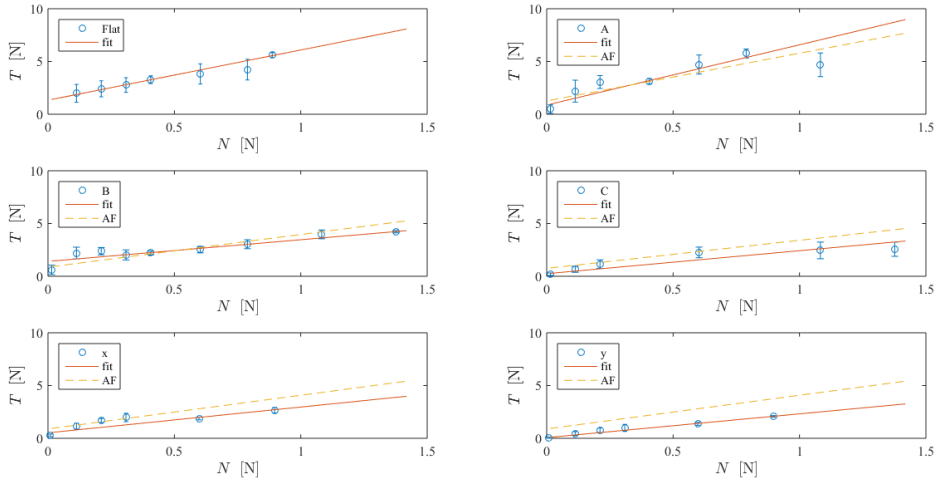

Figure 4.5 Static friction force T as a function of the applied normal load (N): experimental data (blue circles), linear fit (red line), rescaled fit (yellow dotted line). (A) Flat surface; (B) A sample;(C) B sample; (D) C sample; (E) S sample - sliding along the x direction; (F) S sample - sliding along the y direction.

Eq. (4.1) appears to be a good explanation of the frictional behavior, even if for small loads the coefficient of friction is higher, while increasing the load, it becomes constant, also because the effects of adhesion become smaller. The values obtained from the fits are reported in Table 4.2 Results obtained from the fits following Eq. (4.1).

In Figure 4.5 and Figure 4.6 another curve is reported (dotted lines), to study how patterns, so that the Area Fraction (AF), contribute in decreasing the coefficient of friction. This is done by computing the coefficient of friction of each patterned

surface with respect to its AF and the coefficient of friction of the flat surface. The equation of the yellow dotted curve is the following:

$$T = AF\left(\tau_{0,F} A_{th} + \mu_F N\right) \tag{4.2}$$

Where $\tau_{0,F}$ and μ_F are the adhesion force per unit area and the coefficient of friction of the flat surface, respectively. These predictions are qualitative good, but tend to overestimate the frictional behaviour of the patterned surfaces. Moreover, this formulation does not consider the effect of anisotropy, because sample S is characterized by the same AF. These insights suggest that the decrease in the friction coefficient due to a surface texturing depends not only from the real contact area of the samples. For these reasons, numerical simulations are realized, in order to describe more in details the effects of patterning and to capture also the surface anisotropy.

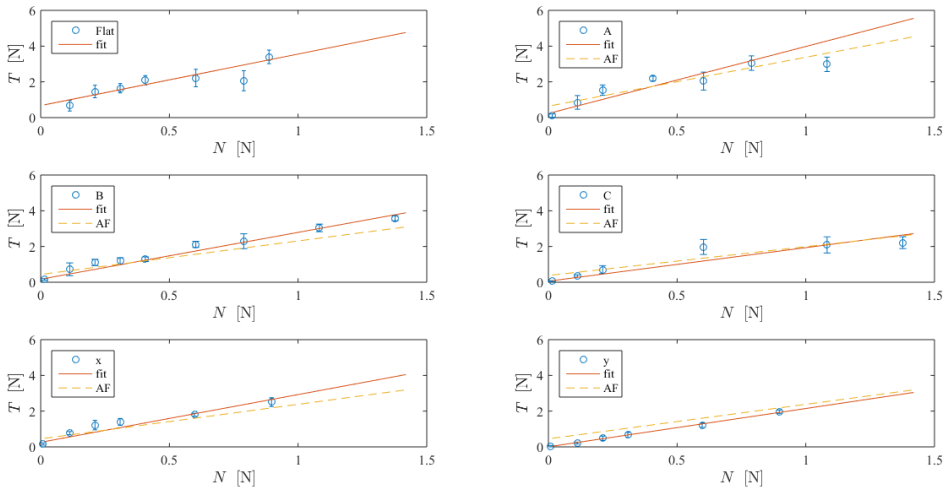

Figure 4.6 Dynamic friction force T as a function of the applied normal load (N): experimental data (blue circles), linear fit (red line), rescaled fit (yellow dotted line). (A) Flat surface; (B) A sample;(C) B sample; (D) C sample; (E) S sample - sliding along the x direction; (F) S sample - sliding along the y direction.

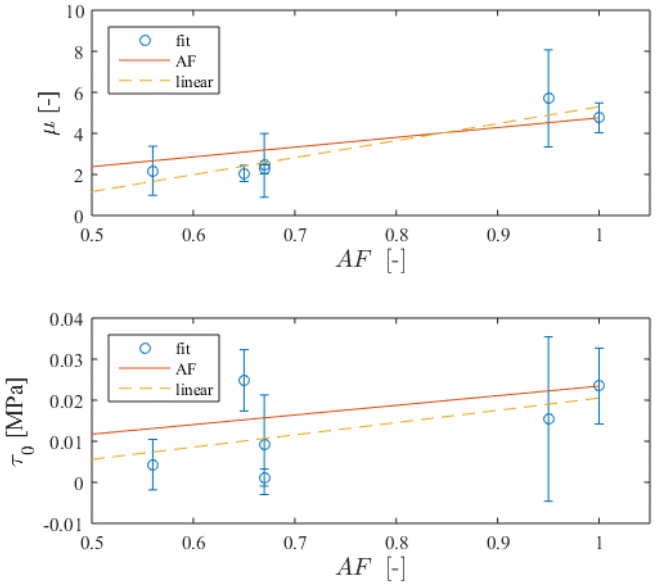

Figure 4.7 Comparison between the fitted parameters for the static coefficient of friction μ and τ0 with respect to the prediction by adopting Eq.(4.2). A linear fit of both the parameters show a decresing trend with decresing AF.

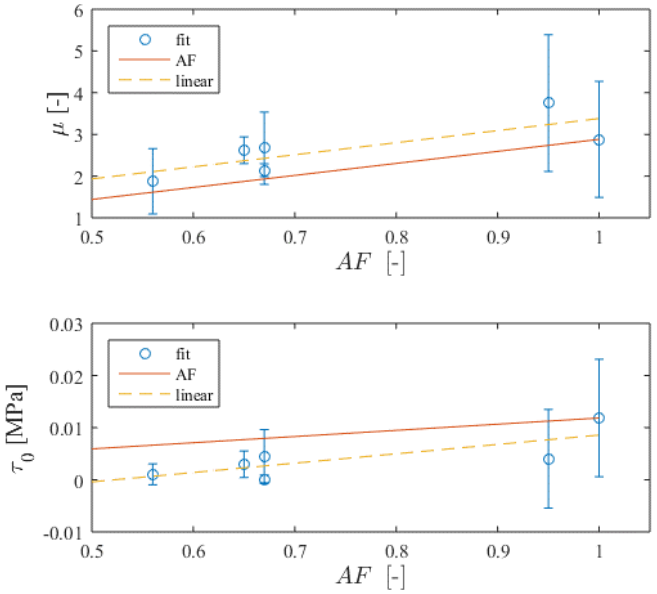

Figure 4.8 Comparison between the fitted parameters for the dynamic coefficient of friction μ and τ0 with respect to the prediction by adopting Eq.(4.2). A linear fit of both the parameters show a decresing trend with decresing AF.

Sample	STATIC				DYNAMIC			
	μ		τ_0 [kPa]		μ		τ_0 [kPa]	
	mean	st.dev	mean	st.dev	mean	st.dev	mean	st.dev
F	4.76	0.73	23.45	9.24	2.88	1.39	11.85	11.27
A	5.71	2.36	15.41	20.03	3.75	1.64	4.02	9.47
B	2.05	0.40	24.85	7.46	2.62	0.32	2.98	2.55
C	2.18	1.19	4.30	6.15	1.88	0.78	1.05	2.01
S (x)	2.44	1.55	9.17	12.13	2.67	0.87	4.52	5.12
S (y)	2.25	0.22	1.16	2.07	2.14	0.16	0.09	0.84

Table 4.2 Results obtained from the fits following Eq. (4.1).

4.3. Numerical simulations

Model formulation

In order to compare numerical results with experimental tests, a 2D formulation of the spring-block model previously introduced in (Costagliola et al. 2018) is adopted. In the spring-block model, the contact surface is discretized into elements of mass *m*, each connected by springs to the first eight neighbours and arranged in a regular square lattice with N_x blocks along the *x*-axis and N_y blocks along the *y*-axis. The distances between blocks on the two axes are l_x and l_y, respectively. The equivalence of this spring-mass system with a homogeneous elastic material is obtained by imposing that the stiffness of the springs parallel to the axis is $K_{int} = 3/8\ E\ l_z$, where l_z is the thickness of the layer. The stiffness of the diagonal springs is $K_{int}/2$, while the Poisson's ratio is fixed to 1/3 and $l_x = l_y = l$ (Absi and Prager 1975). The force exerted on the *i*–th block by the neighbouring *j*-th block can be written as: $\boldsymbol{F}_{int}^{(ij)} = k_{ij}\,(r_{ij} - l_{ij})(\boldsymbol{r}_{i} - \boldsymbol{r}_{j})/r_{ij}$, where $\boldsymbol{r}_i$, $\boldsymbol{r}_j$ are the position vectors of the two blocks, r_{ij} is the modulus of their distance, l_{ij} is the modulus of the rest distance and k_{ij} is the stiffness of the spring connecting them.

All the blocks are connected to the slider through springs of stiffness K_S, which are related to the shear modulus of the material $G = 3/8\ E$ and, by simple calculation, $K_s = K_{int}\,(l/\ l_z)^2$. For simplicity $l_z = l$. The slider moves at a constant velocity characterized by the vector $\boldsymbol{v}$ laying on the *xy* plane, so that the force

exerted by shear springs on the *i*-th block at time *t* is $\boldsymbol{F}_s^{(i)} = (\boldsymbol{v}t + \boldsymbol{r}_i^0 - \boldsymbol{r}_i)$, where $\boldsymbol{r}_i^0$ is the initial resting position. The total driving force is defined as $\boldsymbol{F}_{mot}^{(i)} = \boldsymbol{F}_s^{(i)} + \boldsymbol{F}_{int}^{(ij)}$. Each block is subjected to a normal force $F_n^{(i)} = pl^2$, where p is the applied pressure. Furthermore, a damping force term is added to avoid artificial block oscillations, $\boldsymbol{F}_d^{(i)} = - m \gamma \dot{r}_i$ where γ is the damping coefficient and $\dot{r}_i$ is the velocity vector of the block.

The interaction between blocks and the rigid plane is modelled as in (Costagliola et al. 2018) : each block is subjected to the fundamental Amontons-Coulomb (AC) friction force with a local static and dynamic friction coefficients, respectively $\mu_s^{(i)}$ and $\mu_d^{(i)}$, randomly assigned for each block at the beginning of the simulation from a Gaussian statistical distribution, i.e. $g(\mu_{s,d}^{(i)}) = (2\pi\sigma)^{-1} exp\,[-(\mu_{s,d}^{(i)} - (\mu_{s,d})_m)\,2/(2\sigma_{s,d}^2)]$. $(\mu_{s,d})_m$ denotes the mean value of the microscopic friction coefficients for static and dynamic case, respectively, and $\sigma_{s,d}$ is its standard deviation. Thus, the friction force on the *i*-th block can be described as follows: while the block is at rest, the friction force $\boldsymbol{F}_{fr}^{(i)}$ opposes to the total driving force, i.e. $\boldsymbol{F}_{fr}^{(i)} = -\boldsymbol{F}_{mot}^{(i)}$, up to a threshold value $F_{fr}^{(i)} = \mu_s^{(i)} F_n^{(i)}$. When this limit is exceeded, a constant dynamic friction force opposes the motion, i.e. $F_{fr}^{(i)} = - \mu_d^{(i)} F_n^{(i)}$. However, experimental data in this work show non-negligible adhesion effects in the friction force in the limit of zero pressure. In order to take into account this effect, a constant force is added to the static friction force thresholds. Thus, the friction threshold for the *i*-th block is $F_{fr}^{(i)} = \mu_s^{(i)} F_n^{(i)} + F_{ad}$, where the last term is the same for all blocks and includes all the possible adhesion effects. This is the simplest way to account for adhesion effects without adding specific details of the microscopic interactions that give rise to them. This level of approximation is consistent with that adopted for the AC friction force and with the rest of the model, which intentionally avoids a detailed microscopic description. In the case of patterned surfaces, areas corresponding to cavities are attributed friction coefficients equal to zero.

Thus, the motion of each block is described by a system of Newton's equations that can be solved using a fourth-order Runge-Kutta algorithm. From the motion equation of all blocks, the total friction force can be calculated through the total force exerted by the slider, e.g. $T_{tot}(t)=\Sigma_i \boldsymbol{F}_s^{(i)}(t)$, corresponding to that measured in the experiments. A typical behaviour of T_{tot} as a function of time is shown in Figure 4.9. From this, the static friction force $T=max_t\, T_{tot}(t)$ is the first maximum peak. To account for statistical effects, the simulations are iterated, by extracting each time new random local friction coefficients and determining a statistical average of any observable. The integration time step is 10^{-8} s, which is sufficient to reduce integration errors below the statistical uncertainty due to the model iterations as detailed in (Costagliola et al. 2018).

Model parameters

The numerical model contains a number of parameters that need to be modified to fit experimental data, although some degree of approximation is inevitable since experimental conditions cannot be replicated exactly. For example, the Poisson's ratio of the model is 1/3 by definition, while the PDMS real value is closer to 0.5.

The slider velocity, the applied pressure, the material density and Young's modulus are taken from experimental values. Thus, the mass of the block is $m = \rho l^3$, with ρ = 1.012 g/cm^3. The Young's modulus is assumed E = 0.8 MPa (Yu and Zhao 2009) , and the applied pressure varies between 3 KPa and 25 KPa. The slider velocity is in modulus v = 0.2 mm/s. The sliding direction with respect to the (x,y) orientation is randomly chosen at each simulation at an angle α, to account for the uncertainty in the sliding direction in experiments. Thus, the velocity vector of the slider is $v = (v\cos(\alpha), v\sin(\alpha))$. For flat and patterned samples A,B,C the angle is chosen with a uniform distribution in the range [0°, 45°]sufficient to emulate the experimental setup due to the symmetry of the samples. For anisotropic samples S, designed with a precise sliding direction ($\alpha = 0$ for S along x-axis samples and $\alpha = 90°$ for S along y-axis), the uncertainty

is reduced and the angle is chosen within a range [-10°, 10°] around the nominal sliding angle.

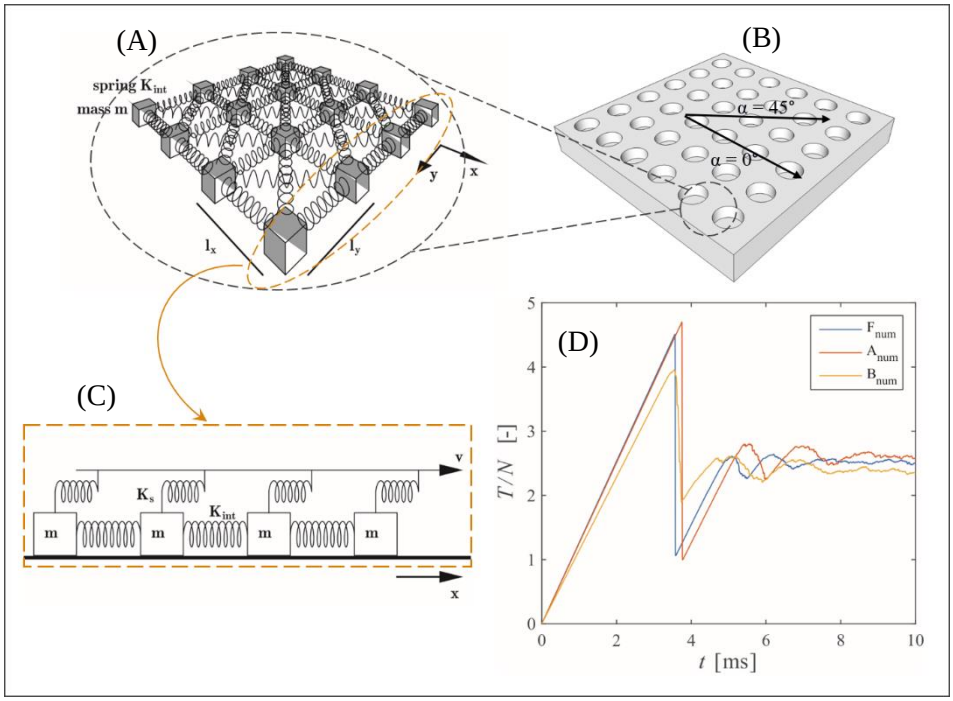

Figure 4.9 A) Sketch of patterned surface, where the main sliding direction is set to α=0°.B) Schematic of the 2D spring-block model with the notation used in the text. Mesh of the internal springs on the surface, the shear springs are not shown. C) Side view showing the slider moving at constant velocity v and the shear springs. D) Outputs of the numerical simulations, showing the evolution of the coefficient of friction in time.

The local friction coefficients of the model are obtained by fitting the experimental data for a flat, non-patterned surface. The optimal values are $(\mu_s)_m$ =4.5, σ_s =0.2 and $(\mu_d)_m$ =3.0, σ_d =0.2 for the local static and dynamic friction coefficient, respectively. The adhesion term is inferred by extrapolating the experimental results for each sample at zero applied normal pressure, as reported in the Table 4.3.

The spring mesh discretization length is fixed to l = 5 μm corresponding to the smallest feature of the experimental surface structures. The total number of blocks

required to match the size of the experimental sample would be very high, but not necessary. As shown in (Costagliola et al. 2018), the qualitative behaviour is not influenced by the number of blocks and the only effect is the decrease of the macroscopic static friction coefficients. Since there is already a set of free parameters, e.g. local friction coefficients and the adhesion, which need to be changed in order to match the macroscopic coefficients with the experimental one, it is equivalent to fix a smaller number of blocks and tune consequently the other parameters. Thus, the lateral number of blocks is $N_x = N_y = 85$, which allows to simulate all the different samples with the same mesh whilst adequately modelling the hole geometries.

However, the numerical model does not replicate the exact experimental sample geometry, since the adopted lattice is square, while the sample holes are circular in shape. The presence of holes is simulated by setting to zero the local friction coefficients of blocks in the corresponding positions, and their circular shape is approximated by means of squares with length equal to the diameter and spacing. The same local friction coefficients of the flat surfaces have been adopted for the regions of the patterned samples in contact with the substrate.

Sample	F_{ad}/l^2 **(kPa)**
Flat	23.8
A	36.1
B	44.4
C	34.4
S (*x* axis)	45.1
S (*y* axis)	11.2

Table 4.3 Adhesion terms expressed as force for unit surface deduced from experimental results for each sample.

In order to compare the numerical simulations with the experimental results, data must be normalized with the total normal force $N=\Sigma_i F_n^{(i)}$, so that the

comparison is performed through the quantity (T/N), i.e. the macroscopic friction coefficient, as a function of the pressure p.

4.4. Comparison between experimental results with numerical simulations

In this section, numerical results are compared to experimental results, in particular the behaviour of the static friction is considered for the analysed patterns. Once the model parameters are tuned through the simulations for a flat surface, results for patterned surfaces are in good agreement with experimental results, as shown in the Figure 4.10, in which the macroscopic static friction coefficient is reported as a function of the applied pressure p.

As suggested (Costagliola et al. 2018), despite the approximations, the model is able to capture the underlying mechanisms of the transition from the static to the dynamic phase in the presence of surface features, correctly accounting the stress concentrations occurring at the edge of these structures and the propagation of detachment fronts before the onset of sliding. This is confirmed by the current comparison, in which the modifications of static friction values due to surface patterning are correctly predicted. Thus, at least in this regime of slow sliding velocities and low to intermediate pressure values, the influence of the patterns is independent of material parameters such as exact elastic properties and microscopic interactions. These features can be taken into account by means of an effective local law, as done in the current model formulation, i.e. through the combination of Coulomb friction with constant adhesion force. The necessary tuning of model parameters can be performed once and for all for a given material system and these remain valid for varying surface patterns. Numerical simulations for asymmetrical or anisotropic patterns do not provide a perfect match with experimental data. This is probably mainly due to the implicit model assumption

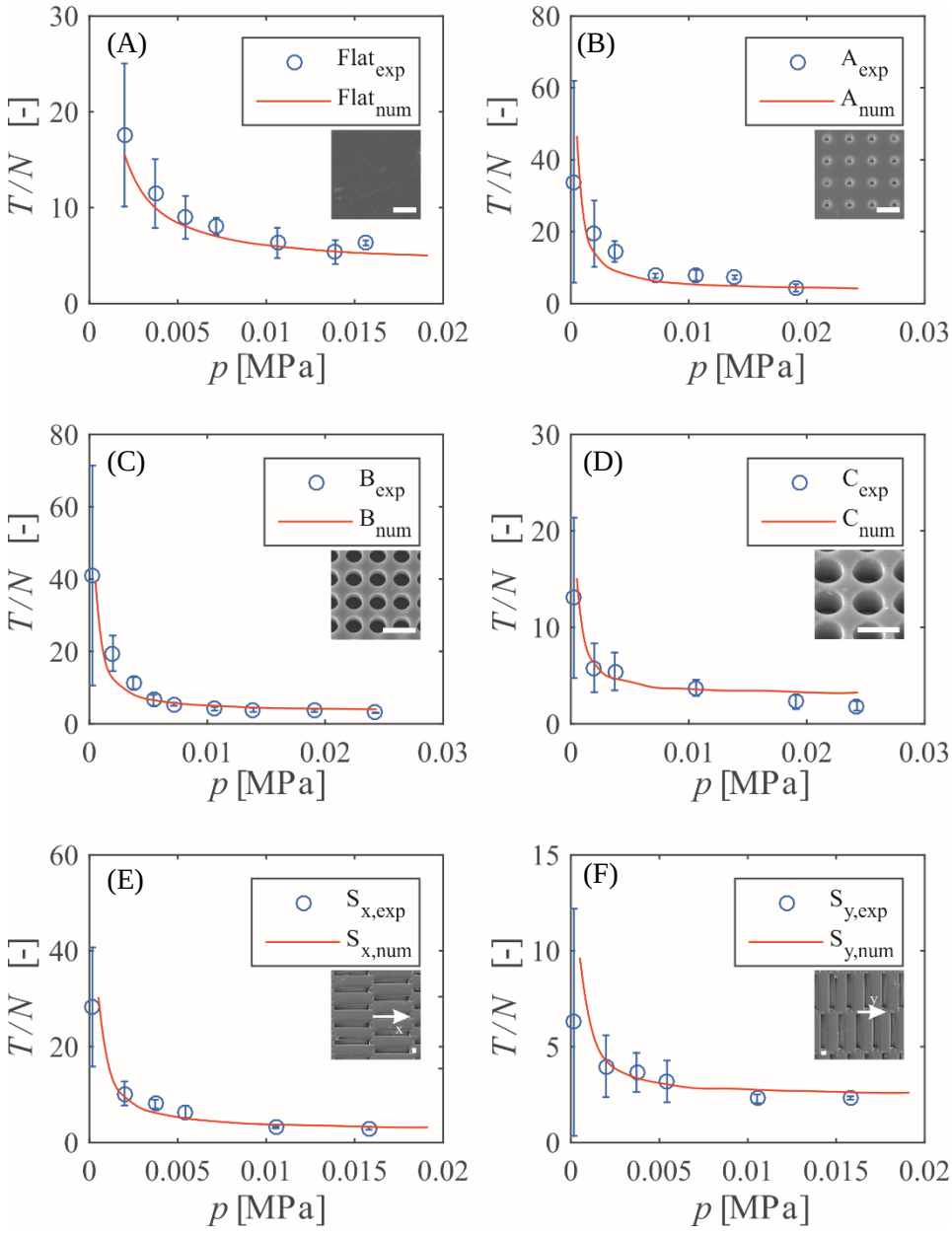

Figure 4.10 Numerical and experimental results of the static coefficient of friction. the ratio between the static friction force (T) and the applied normal load (N) as a function of the nominal pressure (p = N/A) is reported for all the case studies. (A) Flat surfaces; (B) A samples;(C) B samples; (D) C samples; (E) S samples - sliding along the x direction; (F) S samples - sliding along the y direction. All scale bars are equal to 20 μm.

that pattern shapes remain unvaried during sliding, which may not be strictly true for a soft elastic material like PDMS at higher pressure values. The current formulation does not include modifications of the contact shape or area of the patterns, so that the model is less predictive when these factors are influential. Despite this, the model correctly predicts an increase of static friction when the sliding direction is aligned with the longer sides of the structures, in the case of asymmetric holes.

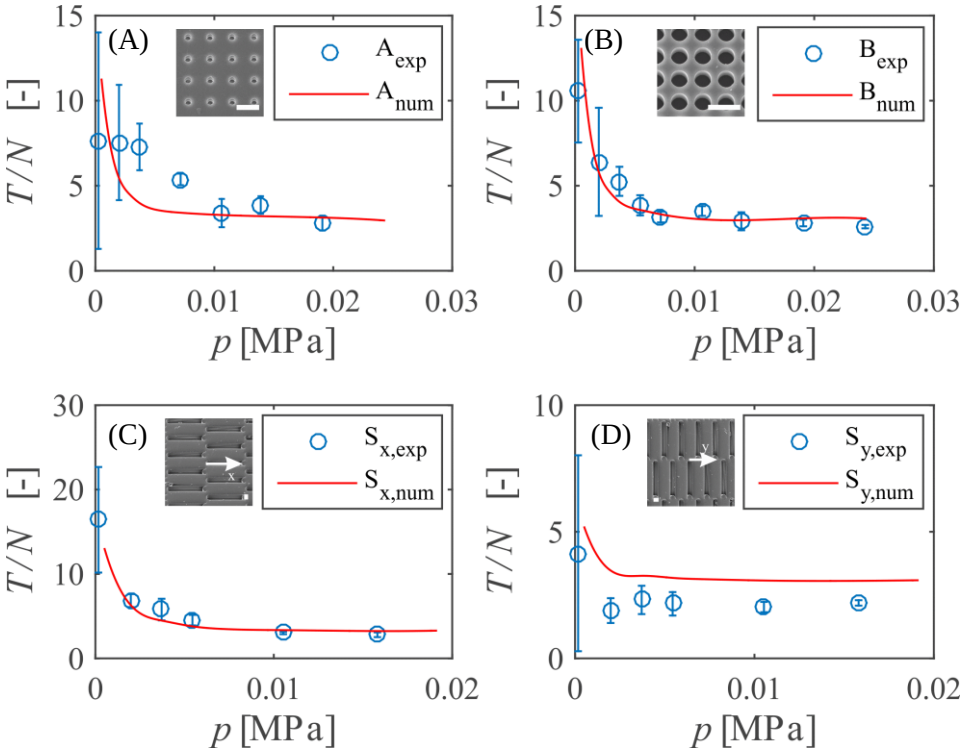

Figure 4.11 Numerical and experimental results of dynamic friction tests in term of the ratio between the static friction force (T) and the applied normal load (N) as a function of the nominal pressure (p = N/A) for all the case studies. (A) A samples;(B) B samples; (C) S samples - sliding along the x direction; (D) S samples - sliding along the y direction. All scale bars are equal to 20 µm.

The results for dynamic friction are also reported (Figure 4.11). As expected, the current formulation of the model is less accurate in describing this phase of the sliding, since it predicts similar asymptotic values for all the types of patterns,

while experimental results display larger variations. Also, there is a discrepancy for small normal pressures, suggesting that other phenomena become relevant in this case, e.g. the deformation of the surface structures.

In conclusion, the 2D spring-block model can be used not only for qualitative, but also for quantitative predictions of static friction of elastic patterned surfaces. The current formulation is reliable for the static phase in a regime of slow sliding and small-intermediate pressures, while additional modifications are required to correctly describe the dynamic phase or higher sliding velocities.

4.5. Conclusions

Experimental results are performed with a custom-made apparatus evaluating friction forces at a constant sliding velocity and for varying normal applied loads. Various types of simple micro-patterns are considered, from equally spaced circular holes to an array of elongated cavities, to evaluate the role pattern spacing and anisotropy. Results show good repeatability and consistency, with a decrease in macroscopic friction coefficients as a function applied normal load. Anisotropic patterns generate a variation of friction forces of up to 300% depending on the sliding direction in the plane, thus allowing to generate directionally tuned friction. Numerical predictions using a 2D spring-block model, modified to include adhesion, are considerably in compliance with experimental results, reproducing normal load dependence and static friction coefficient absolute values, both for isotropic and anisotropic patterns. Although some discrepancy remains, this study provides further evidence of the reliability of the presented model in the case of patterned 2D surfaces. This can be of great interest for the conception of novel surface texture designs for applications, which can enable control and tuning of their frictional, including adhesive properties.

Chapter 5

5. Friction in silk fibres to increase toughness without losing strength

Nowadays, global attention is increasingly focussed on the employment of biological, biocompatible and biodegradable materials in many disciplines, such as medicine, material and biomedical engineering, chemistry, applied science and technologies. Biomaterials can be used as common materials with many advantages: firstly, they are already available in nature, secondly, their mechanical properties are almost comparable to or even better than common materials, thirdly, they are recyclable and durable, but more importantly, they are suitable for being applied in medicine without human body rejection (Some examples are reported in Altman et al., 2003; Chen et al., 2014; Cheung et al., 2008; Hench, 1998; Hersel et al., 2003; Hubbell, 1995; Kundanati et al., 2016; Pugno & Carpinteri, 2007; Staiger et al., 2006; Warnecke et al., 2017; Zorlutuna et al., 2012)

One of these important materials, thoroughly studied in these last twenty-five years, is the *Bombyx mori* silkworm silk (Jiang et al., 2006; Omenetto & Kaplan, 2008, 2010; Pérez-Rigueiro, Viney, Llorca, & Elices, 2000; Viney, Llorca, Elices, & Pe, 1998). Silk has been defined as a new old material with a high capacity to impact high technology, material science, medicine and global health (Figure 5.1). It is composed of water and proteins (Jin and Kaplan 2003; Shao and Vollrath 2002), so that it appears as a transparent material, technologically quite simple to obtain (it is processed in water at room temperature). Moreover, it is biodegradable, edible and could be implantable in the human body without causing any immune response (Lawrence et al. 2009; Partlow et al. 2014; Zhang, Baughman, and Kaplan 2008).

Silkworm silk has been used for centuries in textile and medical industries, with recent application in composites (Ude, Ariffin, and Azhari 2013), tissue engineering scaffolds (Jin and Kaplan 2003; Meinel et al. 2009) and drug delivery (Hardy, Römer, and Scheibel 2008), in microelectronics and photonics (Keum et al. 2011; Kim et al. 2009, 2011; Lawrence et al. 2008; Mannoor et al. 2012). At the same time, the availability of materials displaying both high strength and high toughness is greatly desirable in structural applications. In the past, engineers had to reach a compromise preferring one or the other property depending on the requested application. Strong materials traditionally displayed poor deformation capability and, thus, low specific energy dissipation potential (Ritchie 2011). However, recent developments in materials science have led to new techniques taking inspiration from nature, which has already overcome the conflict between strength and toughness, providing materials like nacre and bones, with complex structures cooperating at different length scales (Bouville et al. 2014; Cranford et al. 2012; Munch et al. 2008). This concept has been transferred to engineering materials, introducing, for example, weak interfaces with intricate architectures (Mirkhalaf, Dastjerdi, and Barthelat 2014) or dispersing fibres in a brittle matrix to form a bridge complementing crack opening and fracture (Palmeri, Putz, and Brinson 2010). While all of these solutions require some chemical treatment on the material of interest, in the present study a different toughening strategy operating at a micro length scale is considered, with a significant increase in toughness of as-produced fibres. This follows an idea recently proposed in (Pugno 2014) and requires the introduction within a fibre of a sliding frictional element, e.g., a knot. When the opposite ends of a knotted fibre are pulled apart, a hidden length is revealed through a sliding mechanism, which dissipates a huge amount of energy. Basically, this mechanism reproduces at a microscopic level the breakage of weak bonds (i.e., sacrificial bonds) in highly coiled macromolecules, which allows the molecular backbone to be further stretched with beneficial effects on toughness (Fantner et al. 2006).

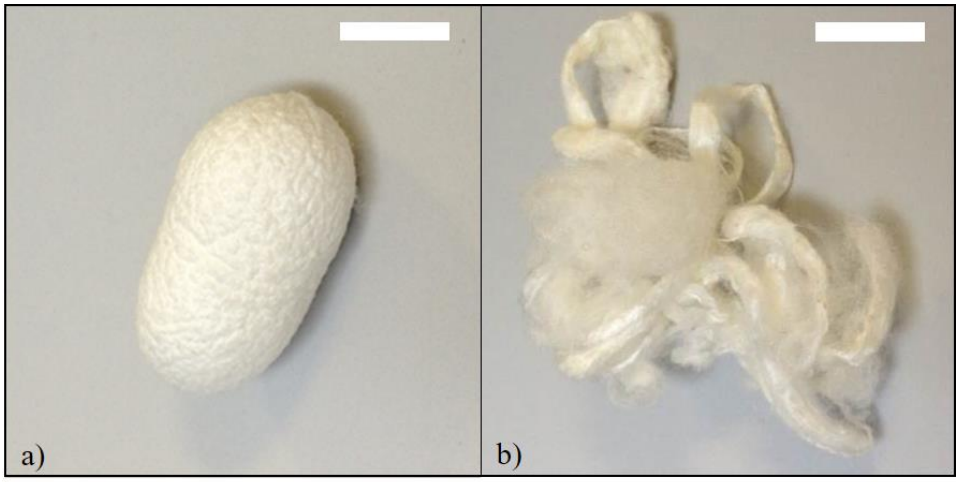

Figure 5.1 Our silkworm silk fibres were extracted from a) the cocoon as is, (the silkworm produces the cocoon to protect itself during the metamorphosis) or b) after the degumming process, where the sericin, a protein, is removed. Scale bars 1 cm.

Knots are intriguing topological elements, with a variety of examples appearing in fine arts as well as many scientific fields, including mathematics (Anstee, Przytycki, and Rolfsen 1989), polymer science (Bayer 1994; Saitta et al. 1999), colloids (Senyuk et al. 2013; Tkalec et al. 2011), fluids (Kleckner and Irvine 2013), chemistry (Ayme et al. 2012; Forgan, Sauvage, and Stoddart 2011), biology (Meluzzi, Smith, and Arya 2010), and obviously engineering (Pugno 2014). Knots can be introduced by hand (Arai et al. 1999), but many biological systems, like proteins and DNA, naturally form knotted configurations (Dean et al. 1985), and their function is still debated (He et al. 2014).

How the presence of knots can affect the mechanical properties of natural fibres as silkworm silk is investigated, and the topologies, that can maximize the toughness increase without compromising fibre strength are analysed. Firstly, the attention focuses on slip or running knots, which can be unfastened without inducing stress concentration and premature failure of the fibre. Then, other topologies are considered, involving different unfastening mechanisms and design complexities, some of them well known in the textile industry, with the aim of

providing new and feasible tools to optimize systems in which energy dissipation is highly requested.

5.1. Sample preparation

For the experiments presented in this chapter, single silk fibres are extracted from untreated and degummed cocoons of domestic *Bombyx mori* silkworm (see Figure 5.1). Some of the isolated fibres are manipulated by tweezers in order to introduce a knot, while others are left plain and used as control samples. From a structural point of view, natural silk fibres (baves) are composed of two filaments (known in the literature as brins), mainly consisting of fibroin, which are coated with a sericin layer binding them together. Since sericin does not contribute to load bearing capacity of the bave (Pérez-Rigueiro et al. 2001), it was removed through a typical degumming process (Bonani et al. 2011) in order to obtain separated bare fibroin fibres one from the other (Figure 5.2). The process of the present experiments follows a typical procedure (Bonani et al. 2011), consisting of boiling twice the cocoon with 1.1 g/L and 0.4 g/L Na_2CO_3 (anhydrous, minimum 99%, from Sigma Aldrich) water solution for one hour each time. This allows to remove any sericin traces and to produce bare fibroin fibres then washes with distilled water and air-dried.

Starting from a fibre length l of 20 mm and a distance between the fibre ends l_0 of 10 mm, the optimal single turned slip knot geometry, which maximized the fibre energy dissipation capability, has a very small knot diameter with a loop length l_p of about 10 mm. Indeed, as this kind of knot tends to loosen during tensile tests, it is convenient to start from the tightest possible configuration. On the contrary, it is not possible to perform successful experiments with a fibre length of 20 mm and l_0 equal to 10 mm, provided with double turned slip knot. Knots with this size could not completely unfasten during tensile tests. Thus, an optimization process is carried out to guarantee the knot the complete release during a test on a fibre with the longest possible loop (for dissipating the highest possible energy), still

keeping l_0=10 mm. This has the following geometry: knot diameter of 6±0.3 mm (with about 12 mm of fibre involved within the knot), and loop length (l_p) of 6 mm.

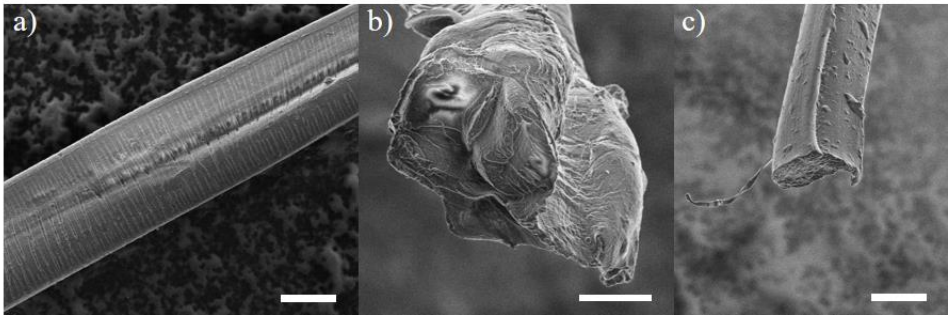

Figure 5.2 a) A natural fibre of silk formed by two brins coated and bended together by a layer of sericin, removed after the degumming process. b) Cross section of a natural silk fibre. c) Cross section of a degummed silk fibre. Scale bars 10 μm.

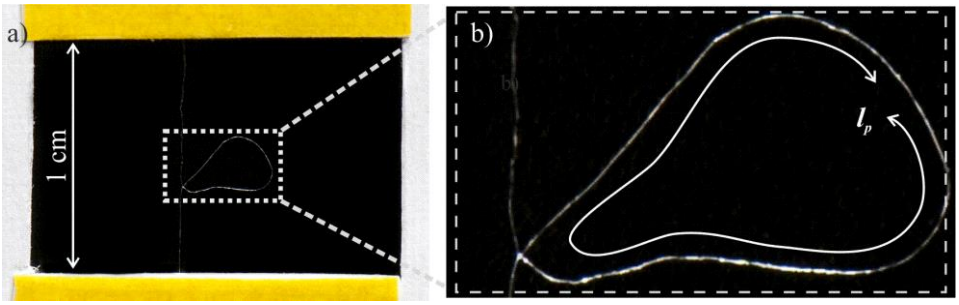

Figure 5.3 a) A degummed silk fibre, provided with an optimized knot, spanning over a paper frame prepared for nanotensile testing. The knot, either single (STSK) or double (DTSK) turned slip knot, is characterized by two main parameters, the loop length, l_p, and the knot diameter, as shown in the zoomed view (b).

5.2. Mechanical properties of silk fibres

From a mechanical point of view, silk fibres extracted from silkworm cocoons are reported with remarkable mechanical properties, i.e., Young modulus up to 16 GPa (Pérez-Rigueiro et al. 2000), fracture strength up to 600 MPa (Viney et al. 1998) and toughness of $6 \cdot 10^4$ J/kg (Shao and Vollrath 2002), even though these

cannot compete with those characterizing spider silk dragline (Pugno, Cranford, and Buehler 2013), having fracture strength of 1.3 GPa and toughness of $16 \cdot 10^4$ J/kg (Shao and Vollrath 2002). However, since spiders offer a smaller yield capability, which hinders their silk to be fully implemented in a massive industrial production (Altman et al. 2003), it would be desirable to combine the advantages offered by both such biomaterials, thus developing methods to provide silkworm silk with spider silk performances.

However, extracting meaningful data from tensile tests on silk is not a straightforward process. As expected from literature, the stress-strain curves of control silk fibres display significant variability (Figure 5.4), which causes in turn variability in terms of mechanical properties, included toughness.

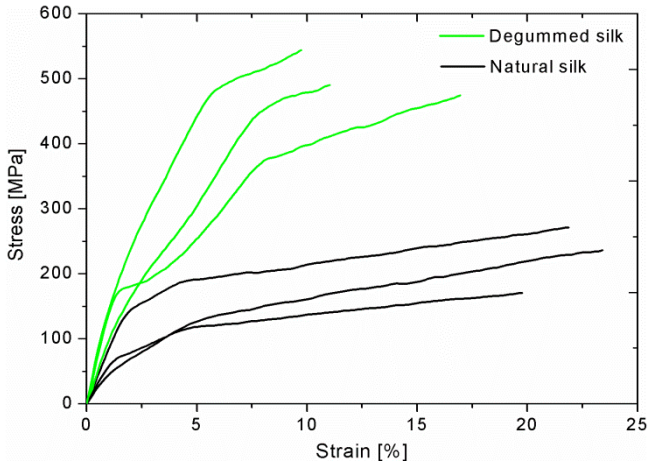

Figure 5.4 Stress-strain curves derived from tensile tests carried out on single untreated baves (black line) and degummed fibres (green line), both showing significant variability.

Such variability is mainly caused by fluctuations in the fibre diameter, which is in turn dependent on many factors closely related to the silkworm nature (Zhao, Feng, and Shi 2007), such as mode and speed of the spinning process. Furthermore, fibre diameter can not only vary in size, but also in shape over the same cocoon (Colomban and Dinh 2012; Pérez-Rigueiro et al. 2000; Viney et al. 1998).

However, as common practice in literature (Pérez-Rigueiro et al. 2000), fibres are considered as provided with a circular cross-section.

The diameter of each tested fibre is evaluated from observation under either optical or scanning electron (SEM) microscope, providing average values of 21 µm and 12 µm for natural and degummed fibres, respectively.

For a fibre without any knot, the energy dissipated per unit mass, T_u, e.g., toughness modulus, can be computed from its stress-strain curve as (Figure 5.6 a):

$$T_u = 1/m \int_0^{x_f} F dx = Al/m \int_0^{\varepsilon_f} \sigma d\varepsilon = 1/\rho \int_0^{\varepsilon_f} \sigma d\varepsilon \qquad (5.1)$$

Where m is the fibre mass, x_f is the displacement at fracture, F is the applied force, A is the fibre cross sectional area, l is the fibre initial length, ρ is the volumetric density, $\varepsilon_f = (l_f - l)/l = x_f/l$ is the fracture strain, l_f is the fibre final length, and $\int_0^{\varepsilon_f} \sigma d\varepsilon$ is the area under the stress-strain curve.

Both untreated baves and degummed single silk fibres are tested at room temperature through a nanotensile testing machine (Agilent T150 UTM) and at a strain rate of 0.001 s^{-1} in case of control samples and 0.002 s^{-1} in case of samples provided with knots. Figure 5.4 shows some tensile tests results of both natural and degummed silk.

Reference values of silk toughness are derived from tensile testing of control untreated baves and degummed single silk fibres with no knot implemented (i.e., toughness is proportional to the area under sample stress-strain curve)

5.3. Knot implementation is silk fibres

In order to evaluate the toughness increase due to the knot introduction, more than 150 single fibres are tested of both untreated and degummed silk, provided with optimized knot topologies (see at the end of this Chapter for details of experimental data).

The knots introduced in the fibres are designed to unfasten as their opposite ends are pulled apart.

This is a necessary condition to fully exploit the knot friction potential and avoid any stress concentration, which can trigger premature failure of the fibre, and compromise its load bearing capacity.

Furthermore, since raw silk from cocoons usually undergoes a degumming process before being processed in industrial applications, in the first knot optimization both natural (i.e., extracted directly from a cocoon) and degummed (i.e., extracted from degummed cocoons) fibres are considered, in order to capture potential differences. Then, tensile tests are performed on both knotted and unknotted control samples in order to evaluate the toughness enhancement due to the knot presence.

Firstly two different knot topologies are tested, involving opposite unfastening mechanism. These knots are known as *Noose* and *Overhand Loop* (Ashley 1944), as reported in Figure 5.5 (a) and (b). While the *Noose* requires the fibre to be turned once around itself, the *Overhand Loop* requires the fibre to be first folded and then turned around itself, thus involving a different unfastening mechanism. In the first case the knot tends to untie as the fibre ends are pulled apart. Thus, at the beginning, this can be very tight and cause the fibre to be highly stressed during the whole tensile test and its toughness to be significantly increased. On the contrary, in the *Overhand Loop* the knot tends to further tie, requiring to start from a very loose configuration in order to be completely released, with much less toughness enhancement.

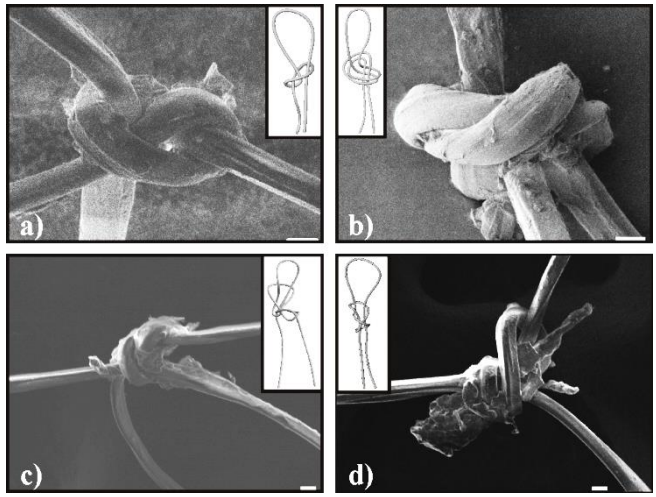

Figure 5.5 Gallery of knots implemented in single silk fibres. (a) SEM picture of the Noose with a schematic on top. (b) SEM picture of the Overhand Loop with a schematic on top. (c) SEM picture of the Chain Knot with two chains and a schematic on top. (d) SEM picture of the X-Knot with a schematic on top. Scale bar: 10 µm.

Then, other slip knot topologies are investigated and optimized, which are strictly related to the *Noose* in order to explore the possibility to further improve its performance.

The first topology is an open version of the *Monkey Chain Lanyard Knot* (Ashley 1944), well known in the textile industry as this reproduces a chain stitch of crochet (Figure 5.5 c): after a noose is tightened, one thread of the fibre is folded and forced to cross the loop, which ends in a chain of a chain stitch. In some samples, such steps are repeated in order to build chain stitch with four and six chains, respectively. In the following, for the sake of brevity, such knot topology will be referred to as simply *Chain Knot*.

The second topology (Figure 5.5d), which has no common name, requires first to implement a noose (Ashley 1944) then to turn its loop inside the knot, obtaining an x-shaped knot, which is, for this reason, referred to as *X-Knot* topology in the following (see Figure 5.7 for details about the knot implementation).

5.4. Estimation of toughness increase due to knots

If a knot is introduced in a fibre, (Figure 5.5) the expression to compute the toughness modulus has to be modified in order to take into account the fibre length involved in both the knot (negligible) and the loop, with its toughness modulus, T_k, which can be computed as:

$$T_k = 1/m \int_0^{x_f^*} F dx = A l_0/m \int_0^{\varepsilon_f^*} \sigma d\varepsilon = (1 - k_1)/\rho \int_0^{\varepsilon_f^*} \sigma d\varepsilon \qquad (5.2)$$

where $x_f^* = l - l_0 + x_f$, l_0 is the initial length equal to the distance between the fibre opposite ends, $\varepsilon_f^* = x_f^*/l_0$, $k_1 = (l - l_0)/l$ accounting for the difference between l_0 and l and $\int_0^{\varepsilon_f^*} \sigma d\varepsilon$ is the area under the stress-strain curve of the knotted fibre (Pugno 2014).

In order to infer quantitative results of knot induced toughness increase, which is not affected by the variability of silk mechanical properties, the toughness of a knotted sample is compared with the toughness of a control sample. If possible, toughness comparison refers to the same fibre.

When the opposite ends of a knotted fibre are pulled apart, the knot presence causes alternating cycles of loading (the knot is tightened and the fibre is stressed) and unloading (the knot unties, some fibre length is released from the loop, causing stress relaxation) until the knot loosens completely (Figure 5.6 b). In all the tests, the final part of the stress-strain curve of knotted fibres reproduced the stress-strain curve of the corresponding unknotted fibres, showing, in fact, a stress at break comparable with the strength of reference samples (without any knots and extracted from a cocoon region adjacent to the knotted fibre) tested apart (Figure 5.6). Moreover, since it is well known that silk mechanical properties display significant variability (Zhao et al. 2007), it is preferable to compare the toughness of a knotted fibre with the toughness of the same fibre in unknotted configuration.

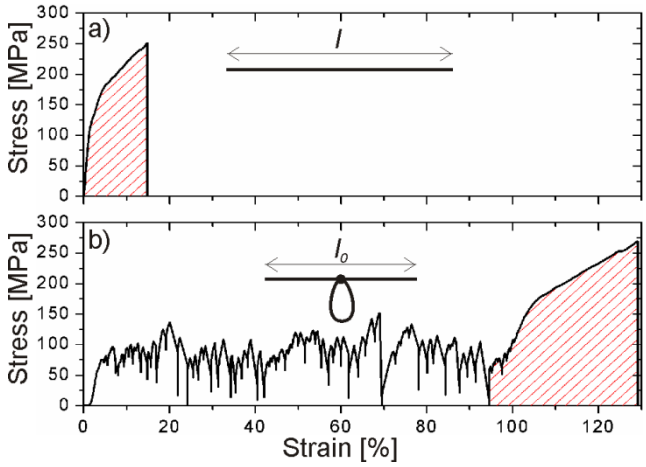

Figure 5.6 (a) Stress-strain curve of an unknotted natural fibre with length l. (b) Stress-strain curve of a knotted natural fibre with length l and distance between its opposite ends l_0, which was extracted from a cocoon region adjacent to the unknotted fibre (a). The presence of the knot modifies the shape of the stress-strain curve (a), introducing a plastic-like plateau and leaving a final region (highlighted) almost corresponding to the stress-strain curve of the same fibre with unknotted configuration. The strain interval within this final region appears larger than in (a) since it is computed with respect to l_0 instead of l.

Accordingly, the final part of the stress-strain curve of a knotted fibre is considered as the curve of its reference unknotted fibre. Then, the ratio between the toughness of the knotted fibre, T_k, and the toughness of the corresponding unknotted fibre, T_u', can be obtained with the following expression:

$$T_k/T_u' = \left[Al_0/m \int_0^{\varepsilon_f^*} \sigma d\varepsilon\right] \Big/ \left[Al_0/m \int_{\varepsilon^*}^{\varepsilon_f^*} \sigma d\varepsilon\right] = \int_0^{\varepsilon_f^*} \sigma d\varepsilon \Big/ \int_{\varepsilon^*}^{\varepsilon_f^*} \sigma d\varepsilon \qquad (5.3)$$

where $\int_{\varepsilon^*}^{\varepsilon_f^*} \sigma d\varepsilon$ is the area under the final part of the stress-strain curve, when the knot is completely released.

However, sometimes it is not possible to consider the same fibre for comparison, since the final part of the stress-strain curve does not clearly show the behaviour of the fibre in unknotted configuration. Therefore, the toughness increase is estimated by referring to the toughness modulus of an unknotted fibre extracted from a cocoon region adjacent to that of the knotted fibre in order to limit

variations in physical and mechanical properties. In this way, the area under the stress-strain curve of the knotted fibre has to be scaled by the factor (1-k_1):

$$T_k/T_u = \left[(1-k_1)/\rho \int_0^{\varepsilon_f^*} \sigma d\varepsilon\right] \Big/ \left[1/\rho \int_0^{\varepsilon_f} \sigma d\varepsilon\right] = (1-k_1) \int_0^{\varepsilon_f^*} \sigma d\varepsilon \Big/ \int_0^{\varepsilon_f} \sigma d\varepsilon \quad (5.4)$$

5.5. Results

In the present section, the effectiveness of four kinds of slip (or running) knots are analysed and compared.

Referring to the *Noose* and the *Overhand Loop*, implemented in both natural and degummed silk, the fibre is allowed in any case, to slide throughout the knot in order to promote energy dissipation, but undergoes a different unfastening mechanism (Figure 5.7).

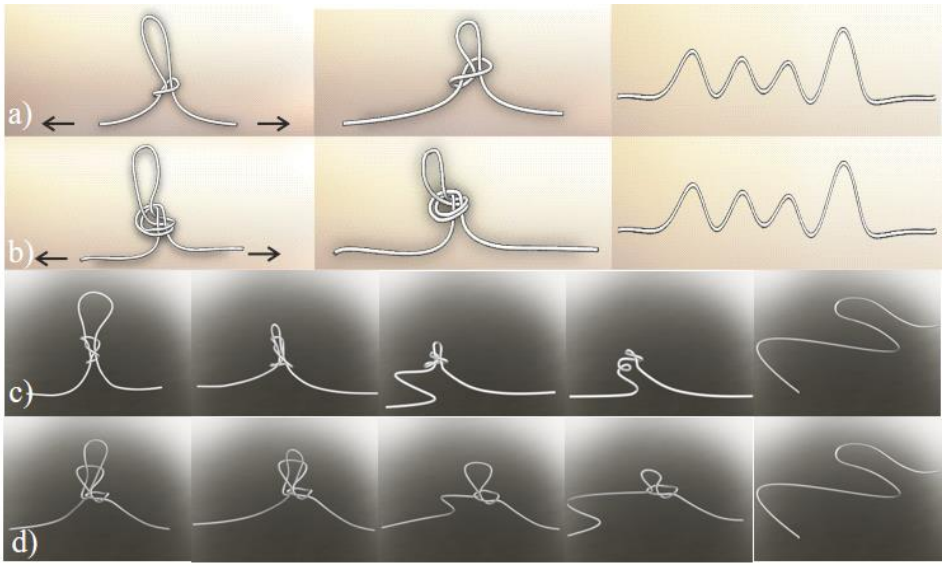

Figure 5.7 Untightening mechanism of the (a) Noose, (b) Overhand Loop, (c) Chain Knot (in this schematic with two chains) and (d) X-Knot. When the fibre opposite ends are pulled apart, the loop is sucked into its closest chain until this is completely released, thus forcing the knot to collapse into a simple noose. If the fibre ends are pulled further apart, the noose loosens until the knot is completely untightened. On the contrary, the Overhand Loop becomes tighter as the fibre is pulled. In an X-knot, the fibre appears to be turned twice at the bottom of its loop. When its opposite ends are pulled apart, the turn closer to the loop tends to tie, causing friction against the fibre sliding,

while the other one loosens. In this way, the knot can unfasten completely although a significant amount of energy can be dissipated.

In fact, while the *Noose* is always able to unfasten, even when extremely tight, as it loosens when the fibre ends are pulled apart, the *Overhand Loop* poses much more issues, since, on the contrary, it becomes tighter as the fibre is pulled. For both untreated and degummed silk, either knot topology is optimized in order to fulfil two main requirements.

	Knot topology	Friction stress / strenght	Raw silk	Degummed silk
Diameter [μm]	-	-	21 ± 2	12 ± 2
Strength (unknotted fibres) [MPa]	-	-	219 ± 68	481 ± 91
T_u [J/g]	-	-	20 ± 11	29 ± 13
Strength [MPa]	*Noose*	> 8%	229 ± 50	343 ± 104
		< 8%	216 ± 46	463 ± 120
	O. L.	> 8%	-	-
		< 8%	237 ± 53	434 ± 146
T_k [J/g]	*Noose*	> 8%	45 ± 12	28 ± 9
		< 8%	19 ± 8	36 ± 18
	O. L.	> 8%	-	-
		< 8%	17 ± 18	29 ± 17
T_u ' [J/g]	*Noose*	> 8%	15 ± 9	29 ± 17
		< 8%	16 ± 7	29 ± 17
	O. L.	> 8%	-	-
		< 8%	16 ± 8	27 ± 17

Table 5.1 Strength and toughness modulus (T_u) of unknotted control fibres. Strength, toughness modulus (T_k) and toughness modulus after unfastening (T_u') of fibres with the Noose and the

Overhand Loop (O. L.) (the toughness modulus was computed considering a density of 1.4 g/cm3 (Pérez-Rigueiro et al. 2001)*). For each knot topology, two sets of data are provided, corresponding to samples with average stress in the strain interval 0%-40% of their strain at break (i.e., friction stress) above or below the 8% of their strength. Such threshold value was considered as the minimum friction stress required for knots to be efficiently implemented.*

With respect to unknotted control samples (Figure 5.4), many differences arise. First, as expected, the knot presence extends the strain interval (i.e., fibres provided with a knot reach a bigger apparent strain) and introduces an artificial plateau, characterized by a series of peaks and drops, corresponding to partial fastening and unfastening of the fibre in the knot and related stick-slips.

In particular, a well-defined plastic-like plateau appears especially when the single turned slip knot topology is considered and this is more evident for natural fibres than for degummed fibres. This means that natural fibres with this knot topology can be constantly high stressed throughout the whole test, causing energy dissipation to be strongly enhanced. Such observations are quantitatively confirmed by values reported in Table 5.1. The single turned slip knot topology allows to significantly enhance toughness of both natural and degummed fibres, with almost 300% increase in the optimal configuration. Conversely, the *Overhand Loop* resulted to be sensibly less performing, with comparable toughness increase around 110% in both natural and degummed fibres.

Knot Topology	Toughness Increase (%)	Strength Decrease (%)
X-Knot	450 ± 107	18 ± 27
Chain Knot (2 chains)	310 ± 11	7 ± 35
Chain Knot (4 chains)	150 ± 11	19 ± 27
Chain Knot (6 chains)	142 ± 18	11 ± 30

Table 5.2 Comparison (*) between the toughness increases and strength decreases provided by different knot topologies with respect to unknotted single silk fibres (average strength of 514 ± 103 MPa and average toughness modulus: 32 ± 14 J/g computed considering a density of 1.4 g/cm^3 [32]).

(*) Because of the variability in the knot tightening procedure, the knot size shows some difference from sample to sample. Thus, when we computed the toughness enhancement provided by each knot topology, we considered an average over three results representative of their optimized behaviour.

Through the analysis of the knot evolutions of the *Noose* only for degummed silk fibres (Figure 5.5 c and d), it is interesting to observe that at the end of the test, before the knot loosens completely and the curve collapses into the stress-strain curve of an unknotted fibre, there are some pronounced stress peaks, which correspond to the number of times the fibre has been turned around itself during preparation. The number of final stress peaks, mainly responsible for toughness increase, is more visible in case of a chain knot with four and six chains.

The *Chain Knot* and the *X-Knot* can be firmly tightened and then completely unfastened during the test with quite high energy dissipation (Table 5.2), depending on the stress plateau value introduced in the corresponding stress-strain curve (Figure 5.8 b). In particular, samples with a chain knot with two chains display a stress-strain curve with a well-defined plastic-like plateau between one eighth and a quarter of the fracture strength (Figure 5.8 b), providing a toughness increase of about 300%, which is comparable to the result obtained with the *Noose* (Pantano et al. 2016). When the number of chains is increased, there is no visible trend in toughness enhancement (Table 5.2). In fact, even if some samples with a chain knot with four chains provide some significant toughness enhancement of almost 400%, the average value is much lower, being about 150%, which is comparable to the average result provided by chain knots with six chains. However, such values are still bigger than the one recorded for the *Overhand Loop* (Table 5.2).

On the contrary, *X-Knot* topology, with a higher plateau in sample stress-strain curve and average values of about one fifth of the fracture stress (Figure 5.8 b) results in a toughness enhancement up to 450% on average (Table 5.2).

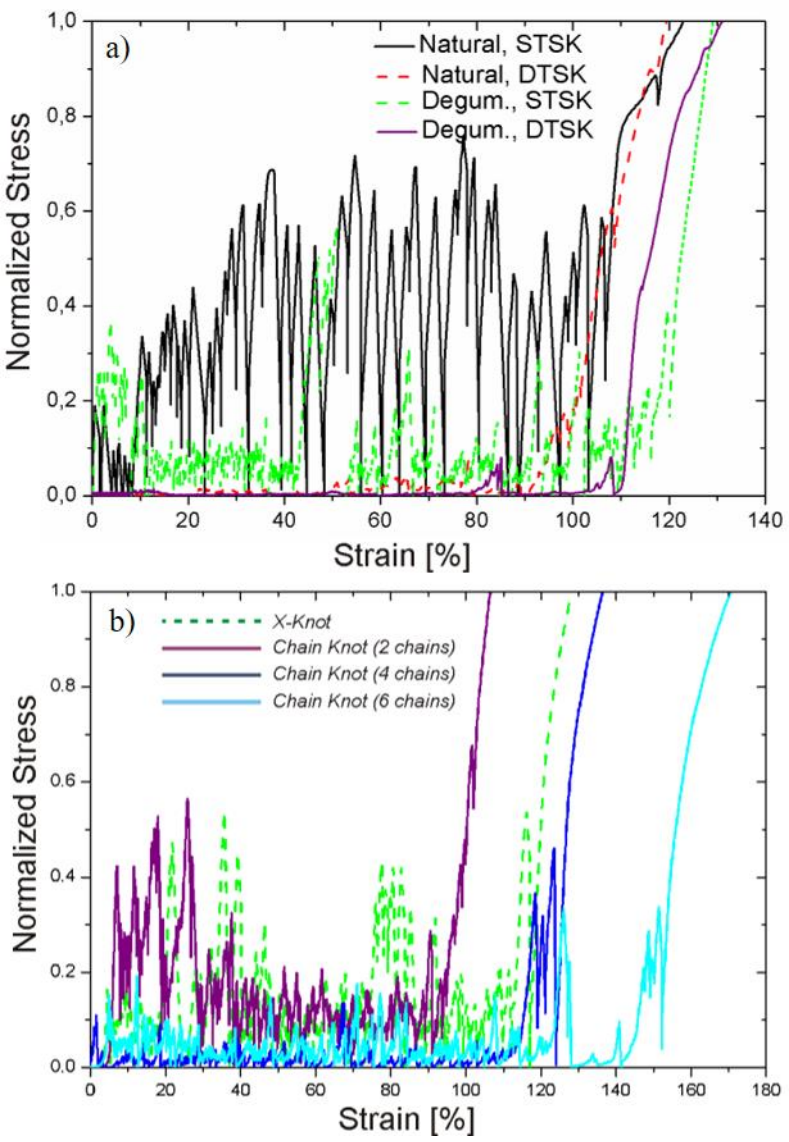

Figure 5.8 (a) Stress-strain curves of natural and degummed silk fibres with optimized Noose or Overhand Loop slip knots. Comparison between the normalized stress-strain curves obtained for natural and degummed single silk fibres provided with optimized knots. Stress values are normalized with respect to fracture strength. Comparison between the stress-strain curves derived from samples with an X-Knot and a Chain Knot with either 2, 4 or 6 chains, respectively. Here, stress values are normalized with respect to the fracture stress of each fiber.

5.6. Discussion and conclusions

The results presented in the previous section can be explained by focusing on the unfastening mechanism involved in either knot topology. In fact, the *Noose* tends to loosen during the test (Figure 5.7 a). Thus, it is possible to start from a very tight configuration, which provides the fibre to be significantly stressed throughout the whole test within a relatively wide apparent strain interval, which allows to more than quadrupling toughness (Table 5.1). On the contrary, the *Overhand Loop* tends to further tighten as the fibre is pulled ((Figure 5.7 b). Thus, in order to release completely the fibre without any damage, it is necessary to start from a very loose configuration. This, however, causes the fibre not to be very stressed, except at the end of the test, providing a much less significant toughness enhancement.

On average, with reference to the single turned slip knot, higher toughness values are reported for natural silk than for degummed silk. This is related to the possibility for natural fibres to dissipate more energy by friction, thus reaching a stress plateau much closer to their fracture strength, as it emerges if the stress values reported in Figure 5.8 are normalized with respect to the corresponding fracture strength. The *Overhand Loop* topology produces instead comparable results for both natural and degummed fibres.

Such different behaviour can be explained by considering the role played by sericin coating. In fact, natural silk fibres are less smooth than degummed fibres and they are more prone to friction as they run through the knot. However, when the knot is always able to unfasten (e.g., *Noose*), this is an added value and contributes positively to further increase the fibre toughness. Conversely, when for the fibre running throughout its loop is difficult as the knot tends to tie during tensile tests (e.g., *Overhand Loop*), any additional friction source can further hinder sliding, causing damage and premature failure of the fibre (Fig. 5e-g).

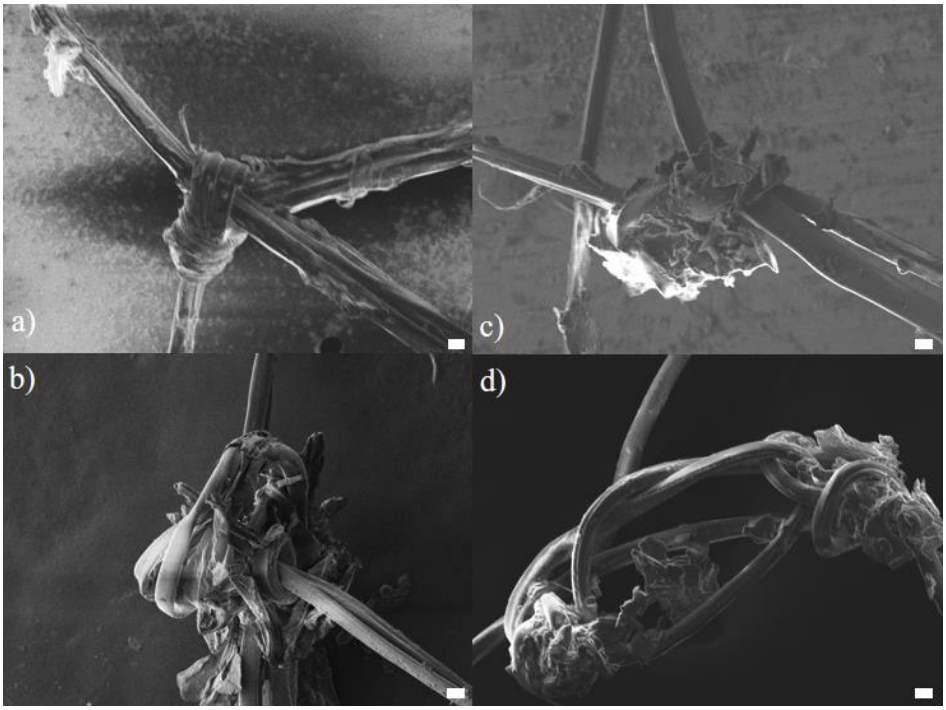

Figure 5.9 a) Unfastening mechanism of the Noose, which tends to loosen as the fiber ends are pulled apart. Such knot can always be released, even when extremely tight, as shown in the SEM image. b) Unfastening mechanism of the Overhand Loop, which tends to further tie as the fiber ends are pulled apart. Thus, if this knot is too tight at the beginning of the test, it cannot be released, as occurred in the natural silk fiber reported in the SEM image (b), which broke at the knot entrance. The sericin coating looks significantly damaged by friction. c) SEM image of a fiber with a Chain Knot with four chains visibly damaged by preparation, which caused superficial exfoliation. (d) SEM image of a fiber with a Chain Knot with six chains not uniformly tightened during preparation. Scale bars: 10 µm

Both the *Chain Knot* and *X-Knot* evolve from the *Noose* and provide different results, depending on a different sliding mechanism which the fibre experiences before the knot is completely unfastened (Figure 5.7 c and d). In this context, the *Chain Knot* behaves more similar to the *Noose*, since the chain closer to the loop tends to open as the fibre ends are pulled apart, thus the fibre can slide easily within the loop and the knot tends to further untie (Figure 5.7 d). On the contrary, a part of the *X-Knot* tends to tie when the fibre is pulled (Figure 5.7 c). The fibre

appears to be turned twice, but while one turn (which is the closest to the loop) tends to tie as the fibre ends are pulled apart, the second one (on the opposite side) tends to untie. This means that the knot can always be released, but with significant energy dissipation, causing the fibre to be much more stressed during the test and toughness to be more than four times bigger than the reference (Table 5.2).

The influence of the number of chains on the friction potential of the *Chain Knot* are also investigated. First of all, compared to other knots, chain knots with multiple chains require increasing manipulation, which, on turn, could induce some superficial exfoliations into the knotted fibre (Figure 5.9). On the one hand, this could contribute in enhancing the energy dissipated by friction during unfastening, as the fibre surface becomes rougher, but, on the other hand, it could also affect the fibre fracture strength, if too much damage is introduced. From a quantitative point of view, these results show that the introduction of 2 chains in the chain knot causes about a twofold toughness increase with respect to the average data obtained with 4 and 6 chains, which are comparable (Table 5.2). This indicates that in the latter cases, the friction potential is not fully exploited, as it is difficult to guarantee all chains in the knot to be uniformly tightened (Figure 5.9). Nevertheless, in some cases, a much more significant increase of almost 400% is achieved, meaning that there is still room for further increase, which could be obtained through the implementation of a controlled and repeatable production process, as that used in the textile industry.

Finally, the effectiveness of different knot topologies in enhancing the toughness of single silk fibres is compared. The knots considered herein are characterized by different design complexity, but have common features to be able to completely unfasten when the fibre opposite ends were pulled apart. Such condition allows on the one hand to not introduce any stress concentration, which could cause premature failure of the fibre, and on the other hand to dissipate an even significant amount of energy depending on the knot design. Such results are very

promising, since, as stated before, some of the tested knots are already known in the textile industry. Thus, the availability of industrial machinery able to process knots with high quality and repeatability could easily allow them to be implemented in industrial products requiring strong energy dissipation capability. The silk toughness could be further increased by considering longer loop to fibre length ratio than that of our experiments, or introducing multiple slip knots within the same fibre. Thus, the results presented in this study could be of help for future investigations, as the work proposed by Bosia et al. (Bosia et al. 2016), where they proposed knots inside synthetic fibres and carbon nanotubes, in order to provide optimizing systems with toughness modulus up to 1400 J/g.

5.7. Supplementary information on silk tensile tests

Supplementary Tables report the results obtained from tensile tests on both raw and degummed single silk fibers provided with the *Noose* and the *Overhand Loop* topologies. In particular, a variety of data can be found, including the strength and the toughness modulus (T_k) of knotted fibers, the toughness modulus of knotted samples computed after complete knot release (T_u'), the toughness modulus of a reference unknotted fiber (T_u) when T_u' could not be clearly identified. Toughness modulus values are computed considering a density of 1.4 g/cm^3 (Ashby 2011). Supplementary Tables include also the values of the mean stress reached by samples over 0% - 40% of their strain at break. In fact, the average stress value reached by knotted fibers at the beginning of tensile tests is indicative of the friction force and thus of the tightness quality of implemented knot. The values of toughness modulus reported in Table 5.1 are computed as average over those values corresponding to samples which reached an average friction stress above the threshold value of 8% of the sample strength. Samples satisfying such requirement are highlighted in both supplementary Table 5.3 and Table 5.5. Conversely, the other values of toughness modulus reported in Table 5.1 are computed as average over those values corresponding to samples, which reached

an average friction stress below the threshold. In case of the *Overhand Loop*, neither sample reaches a friction mean stress above the threshold, thus demonstrating its low efficiency if compared to the *Noose* topology.

Material	Sample number	Strength [MPa]	Friction stress/strength	T_k [J/g]	T_u' [J/g]	T_u [J/g]
Raw silk	1	-	-	-	-	-
Raw silk	2	305	25.5%	67.7	-	32.6
Raw silk	3	246	29.0%	53.1	-	19.6
Raw silk	4	269	25.0%	52.1	23.1	
Raw silk	5	200	23.1%	37.1	-	8.5
Raw silk	6	196	38.6%	42.5	-	8.5
Raw silk	7	115	0.4%	3.5	2.6	-
Raw silk	8	226	1.0%	18.8	17.4	-
Raw silk	9	191	1.3%	22.1	20.4	-
Raw silk	10	220	6.2%	20.3	14.2	-
Raw silk	11	246	3.1%	25.1	21.8	-
Raw silk	12	183	30.2%	39.4	7.7	-
Raw silk	13	165	24.7%	27.8	7.3	-
Raw silk	14	-	-	-	-	-
Raw silk	15	269	5.1%	30.7	23.5	-
Raw silk	16	244	1.4%	13.6	11.9	-
Raw silk	17	242	4.1%	21.5	17.6	-
Raw silk	18	268	17.0%	41.7	22.9	-
Raw silk	19	191	6.8%	18.0	-	8.5

Table 5.3 Raw silk fibers with single turned slip knot: Strength, average friction stress/strength over 0% - 40% of the strain at break, toughness modulus (T_k), toughness modulus after knot unfastening of knotted fibers (T_u'), toughness modulus of reference unknotted samples (T_u).

Material	Sample number	Strength [MPa]	Friction stress/strength	T_k [J/g]	T_u' [J/g]
Raw silk	1	235	0.1%	-	-
Raw silk	2	297	0.0%	14.1	13.9
Raw silk	3	312	0.5%	31.6	31.2
Raw silk	4	171	0.1%	8.0	7.3

Raw silk	5	243	0.5%	18.7	18.3
Raw silk	6	175	0.6%	12.4	10.6
Raw silk	7	-	-	-	-
Raw silk	8	111	0.8%	-	-
Raw silk	9	117	0.8%	-	-
Raw silk	10	198	1.8%	-	-
Raw silk	11	157	1.1%	-	-
Raw silk	12	7	-	-	-
Raw silk	13	236	0.9%	-	-
Raw silk	14	226	0.5%	-	-
Raw silk	15	212	0.5%	11.9	10.5
Raw silk	16	219	0.4%	12.5	11.7
Raw silk	17	267	0.2%	-	-
Raw silk	18	209	0.4%	-	-
Raw silk	19	273	0.4%	26.1	23.8

Table 5.4 Raw silk fibers with double turned slip knot: Strength, average friction stress/strength over 0% - 40% of the strain at break, toughness modulus (T_k), toughness modulus after knot unfastening of knotted fibers (T_u').

Material	Sample number	Strength [MPa]	Friction stress/strength	T_k [J/g]	T_u' [J/g]
Degummed silk	1	396	13.1%	27.3	8.4
Degummed silk	2	508	4.9%	48.0	34.4
Degummed silk	3	-	-	-	-
Degummed silk	4	325	1.4%	22.8	21.6
Degummed silk	5	675	0.6%	67.1	64.4
Degummed silk	6	452	3.0%	24.4	16.0
Degummed silk	7	410	9.0%	36.8	19.5
Degummed silk	8	401	6.0%	25.3	17.2
Degummed silk	9	-	-	-	-
Degummed silk	10	-	-	-	-
Degummed silk	11	420	7.5%	30.3	17.0
Degummed silk	12	223	8.2%	18.8	5.8

Table 5.5 Degummed silk fibers with single turned slip knot: Strength, average friction stress/strength over 0% - 40% of the strain at break, toughness modulus (T_k), toughness modulus after knot unfastening of knotted fibers (T_u').

Material	Sample number	Strength [MPa]	Friction stress/strength	T_k [J/g]	T_u' [J/g]
Degummed silk	1	-	-	-	-
Degummed silk	2	-	-	-	-
Degummed silk	3	225	0.5%	5.0	3.3
Degummed silk	4	318	0.7%	15.5	10.8
Degummed silk	5	518	0.0%	-	-
Degummed silk	6	-	-	-	-
Degummed silk	7	-	-	-	-
Degummed silk	8	-	-	-	-
Degummed silk	9	-	-	-	-
Degummed silk	10	624	0.0%	32.6	31.0
Degummed silk	11	-	-	-	-
Degummed silk	12	-	-	-	-
Degummed silk	13	-	-	-	-
Degummed silk	14	455	2.2%	34.4	32.0
Degummed silk	15	-	-	-	-
Degummed silk	16	243	0.4%	7.2	4.9
Degummed silk	17	-	-	-	-
Degummed silk	18	370	0.6%	13.6	13.2
Degummed silk	19	-	-	-	-
Degummed silk	20	489	0.4%	35.1	34.1
Degummed silk	21	497	0.2%	57.1	56.3
Degummed silk	22	-	-	-	-
Degummed silk	23	391	0.3%	22.2	21.1
Degummed silk	24	-	-	-	-
Degummed silk	25	-	-	-	-
Degummed silk	26	-	-	-	-
Degummed silk	27	470	0.8%	45.1	42.9
Degummed silk	28	696	1.2%	47.0	42.8

Table 5.6 Degummed silk fibers with double turned slip knot: Strength, average friction stress/strength over 0% - 40% of the strain at break, toughness modulus (T_k), toughness modulus after knot unfastening of knotted fibers (T_u').

Finally, some reference values of toughness modulus or strength of control raw or degummed single silk unknotted fibers are provided in Table 5.7 and Table 5.8, respectively. The average of the reported values were included in Table 5.1.

Material	Sample number	Diameter [μm]	Strength [MPa]	T_u [J/g]
Raw silk	1	21	271	32.6
Raw silk	2	20	251	19.6
Raw silk	3	21	179	8.5
Raw silk	4	19	315	36.2
Raw silk	5	22	236	27.1
Raw silk	6	25	171	18.1
Raw silk	7	18	231	18.1
Raw silk	8	19	97	4.1
	Mean	21	219	20.5
	St. Dev.	2	68	11.1

Table 5.7 Strength and toughness modulus of control raw silk unknotted fibers.

Material	Sample number	Diameter [μm]	Strength [MPa]	T_u [J/g]
Degummed silk	1	12	339	15.0
Degummed silk	2	8	646	43.5
Degummed silk	3	12	441	47.9
Degummed silk	4	12	415	17.6
Degummed silk	5	12	544	26.4
Degummed silk	6	14	490	24.8
Degummed silk	7	14	496	18.7
Degummed silk	8	14	474	40.1
	Mean	12	481	29.3
	St. Dev.	2	91	12.8

Table 5.8 Strength and toughness modulus of control degummed silk unknotted fibers.

Conclusions

The overall research in this thesis is devoted to extend our current knowledge in tribology. The world *tribology* comprises several interlinked complex phenomena. In this work, I aimed at describing friction from an analytical and numerical point of view, and, at the same time, to find some challenging and useful applications of friction, taking inspiration from the biological world.

Since a good understanding of all features would require a multidisciplinary background, I focused especially on dry friction, except for the ice friction modelling, in which a lubricant (i.e. water) is present.

By developing the analytical model for 1D and 2D surface roughness (the Anisotropic Lattice Spring Friction Model), which and how parameters influence the frictional behaviour of the model are described, such as local friction coefficient, direction of sliding, amplitude and wavelength of the surfaces. The friction coefficient strongly depends on the roughness of the surfaces involved and on the sliding direction β. Generic 1D roughness displays higher friction coefficient rather than the saw tooth shape, with a variation up to 40% less, moving from β = 0° to 90°. By introducing 2D roughness, the results of this investigation highlight that symmetrical surfaces seem to be more influenced by their shape, rather than the direction of sliding, while with non-symmetrical surfaces (different wavelength in the x and y directions), the sliding direction affects up to 30-40% the dynamic friction coefficient when β varies from 0° to 90°.

Then, other effects are introduced, namely adhesion, sliding wear and hierarchical structures. Adhesion can be introduced by imposing that the springs governing the interaction at the interface can be subjected to tensile forces. This aspect causes an increase in both the total compression force acting on the asperities and in the

apparent friction coefficient. Results show that, when adhesion affects the contact between surfaces, a tangential force is still present even if there is no normal load. Wear is adopted as a process that reduces the friction coefficient in time and smooths the asperities. The effect is more evident if the sliding is along the profile with sharper roughness (e.g. β equal to 0 for 1D roughness). If hierarchical self-similar levels are present, they contribute in enhancing the friction coefficient in a non-linear way. The effect of wear in the presence of hierarchical surfaces, provides the model with the prediction of the friction coefficient, which decreases in time due to sliding wear.

A particular case of lubricated friction is studied, dealing with the tribological behaviour of ice. Three different degrees of random roughness are introduced on stainless-steel surface pins, one comparable to the roughness of the ice and the other two one order of magnitude higher. Both the temperature of the system and the sliding velocity vary in a wide range.

It is shown that surface morphology influences the tribological regime of the system. In the boundary regime the higher the roughness, the higher the coefficient of friction. By increasing the sliding velocity (and thus the thickness of the water layer on the interface), the role of the interlocking asperity contacts becomes less relevant and the roughness has a lower influence on the coefficient of friction.

The experimental results are explained by applying the 1D-ASLFM that includes roughness and describes the local coefficient of friction in terms of shear stress of the water originated from the melting of ice at the interface. The only unknown parameter, the real contact area, is estimated both from the fits and through the bearing-ratio curve and the roughness parameters of the steel surfaces. The good fits between the model and the experimental data obtained with the two rougher sliders confirm the validity of both the model and the physical hypotheses about the mechanism of sliding friction on ice. The tribological behaviour of pin #1, characterized by the smoothest roughness, is proved to belong to the boundary

regime rather than the mixed regime. For this reason, the model can not describe its friction and estimate the contact length.

Referring to tribological tests, five various surface pattern configurations are studied. They have been realised from direct copy of silicon substrate with micro pillars on the surface, resulting in micro holes on PDMS surface samples. Results show how surface patterns influence the frictional behaviour. This is partly due to a decrease in the real contact area of textured samples although other aspects may contribute to this trend, including stress concentrations around surface features or the effect of adhesion, which has a higher influence at lower loads, especially on the surfaces with higher texture density. Thus, experiments are combined with a numerical study and results show both good repeatability and consistency. Anisotropic patterns generated a variation of friction forces of up to 300% depending on the sliding direction in the plane, thus producing directionally tuned friction.

Finally, how friction can be used to increase the toughness of one-dimensional elements, thanks to slip knots on single silkworm silk fibres is presented. This study demonstrates that, under optimized conditions, a slip knot introduced within the fibre can increase its energy dissipation capability, without causing significant damage to the fibre and avoiding significant stress concentration at the knot entrance. Four different topologies are considered and two opposite unfasten mechanisms. Although both mechanisms allow the fibre to slide within their loop, thus promoting energy dissipation, the *Noose* and the *X-knot* provided the best results, with respectively more than three times and four times toughness enhancement compared to a reference unknotted sample.

To summarize, the Anisotropic Lattice Spring Friction Model, thanks to its versatility, appears to be highly adaptable to various situations, even to the ice friction, opening further developments of application in other tribological systems. The presence of hierarchy shows that surfaces with hierarchical self-affine

structures can be seen as a smart way to increase the friction coefficient. The experimental parts provide new insights on friction and how to tune tribological properties of materials.

The results of this thesis justify future developments from both experimental and numerical points of view. Experiments on controlled rough surfaces will be realized to validate the model. Moreover, new features will be introduced inside the numerical formulation, such as random roughness and static friction force, overcoming the limits due to periodic and derivable surfaces.

Bibliography

Absi, E. and W. Prager. 1975. “A Comparison of Equivalence and Finite Element Methods.” *Computer Methods in Applied Mechanics and Engineering* 6(1):59–64.

Albracht, F. 2004. “On the Influences of Friction on Ice.” *Materialwissenschaft Und Werkstofftechnik* 35:620.

Altman, Gregory H. et al. 2003. “Silk-Based Biomaterials.” *Biomaterials* 24(3):401–16.

Anstee, R. P., J. H. Przytycki, and D. Rolfsen. 1989. “Knot Polynomials and Generalized Mutation.” *Topology and Its Applications* 32(3):237–49.

Antoni, N., J. L. Ligier, P. Saffré, and J. Pastor. 2007. “Asymmetric Friction: Modelling and Experiments.” *International Journal of Engineering Science* 45(2–8):587–600.

Arai, Yasuharu et al. 1999. “Tying a Molecular Knot with Optical Tweezers.” *Nature* 399(6735):446–48.

Archard, J. F. 1953. “Contact and Rubbing of Flat Surfaces.” *Journal of Applied Physics* 24(8):981–88.

Archard, J. F. 1957. “Elastic Deformation and the Laws of Friction Article Cited In :” *Proc. R. Soc. Lond. A* 190–205.

Ashby, Michael F. 2011. *Materials Selection in Mechanical Design*. Retrieved (http://linkinghub.elsevier.com/retrieve/pii/B9781856176637000011).

Ashley, C. W. 1944. *The Ashley Book of Knots*. New York,: NY: Doubleday, Doran and Co. Inc.

Autumn, Kellar et al. 2000. “Adhesive Force of a Single Gecko Foot-Hair.” *Nature* 405(6787):681–85.

Ayme, Jean François et al. 2012. “A Synthetic Molecular Pentafoil Knot.” *Nature Chemistry* 4(1):15–20.

Baum, Martina J., Lars Heepe, Elena Fadeeva, and Stanislav N. Gorb. 2014. “Dry Friction of Microstructured Polymer Surfaces Inspired by Snake

Skin." *Beilstein Journal of Nanotechnology* 5(1):1091–1103.

Bäurle, L., Th U. Kaempfer, D. Szabó, and N. D. Spencer. 2007. "Sliding Friction of Polyethylene on Snow and Ice: Contact Area and Modeling." *Cold Regions Science and Technology* 47(3):276–89.

Bayer, R. K. 1994. "Structure Transfer from a Polymeric Melt to the Solid State Part III: Influence of Knots on Structure and Mechanical Properties of Semicrystalline Polymers." *Colloid & Polymer Science* 272(8):910–32. Retrieved (http://link.springer.com/10.1007/BF00658889).

Berardo, A., M. F. Pantano, and N. M. Pugno. 2016. "Slip Knots and Unfastening Topologies Enhance Toughness without Reducing Strength of Silk Fibroin Fibres." *Interface Focus* 6(1).

Bhushan, B. and A. Majumdar. 1992. "Elastic-Plastic Contact Model for Bifractal Surfaces." *Wear* 153(1):53–64.

Bhushan, Bharat. 2007. "Adhesion of Multi-Level Hierarchical Attachment Systems in Gecko Feet." *Journal of Adhesion Science and Technology* 21(12–13):1213–58.

Bistac, S. and A. Galliano. 2005. "Nano and Macro Tribology of Elastomers." *Tribology Letters* 18(1):21–25.

Boesel, Luciano F., Christian Cremer, Eduard Arzt, and Aránzazu Del Campo. 2010. "Gecko-Inspired Surfaces: A Path to Strong and Reversible Dry Adhesives." *Advanced Materials* 22(19):2125–37.

Bonani, W., D. Maniglio, A. Motta, W. Tan, and C. Migliaresi. 2011. "Biohybrid Nanofiber Constructs with Anisotropic Biomechanical Properties." *Journal of Biomedical Materials Research - Part B Applied Biomaterials* 96 B(2):276–86.

Borodich, F. M. and D. a. Onishchenko. 1999. "Similarity and Fractality in the Modelling of Roughness by a Multilevel Profile with Hierarchical Structure." *International Journal of Solids and Structures* 36(17):2585–2612.

Bosia, Federico et al. 2016. "Knotted Synthetic Polymer or Carbon Nanotube Microfibres with Enhanced Toughness, up to 1400 J/G." *Carbon* 102:116–25.

Bouville, Florian et al. 2014. "Strong, Tough and Stiff Bioinspired Ceramics from Brittle Constituents." *Nature Materials* 13(5):508–14.

Bowden, F. .. and T. P. Hughes. 1939. “The Mechanism of Sliding on Ice and Snow.” *Proceedings of the Royal Society of London* A 172:280–98.

Bowden, F. P., D. Tabor, and Frederic Palmer. 1951. “The Friction and Lubrication of Solids.” *American Journal of Physics* 19(7):428–29. Retrieved (http://aapt.scitation.org/doi/10.1119/1.1933017).

Braun, O. M. and Y. S. Kivshar. 2004. *The Frenkel-Kontorova Model: Concepts, Methods, and Applications*. Berlin: Springer-Verlag.

Brown, Stephen R. 1987. “A Note on the Description of Surface Roughness Using Fractal Dimension.” *Geophysical Research Letters* 14(11):1095–98.

Capozza, R. and Nicola Pugno. 2015. “Effect of Surface Grooves on the Static Friction of an Elastic Slider.” *Tribology Letters* 58(3):35.

Carbone, G. and F. Bottiglione. 2008. “Asperity Contact Theories: Do They Predict Linearity between Contact Area and Load?” *Journal of the Mechanics and Physics of Solids* 56(8):2555–72.

Carbone, G. and F. Bottiglione. 2011. “Contact Mechanics of Rough Surfaces: A Comparison between Theories.” *Meccanica* 46(3):557–65.

Carbone, G., B. Lorenz, B. N. J. Persson, and A. Wohlers. 2009. “Contact Mechanics and Rubber Friction for Randomly Rough Surfaces with Anisotropic Statistical Properties.” *European Physical Journal E* 29(3):275–84.

Carbone, G. and L. Mangialardi. 2004. “Adhesion and Friction of an Elastic Half-Space in Contact with a Slightly Wavy Rigid Surface.” *Journal of the Mechanics and Physics of Solids* 52(6):1267–87.

Caroli, C. and P. Nozières. 1998. “Hysteresis and Elastic Interactions of Microasperities in Dry Friction.” *European Physical Journal B* 4:233–46.

Caroli, C. and Ph Nozières. 1998. “Hysteresis and Elastic Interactions of Microasperities in Dry Friction.” *European Physical Journal B* 4(2):233–46.

Chen, Qiang, Francesco Baino, Silvia Spriano, and Nicola M. Pugno. 2014. “Modelling of the Strength – Porosity Relationship in Glass-Ceramic Foam Scaffolds for Bone Repair.” 34:2663–73.

Cheung, Hoi Yan, Kin Tak Lau, Xiao Ming Tao, and David Hui. 2008. “A Potential Material for Tissue Engineering: Silkworm Silk/PLA Biocomposite.” *Composites Part B: Engineering* 39(6):1026–33.

Colbeck, S. C. et al. 1975. “Snow and Ice.” *Reviews of Geophysics* 13(3):435–41.

Colbeck, S. C. 1988. “The Kinetic Friction of Snow.” *Journal of Glaciology* 34(116):78–86.

Colomban, Philippe and Hung Manh Dinh. 2012. “Origin of the Variability of the Mechanical Properties of Silk Fibres: 2 the Nanomechanics of Single Silkworm and Spider Fibres.” *Journal of Raman Spectroscopy* 43(8):1035–41.

Costagliola, G., F. Bosia, and N. M. Pugno. 2018. “A 2-D Model for Friction of Complex Anisotropic Surfaces.” *Journal of the Mechanics and Physics of Solids* 112:50–65.

Costagliola, Gianluca, Federico Bosia, and Nicola M. Pugno. 2016. “Static and Dynamic Friction of Hierarchical Surfaces.” *Physical Review E* 94(6):1–10.

Costagliola, Gianluca, Federico Bosia, and Nicola M. Pugno. 2017. “Hierarchical Spring-Block Model for Multiscale Friction Problems.” *ACS Biomaterials Science & Engineering* 3(11):2845–52.

Coulomb, C. A. 1821. *Theorie Des Machines Simple (Theory of Simple Machines)*. Paris: Bachelier.

Cranford, Steven W., Anna Tarakanova, Nicola M. Pugno, and Markus J. Buehler. 2012. “Nonlinear Material Behaviour of Spider Silk Yields Robust Webs.” *Nature* 482(7383):72–76.

Dash, J. G. 2003. “Theory of a Tribometer Experiment on Ice Friction.” *Scripta Materialia* 49(10 SPEC.):1003–6.

Dean, F. B., A. Stasiak, T. Koller, and N. R. Cozzarelli. 1985. “Duplex DNA Knots Produced by Escherichia Coli Topoisomerase I. Structure and Requirements for Formation.” *Journal of Biological Chemistry* 260(8):4975–83.

Derjaguin, B. V, V. M. Muller, and Y. U. P. Toporov. 1975. “Effect of Contact Deformation on the Adhesion of Particles.” *Journal of Colloid and Interface Science* 52(3):105–8.

Dowson, D. 1979. *History of Tribology*. London: Longman Group Limited.

Du, Yinghong et al. 2015. “Mechanical Properties of the Hierarchical Honeycombs with Stochastic Voronoi Sub-Structures.” *EPL (Europhysics*

Letters) 111(5):56007. Retrieved (http://stacks.iop.org/0295-5075/111/i=5/a=56007?key=crossref.d3d2592ff45e9db8c78250ea3f62f70c).

Ducret, S., H. Zahouani, A. Midol, P. Lanteri, and T. G. Mathia. 2005. "Friction and Abrasive Wear of UHWMPE Sliding on Ice." Pp. 26–31 in *Wear*, vol. 258.

Erdemir, A. 2005. "Review of Engineered Tribological Interfaces for Improved Boundary Lubrication." *Tribology International* 38(3):249–56.

Etsion, I. 2004. "Improving Tribological Performance of Mechanical Components by Laser Surface Texturing." *Tribology Letters* 17(4):733–37.

Etsion, Izhak. 2005. "State of the Art in Laser Surface Texturing." *Journal of Tribology* 127(1):248. Retrieved (http://tribology.asmedigitalcollection.asme.org/article.aspx?articleid=1467274).

Evans, D. C. B., J. F. Nye, and K. J. Cheeseman. 1976. "The Kinetic Friction of Ice." *Proc. R. Soc. Lond. A* 347(1651):493–512. Retrieved (http://rspa.royalsocietypublishing.org/content/347/1651/493).

Fantner, Georg E. et al. 2006. "Sacrificial Bonds and Hidden Length: Unraveling Molecular Mesostructures in Tough Materials." *Biophysical Journal* 90(4):1411–18.

Filippov, Alexander and Stanislav N. Gorb. 2013. "Frictional-Anisotropy-Based Systems in Biology: Structural Diversity and Numerical Model." *Scientific Reports* 3.

Forgan, Ross S., Jean Pierre Sauvage, and J. Fraser Stoddart. 2011. "Chemical Topology: Complex Molecular Knots, Links, and Entanglements." *Chemical Reviews* 111(9):5434–64.

Fuller, K. N. G. and D. Tabor. 1975. "The Effect of Surface Roughness on the Adhesion of Elastic Solids." *Proceedings of the Royal Society A: Mathematical, Physical and Engineering Sciences* 345(1642):327–42. Retrieved (http://rspa.royalsocietypublishing.org/cgi/doi/10.1098/rspa.1975.0138).

Fülöp, Tibor and Ari J. Tuononen. 2013. "Evolution of Ice Surface under a Sliding Rubber Block." *Wear* 307(1–2):52–59.

Gagnepain, J. J. and C. Roques-Carmes. 1986. "Fractal Approach to Two-Dimensional and Three-Dimensional Surface Roughness." *Wear* 109(1–

4):119–26.

Galliano, A., S. Bistac, and J. Schultz. 2003. "Adhesion and Friction of PDMS Networks: Molecular Weight Effects." *Journal of Colloid and Interface Science* 265(2):372–79.

Ghio, Simone et al. 2015. "Fast and Large Area Fabrication of Hierarchical Bioinspired Superhydrophobic Silicon Surfaces." *Journal of the European Ceramic Society* 36:2363–69.

Greenwood, J. A. 1997. "Adhesion of Elastic Spheres." *Proceedings of the Royal Society A: Mathematical, Physical and Engineering Sciences* 453(1961):1277–97. Retrieved (http://rspa.royalsocietypublishing.org/cgi/doi/10.1098/rspa.1997.0070).

Greenwood, J. A. and J. B. P. Williamson. 1966. "Contact of Nominally Flat Surfaces." *Proceedings of the Royal Society A: Mathematical, Physical and Engineering Sciences* 295(1442):300–319. Retrieved (http://rspa.royalsocietypublishing.org/cgi/doi/10.1098/rspa.1966.0242).

Greiner, Christian, Michael Scha, Uwe Popp, and Peter Gumbsch. 2014. "Contact Splitting and the E Ff Ect of Dimple Depth on Static Friction of Textured Surfaces." *ACS Applied Materials and Interfaces (Supporting)* 1–6.

Gualtieri, E. et al. 2011. "Role of Roughness Parameters on the Tribology of Randomly Nano-Textured Silicon Surface." *Journal of Nanoscience and Nanotechnology* 11:9244–50.

Gualtieri, E., A. Borghi, L. Calabri, N. Pugno, and S. Valeri. 2009. "Increasing Nanohardness and Reducing Friction of Nitride Steel by Laser Surface Texturing." *Tribology International* 42(5):699–705.

Hardy, John G., Lin M. Römer, and Thomas R. Scheibel. 2008. "Polymeric Materials Based on Silk Proteins." *Polymer* 49(20):4309–27.

Hatton, D. C., P. R. Sammonds, and D. L. Feltham. 2009. "Ice Internal Friction: Standard Theoretical Perspectives on Friction Codified, Adapted for the Unusual Rheology of Ice, and Unified." *Philosophical Magazine* 89(31):2771–99.

He, Bo, Wei Chen, and Q. Jane Wang. 2008. "Surface Texture Effect on Friction of a Microtextured Poly(Dimethylsiloxane) (PDMS)." *Tribology Letters* 31(3):187–97.

He, Chengzhi, Guillaume Lamour, Adam Xiao, Joerg Gsponer, and Hongbin Li.

2014. “Mechanically Tightening a Protein Slipknot into a Trefoil Knot.” *Journal of the American Chemical Society* 136(34):11946–55.

Hench, Larry L. 1998. “Biomaterials: A Forecast for the Future.” *Biomaterials* 19(16):1419–23.

Hersel, Ulrich, Claudia Dahmen, and Horst Kessler. 2003. “RGD Modified Polymers: Biomaterials for Stimulated Cell Adhesion and Beyond.” *Biomaterials* 24(24):4385–4415.

Hertz, H. 1882. “Ueber Die Verdunstung Der Flüssigkeiten, Insbesondere Des Quecksilbers, Im Luftleeren Raume.” *Annalen Der Physik* 253(10):177–93.

Higgins, Daniel D., Brett A. Marmo, Christopher E. Jeffree, Vasileios Koutsos, and Jane R. Blackford. 2008. “Morphology of Ice Wear from Rubber-Ice Friction Tests and Its Dependence on Temperature and Sliding Velocity.” *Wear* 265(5–6):634–44.

Hsu, Stephen M., Yang Jing, Diann Hua, and Huan Zhang. 2014. “Friction Reduction Using Discrete Surface Textures: Principle and Design.” *Journal of Physics D: Applied Physics* 47(33):335307. Retrieved (http://stacks.iop.org/0022-3727/47/i=33/a=335307?key=crossref.7e0896fa2c22b172dc6ca28cd9d03ce5).

Hubbell, J. a. 1995. “Biomaterials in Tissue Engineering.” *Bio/Technology (Nature Publishing Company)* 13(6):565–76.

Jacobsen, Stefan, George W. Scherer, and Erland M. Schulson. 2015. “Concrete-Ice Abrasion Mechanics.” *Cement and Concrete Research* 73:79–95.

Jiang, Ping et al. 2006. “Tensile Behavior and Morphology of Differently Degummed Silkworm (Bombyx Mori) Cocoon Silk Fibres.” *Materials Letters* 60(7):919–25.

Jin, Hyoung Joon and David L. Kaplan. 2003. “Mechanism of Silk Processing in Insects and Spiders.” *Nature* 424(6952):1057–61.

Jin, Zhongmin and Duncan Dowson. 2013. “Bio-Friction.” *Friction* 1(2):100–113.

Johnson, K. L., K. Kendall, and A. D. Roberts. 1971. “Surface Energy and the Contact of Elastic Solids.” *Proceedings of the Royal Society A: Mathematical, Physical and Engineering Sciences* 324(1558):301–13. Retrieved (http://rspa.royalsocietypublishing.org/cgi/doi/10.1098/rspa.1971.0141).

Johnston, I. D., D. K. McCluskey, C. K. L. Tan, and M. C. Tracey. 2014. "Mechanical Characterization of Bulk Sylgard 184 for Microfluidics and Microengineering." *Journal of Micromechanics and Microengineering* 24(3).

Jones, S. J., H. Kitagawa, K. Izumiyama, and H. Shimoda. 1994. "Friction of Melting Ice." *Annals of Glaciology* 19:7–12.

Jung, Yong Chae and Bharat Bhushan. 2006. "Contact Angle , Adhesion and Friction Properties of Micro- and Nanopatterned Polymers for Superhydrophobicity."

Keum, Hohyun, Martin Mccormick, Ping Liu, Yong-wei Zhang, and Fiorenzo G. Omenetto. 2011. "RESEARCH ARTICLES Epidermal Electronics." 333(August).

Kietzig, Anne Marie, Savvas G. Hatzikiriakos, and Peter Englezos. 2009. "Ice Friction: The Effects of Surface Roughness, Structure, and Hydrophobicity." *Journal of Applied Physics* 106(2).

Kietzig, Anne Marie, Savvas G. Hatzikiriakos, and Peter Englezos. 2010. "Physics of Ice Friction." *Journal of Applied Physics* 107(8).

Kim, Dae-hyeong et al. 2011. "NIH Public Access." *Electronics* 9(6):511–17.

Kim, Dae Hyeong et al. 2009. "Silicon Electronics on Silk as a Path to Bioresorbable, Implantable Devices." *Applied Physics Letters* 95(13):93–96.

Kim, Tae Wan and Bharat Bhushan. 2007. "Effect of Stiffness of Multi-Level Hierarchical Attachment System on Adhesion Enhancement." *Ultramicroscopy* 107(10–11):902–12.

Klapproth, C., T. M. Kessel, K. Wiese, and B. Wies. 2016. "An Advanced Viscous Model for Rubber-Ice-Friction." *Tribology International* 99:169–81.

Kleckner, Dustin and William T. M. Irvine. 2013. "Creation and Dynamics of Knotted Vortices." *Nature Physics* 9(4):253–58.

de Koning, Jos J., Gert de Groot, and Gerrit Jan van Ingen Schenau. 1992. "Ice Friction during Speed Skating." *Journal of Biomechanics* 25(6):565–71.

Kriston, András, Nihat Ali Isitman, Tibor Fülöp, and Ari J. Tuononen. 2016. "Structural Evolution and Wear of Ice Surface during Rubber-Ice Contact." *Tribology International* 93:257–68.

Kundanati, Lakshminath et al. 2016. “Fabrication and Mechanical Characterization of Hydrogel Infused Network Silk Scaffolds.” *International Journal of Molecular Sciences* 17(10).

Lawrence, Brian D., Mark Cronin-Golomb, Irene Georgakoudi, David L. Kaplan, and Fiorenzo G. Omenetto. 2008. “Bioactive Silk Protein Biomaterial Systems for Optical Devices.” *Biomacromolecules* 9(4):1214–20.

Lawrence, Brian D., Jeffrey K. Marchant, Mariya A. Pindrus, Fiorenzo G. Omenetto, and David L. Kaplan. 2009. “Silk Film Biomaterials for Cornea Tissue Engineering.” *Biomaterials* 30(7):1299–1308. Retrieved (http://dx.doi.org/10.1016/j.biomaterials.2008.11.018).

Li, Ning, Erjiang Xu, Ze Liu, Xinyun Wang, and Lin Liu. 2016. “Tuning Apparent Friction Coefficient by Controlled Patterning Bulk Metallic Glasses Surfaces.” *Scientific Reports* 6(November):1–9. Retrieved (http://dx.doi.org/10.1038/srep39388).

Lishman, Ben, Peter Sammonds, and Danny Feltham. 2011. “A Rate and State Friction Law for Saline Ice.” *Journal of Geophysical Research: Oceans* 116(5).

Liskiewicz, T., A. Morina, and A. Neville. 2008. “Friction in Nature.” *WIT Transactions on Ecology and the Environment* 114(June 2008):263–72.

Maegawa, Satoru, Fumihiro Itoigawa, and Takashi Nakamura. 2016. “Effect of Surface Grooves on Kinetic Friction of a Rubber Slider.” *Tribology International* 102:326–32.

Majumdar, A. and C. L. Tien. 1990. “Fractal Characterization and Simulation of Rough Surfaces.” *Wear* 136(2):313–27.

Majumdar, a and B. Bhushan. 1991. “Fractal Model of Elastic-Plastic Contact between Rough Surfaces.” *Journal of Tribology-Transactions of the Asme* 113(1):1–11.

Makkonen, Lasse. 1997. “Surface Melting of Ice.” *The Journal of Physical Chemistry B* 101(32):6196–6200. Retrieved (http://pubs.acs.org/doi/abs/10.1021/jp963248c).

Makkonen, Lasse. 2012. “A Thermodynamic Model of Sliding Friction.” *AIP Advances* 2(1).

Makkonen, Lasse and Maria Tikanmäki. 2014. “Modeling the Friction of Ice.” *Cold Regions Science and Technology* 102:84–93.

Mandelli, Davide et al. 2015. "Superlubric-Pinned Transition in Sliding Incommensurate Colloidal Monolayers." *Physical Review B - Condensed Matter and Materials Physics* 92(13).

Mannoor, Manu S. et al. 2012. "Graphene-Based Wireless Bacteria Detection on Tooth Enamel." *Nature Communications* 3:763–68. Retrieved (http://dx.doi.org/10.1038/ncomms1767).

Marmo, Brett A., Jane R. Blackford, and Chris E. Jeffree. 2005. "Ice Friction, Wear Features and Their Dependence on Sliding Velocity and Temperature." *Journal of Glaciology* 51(174):391–98.

McCarthy, Matthew et al. 2012. "Biotemplated Hierarchical Surfaces and the Role of Dual Length Scales on the Repellency of Impacting Droplets." *Applied Physics Letters* 100(26):1–6.

Meinel, Anne J. et al. 2009. "Optimization Strategies for Electrospun Silk Fibroin Tissue Engineering Scaffolds." *Biomaterials* 30(17):3058–67.

Meluzzi, Dario, Douglas E. Smith, and Gaurav Arya. 2010. "Biophysics of Knotting." *Annual Review of Biophysics* 39(1):349–66. Retrieved (http://www.annualreviews.org/doi/10.1146/annurev.biophys.093008.131412).

Meng, H. C. and K. C. Ludema. 1995. "Wear Models and Predictive Equations: Their Form and Content." *Wear* 181–183(PART 2):443–57.

Mirkhalaf, M., A. Khayer Dastjerdi, and F. Barthelat. 2014. "Overcoming the Brittleness of Glass through Bio-Inspiration and Micro-Architecture." *Nature Communications* 5.

Mróz, Z. and S. Stupkiewicz. 1994. "An Anisotropic Friction and Wear Model." *International Journal of Solids and Structures* 31(8):1113–31.

Munch, E. et al. 2008. "Tough, Bio-Inspired Hybrid Materials." *Science* 322(5907):1516–20.

Murarash, Boris, Yan Itovich, and Michael Varenberg. 2011. "Tuning Elastomer Friction by Hexagonal Surface Patterning." *Soft Matter* 7(12):5553. Retrieved (http://xlink.rsc.org/?DOI=c1sm00015b).

Nguyen, D. T. et al. 2013. "Friction of Rubber with Surfaces Patterned with Rigid Spherical Asperities." *Tribology Letters* 49(1):135–44.

Norell, Jesper, Annalisa Fasolino, and Astrid S. De Wijn. 2016. "Emergent Friction in Two-Dimensional Frenkel-Kontorova Models." *Physical*

Review E 94(2).

Nosonovsky, M. and B. Bhushan. 2008. *Multiscale Dissipative Mechanisms and Hierarchical Surfaces*. New York: Springer Berlin Heidelberg.

Nosonovsky, Michael and Bharat Bhushan. 2007. "Multiscale Friction Mechanisms and Hierarchical Surfaces in Nano- and Bio-Tribology." *Materials Science and Engineering R: Reports* 58(3–5):162–93.

Nyberg, H., S. Alfredson, S. Hogmark, and S. Jacobson. 2013. "The Asymmetrical Friction Mechanism That Puts the Curl in the Curling Stone." *Wear* 301:583–89.

Oksanen, Pekka and Juhani Keinonen. 1982. "The Mechanism of Friction of Ice." *Wear* 78(3):315–24.

Omenetto, Fiorenzo G. and David L. Kaplan. 2008. "A New Route for Silk." *Nature Photonics* 2(11):641–43.

Omenetto, Fiorenzo G. and David L. Kaplan. 2010. "New Opportunities for an Ancient Material." 329(July):528–32.

Palmeri, Marc J., Karl W. Putz, and L. Catherine Brinson. 2010. "Sacrificial Bonds in Stacked-Cup Carbon Nanofibers: Biomimetic Toughening Mechanisms for Composite Systems." *ACS Nano* 4(7):4256–64.

Pantano, M. F., A. Berardo, and N. M. Pugno. 2016. "Tightening Slip Knots in Raw and Degummed Silk to Increase Toughness without Losing Strength." *Scientific Reports* 6.

Partlow, Benjamin P. et al. 2014. "Highly Tunable Elastomeric Silk Biomaterials." 4615–24.

Pérez-Rigueiro, J., M. Elices, J. Llorca, and C. Viney. 2001. "Tensile Properties of Silkworm Silk Obtained by Forced Silking." *Journal of Applied Polymer Science* 82(8):1928–35.

Pérez-Rigueiro, J., C. Viney, J. Llorca, and M. Elices. 2000. "Mechanical Properties of Single-Brin Silkworm Silk." *Journal of Applied Polymer Science* 75(10):1270–77.

Persson, B. N. J. 2000. *Sliding Friction: Physical Principles and Applications*. Retrieved (http://linkinghub.elsevier.com/retrieve/pii/S0167572998000090).

Persson, B. N. J. 2001. "Elastoplastic Contact between Randomly Rough Surfaces." *Physical Review Letters* 87(11):116101. Retrieved

(https://link.aps.org/doi/10.1103/PhysRevLett.87.116101).

Persson, B. N. J. 2006. "Contact Mechanics for Randomly Rough Surfaces." *Surface Science Reports* 61(4):201–27. Retrieved (http://linkinghub.elsevier.com/retrieve/pii/S0167572906000410).

Persson, B. N. J., O. Albohr, U. Tartaglino, A. I. Volokitin, and E. Tosatti. 2005. "On the Nature of Surface Roughness with Application to Contact Mechanics, Sealing, Rubber Friction and Adhesion." *Journal of Physics: Condensed Matter* 17(1):R1–62. Retrieved (http://stacks.iop.org/0953-8984/17/i=1/a=R01?key=crossref.7463e9973eaa58c09e5bdac3d1940d9d).

Persson, B. N. J., F. Bucher, and B. Chiaia. 2002. "Elastic Contact between Randomly Rough Surfaces: Comparison of Theory with Numerical Results." *Physical Review B* 65(18):184106. Retrieved (https://link.aps.org/doi/10.1103/PhysRevB.65.184106).

Persson, Bo N. J. 2000. *Sliding Friction*. 2nd ed. edited by Von Klitzing Klaus and Wiesendange Roland. Berlin, Heidelberg: Springer Berlin Heidelberg. Retrieved (http://link.springer.com/10.1007/978-3-662-04283-0).

Petrenko, F. and R. Whitworth. 1999. *Physics of Ice*. New York: Oxford University.

Pettersson, Ulrika and S. Jacobson. 2004. "Friction and Wear Properties of Micro Textured DLC Coated Surfaces in Boundary Lubricated Sliding." *Tribology Letters* 17(3):553–59.

Popov, V. L. and A. V. Dimaki. 2011. "Using Hierarchical Memory to Calculate Friction Force between Fractal Rough Solid Surface and Elastomer with Arbitrary Linear Rheological Properties." *Technical Physics Letters* 37(1):8–11. Retrieved (http://link.springer.com/10.1134/S106378501101010X).

Popova, Elena and Valentin L. Popov. 2015. "The Research Works of Coulomb and Amontons and Generalized Laws of Friction." *Friction* 3(2):183–90.

Pugno, N., E. Lepore, S. Toscano, and F. Pugno. 2011. "Normal Adhesive Force-Displacement Curves of Living Geckos." *Journal of Adhesion* 87(11):1059–72.

Pugno, Nicola M. 2006. "Mimicking Nacre with Super-Nanotubes for Producing Optimized Super-Composites." *Nanotechnology* 17(21):5480–84.

Pugno, Nicola M. 2014. "The 'Egg of Columbus' for Making the World's Toughest Fibres." *PLoS ONE* 9(4):1–6.

Pugno, Nicola M. and Alberto Carpinteri. 2007. “Nanomechanics of Hierarchical Biomaterials.” 661(2):11–21.

Pugno, Nicola M. and Alberto Carpinteri. 2008. “Design of Micro-Nanoscale Bio-Inspired Hierarchical Materials.” *Philosophical Magazine Letters* 88(6):397–405.

Pugno, Nicola M., Steven W. Cranford, and Markus J. Buehler. 2013. “Synergetic Material and Structure Optimization Yields Robust Spider Web Anchorages.” *Small* 9(16):2747–56.

Pugno, Nicola M. and Emiliano Lepore. 2008. “Observation of Optimal Gecko’s Adhesion on Nanorough Surfaces.” *BioSystems* 94(3):218–22.

Pugno, Nicola M., Qifang Yin, Xinghua Shi, and Rosario Capozza. 2013. “A Generalization of the Coulomb’s Friction Law: From Graphene to Macroscale.” *Meccanica* 48(8):1845–51.

Putignano, C., L. Afferrante, G. Carbone, and G. Demelio. 2012. “A New Efficient Numerical Method for Contact Mechanics of Rough Surfaces.” *International Journal of Solids and Structures* 49(2):338–43. Retrieved (http://dx.doi.org/10.1016/j.ijsolstr.2011.10.009).

Rand, Charles J. and Alfred J. Crosby. 2009. “Friction of Soft Elastomeric Wrinkled Surfaces.” *Journal of Applied Physics* 106(6).

Ranjan, R., D. N. Lambeth, M. Tromel, P. Goglia, and Y. Li. 1991. “Laser Texturing for Low-Flying-Height Media.” *Journal of Applied Physics* 69(8):5745–47.

Ritchie, Robert O. 2011. “The Conflicts between Strength and Toughness.” *Nature Materials* 10(11):817–22.

Roberts, A. D. and J. C. Richardson. 1981. “Interface Study of Rubber-Ice Friction.” *Wear* 67(1):55–69.

Sahli, R. et al. 2018. “Evolution of Real Contact Area under Shear and the Value of Static Friction of Soft Materials.” *Proceedings of the National Academy of Sciences* 201706434. Retrieved (http://www.pnas.org/lookup/doi/10.1073/pnas.1706434115).

Saitta, A. Marco, Paul D. Soper, E. Wasserman, and Michael L. Klein. 1999. “Influence of a Knot on the Strength of a Polymer Strand.” *Nature* 399(6731):46–48.

Schulson, Erland M. 2015. “Low-Speed Friction and Brittle Compressive

Failure of Ice: Fundamental Processes in Ice Mechanics." *International Materials Review* 60:451–78.

Schulson, Erland M. and Andrew L. Fortt. 2012. "Friction of Ice on Ice." *Journal of Geophysical Research B: Solid Earth* 117(12).

Senyuk, Bohdan et al. 2013. "Topological Colloids." *Nature* 493(7431):200–205.

Shao, Zhengzhong and Fritz Vollrath. 2002. "Surprising Strength of Silkworm Silk." *Nature* 418(6899):741.

Shu, N. P. 1986. *Tribophysics*. Prentice-Hall.

Spagni, A. et al. 2016. "Friction of Rough Surfaces on Ice: Experiments and Modeling." *Wear* 368–369.

Staiger, Mark P., Alexis M. Pietak, Jerawala Huadmai, and George Dias. 2006. "Magnesium and Its Alloys as Orthopedic Biomaterials: A Review." *Biomaterials* 27(9):1728–34.

Stamboulides, Christos, Peter Englezos, and Savvas G. Hatzikiriakos. 2012. "The Ice Friction of Polymeric Substrates." *Tribology International* 55:59–67.

Stewart Gillmor, C. 1971. *Coulomb and the Evolution of Physics and Engineering in Eighteenth-Century France*. Princeton: Princeton University Press.

Stupkiewicz, Stanisław, Maciej J. Lewandowski, and Jakub Lengiewicz. 2014. "Micromechanical Analysis of Friction Anisotropy in Rough Elastic Contacts." *International Journal of Solids and Structures* 51(23–24):3931–43.

Sukhorukov, Sergiy and Aleksey Marchenko. 2014. "Geometrical Stick-Slip between Ice and Steel." *Cold Regions Science and Technology* 100:8–19.

Tabor, D. 1977. "Surface Forces and Surface Interactions." *Journal of Colloid And Interface Science* 58(1):2–13.

Tkalec, Uroš, Miha Ravnik, Simon Čopar, Slobodan Žumer, and Igor Muševič. 2011. "Reconfigurable Knots and Links in Chiral Nematic Colloids." *Science* 333(6038):62–65.

Tramsen, H. T. et al. 2018. "Inversion of Friction Anisotropy in a Bio-Inspired Asymmetrically Structured Surface." *Journal of the Royal Society Interface* 15:2017062.

Ude, A. U., A. K. Ariffin, and C. H. Azhari. 2013. “An Experimental Investigation on the Response of Woven Natural Silk Fiber/Epoxy Sandwich Composite Panels under Low Velocity Impact.” *Fibers and Polymers* 14(1):127–32.

Vakis, A. et al. 2018. “Modeling and Simulation in Tribology Across Scales: An Overview.” *Tribology International*.

Valentini, L. et al. 2016. “Synergistic Effect of Graphene Nanoplatelets and Carbon Black in Multifunctional EPDM Nanocomposites.” *Composites Science and Technology* 128.

Vanossi, Andrea, Nicola Manini, Michael Urbakh, Stefano Zapperi, and Erio Tosatti. 2013. “Colloquium: Modeling Friction: From Nanoscale to Mesoscale.” *Reviews of Modern Physics* 85(2):529–52.

Varenberg, Michael, Nicola M. Pugno, and Stanislav N. Gorb. 2010. “Spatulate Structures in Biological Fibrillar Adhesion.” *Soft Matter* 6(14):3269. Retrieved (http://xlink.rsc.org/?DOI=c003207g).

Viney, C., J. Llorca, M. Elices, and J. Pe. 1998. “Silkworm Silk as an Engineering Material.” *Journal of Applied Polymer Science* 70:2439–47.

Wallen-Russell, Christopher and Ben Lishman. 2016. “The Friction of Saline Ice on Aluminium.” *Advances in Tribology* 2016.

Warnecke, Daniela et al. 2017. “Tribology International Friction Properties of a New Silk Fi Broin Sca Ff Old for Meniscal Replacement.” 109(November 2016):586–92.

Whitehouse, D. J. and J. F. Archard. 1970. “The Properties of Random Surfaces of Significance in Their Contact.” *Proceedings of the Royal Society A: Mathematical, Physical and Engineering Sciences* 316(1524):97–121. Retrieved (http://rspa.royalsocietypublishing.org/cgi/doi/10.1098/rspa.1970.0068).

Xing, Youqiang, Jianxin Deng, Ze Wu, and Fengfang Wu. 2017. “High Friction and Low Wear Properties of Laser-Textured Ceramic Surface under Dry Friction.” *Optics and Laser Technology* 93:24–32.

Yu, Jing et al. 2012. “Friction and Adhesion of Gecko-Inspired PDMS Flaps on Rough Surfaces.” *Langmuir* 28(31):11527–34.

Yu, Ying Song and Ya Pu Zhao. 2009. “Deformation of PDMS Membrane and Microcantilever by a Water Droplet: Comparison between Mooney-Rivlin and Linear Elastic Constitutive Models.” *Journal of Colloid and Interface*

Science 332(2):467–76. Retrieved (http://dx.doi.org/10.1016/j.jcis.2008.12.054).

Zhang, Xiaohui, Cassandra B. Baughman, and David L. Kaplan. 2008. "In Vitro Evaluation of Electrospun Silk Fibroin Scaffolds for Vascular Cell Growth." 29.

Zhao, Hong-Ping, Xi-Qiao Feng, and Hui-Ji Shi. 2007. "Variability in Mechanical Properties of Bombyx Mori Silk." *Materials Science and Engineering: C* 27(4):675–83. Retrieved (http://linkinghub.elsevier.com/retrieve/pii/S0928493106001998).

Zorlutuna, Pinar et al. 2012. "Microfabricated Biomaterials for Engineering 3D Tissues." *Advanced Materials* 24(14):1782–1804.

Appendix

In the following pages, an additional related work is reported, thanks to the collaboration with the University of Perugia. In particular, we focused on the tribological part reported in (Valentini et al. 2016).

A. Synergistic effect of graphene nanoplatelets and carbon black in multifunctional EPDM nanocomposites

Rubber is commonly considered the workhorse of the industrial and automotive products because of its good mechanical properties and its relatively low cost; finished products are found in the market place as compression moulded products. The physical and chemical resistance properties of rubber materials are determined by the addition of carbon black (CB) that historically has been utilized to reinforce rubber matrices [1,2].

However, since the main factors that affect the composite properties are the particle size and the mode of interactions with the matrix materials, single filler does not generally match the structural and functional requirements of rubber composites [3-7]. There are different types of carbon fillers (e.g., exfoliated graphite, carbon nanotubes and carbon fibres) and each type has its peculiar characteristic. For example, the percolation threshold of nanotubes is very low because of their high aspect ratio and it was found that the partial replacement of CB with carbon nanotubes leads to a much lower percolation threshold than that of the composite obtained with single filler and to a synergetic effect on the composite properties [8,9]; on the other hand the high cost hinders their large scale application. Exfoliated graphite is cheap and recently it was used as potential material for replacing CB for reinforcement of styrene-butadiene rubber. Its main

drawback is the percolation threshold that is usually high and detrimental for the mechanical properties.

Thus, the use of a combination of different carbon fillers would be a good way to get balanced properties and cost. A model for predicting the synergy between electrical conducting nanofillers, assumed immiscible, was applied for the optimal design of real nanocomposites [11]. Ma et al. [12] showed that the addition of carbon nanotubes into CB polymer composites enhanced the electric conductivity of the polymer matrix [12] with a low percolation threshold of about 0.4 wt.%. The combination of two or more carbon fillers was demonstrated to improve also the thermal performance of the composite due to the synergistic effect [13-14]. Recently, Yang et al. [15] studied the effects of substituting CB with graphene oxide/CB and reduced graphene oxide/CB hybrid fillers on the structure and properties of natural rubber composites.

Carbon fillers with different aspect ratio and sizes can be mixed with a host polymer matrix showing evidences of exfoliation and shortening of the particle size during mixing process even with expanded graphite. That suggests that simple mechanical milling can facilitate the exfoliation of the graphite layers into smaller dimension. Das et al. [16] reported a TEM and X-ray diffraction study of styrene butadiene rubber composites showing that the dispersion/exfoliation of the stacked graphene sheets into individual single sheets was facilitated by the presence of carbon black in the system. The existence of few-layer graphene sheets was attributed to a complex morphology arisen from filler –filler network interaction. The same authors [17] reported another study on solution styrene butadiene rubber composites reinforced with graphene nanoplatelets, expanded graphite, and multiwall carbon nanotubes. It was found that the high aspect ratio of carbon nanotubes enabled to form a network at low filler loading, leading to a good reinforcement effect.

Similarly to these previous attempts, Hu et al. [18] report a simple and effective way to disperse carbon nanotubes and graphene in silicone rubber and more

recently Li et al. [19] demonstrated toughening natural rubber by designing a compact hybrid filler network composed of graphene and carbon nanotubes.

In addition to graphene oxide, multi-layer graphene platelets also exhibit unique and useful behaviours. Multi-layer graphene, herein referred to as graphite nanoplatelets (GNPs) contains essentially no oxygen (<1% by weight of oxygen). Graphite nanoplatelets (GNPs) are obtained from graphite expansion that determines the platelet thickness [20,21]. With this method, 2D graphite materials consisting of hundreds of stacked graphene layers and named graphite nanoplatelets with ABA or ABCA stacking, and with a thickness and/or lateral dimension less than 100 nm are obtained.

The 2D nanoscale dimension of GNPs is a huge benefit in relation to the large conventional 3D fillers [22]. Those graphitic inclusions are characterized by far better shape factor, larger contact surface and higher mechanical strength. At the same time GNPs tend to aggregate and are difficult to disperse in polymer matrices due to the strong van der Waals attraction between the sheets and their high surface area, the synergy among the hybrid fillers comprising of graphite intercalation compounds, mainly GNPs, and CB could lead to the development of graphite-based elastomer composites exhibiting exceptional mechanical and thermal properties.

It is known that rubbers or elastomers generally have a low thermal conductivity. Consequently, when such materials are used as packaging for electronic circuit, they store the generated heat that in turn raises the temperature of the device itself, thereby promoting heat deterioration of the electronic component. To achieve this goal, the heat conduction capability of a rubber may be improved by compounding a rubber with a filler having a heat conductivity higher than that of the rubber.

High filler loadings (>30 vol.%) or traditional metallic materials were typically necessary to develop functional elastomers with appropriate level of thermal conductivity [23,24]. The employment of high filler loading makes difficult the processing, such as possibility to be extruded and injection moulded, while

traditional metallic materials with the highest thermal conductivity are too heavy and subjected to corrosion. Moreover, the reinforcing capacity is deteriorated after some certain value of filler amount. When a dramatic increase in properties, such as mechanical and thermal properties can be achieved when two different fillers both with saturate amount are added in rubber matrix synchronously, this is suggestive of synergistic effect.

In this work a part of carbon black with graphite nanoplatelets was replaced to produce ethylene-propylene diene terpolymer rubber (EPDM) based nanocomposites; a proper combination of graphite nanoplatelets lead to synergistic effect in improving the thermal conductivity, damping and mechanical properties of the nanocomposites. The effects of substituting GNPs for CB on the thermal, damping and mechanical properties of rubber/CB composites was studied and rationalized in terms of a mixture model.

A.1. Experimental details

Ethylene-propylene diene terpolymer rubber (EPDM) was kindly supplied by Exxon Mobil Chemical under the trade name Vistalon 7500 (ethylene content: 56.0 wt.% and 5-ethylidene-2-norbornene (ENB) content: 5.7 wt.%). Carbon black was kindly supplied by Cabot, S.A. under the trade name Vulcan 3-N330 (diameter 225 nm with a surface area of 77 m^2/g) and a paraffinic oil kindly supplied by Nynas, Nyflex 820 was used as plasticizer. Graphite nanoplatelets, an intermediate grade between graphene and graphite, which can neither be considered pure graphene nor graphite were purchased from Cheaptubes.

Rubber compounds were prepared in an open two-roll mill at room temperature. The rotors operated at a speed ratio of 1:1.4. The vulcanization ingredients were sequentially added to the elastomer before to the incorporation of the filler and sulphur. The recipes of the compounds are described in Table A.1. Vulcanizing conditions (temperature and time) were previously determined by a Monsanto Moving Die Rheometer MDR 2000E. Rubber compounds were then vulcanized

at 160 ºC in a thermofluid heated press. The vulcanization time of the samples corresponds to the optimum cure time t_{90} derived from the curing curves of the MDR 2000E. Specimens were mechanically cut out from the vulcanized plaques. Field emission scanning microscopy (FESEM) was used to investigate the cross section of the samples.

Ingredient	**EPDM -1 (0/0)**	**EPDM -2 (2/0)**	**EPDM -3 (5/0)**	**EPDM-4 (10/0)**	**EPDM -5 (0/48)**	**EPDM -6 (2/24)**	**EPDM -7 (5/48)**
EPDM Vistalon 7500	100	100	100	100	100	100	100
Paraffinic oil	80	80	80	80	80	80	80
Zinc oxide	5	5	5	5	5	5	5
Stearic acid	1	1	1	1	1	1	1
TMTD	1.5	1.5	1.5	1.5	1.5	1.5	1.5
Sulphur	3	3	3	3	3	3	3
Carbon black	---	---	---	---	190	95	190
Graphite Nanoplatelets	---	10	20	50	---	10	20

Table A.1 Recipes of the rubber compounds (indicated in phr: parts per hundred of rubber). The %weight content of GNPs/CB is reported below the name of each sample.

Tensile stress–strain properties were measured according to ISO 37–1977 specifications, on an Instron dynamometer (Model 4301), at 25 ºC at a crosshead speed of 500 mm*min^{-1}. At least five specimens of each sample were tested.

X-ray diffraction (XRD) experiments were conducted with an XRD diffractometer (Bruker) with a radiation source of Cu Kα and wavelength λ= 0.154

nm operating at 40 kV and 40 mA. The incidence angle (2θ) was fixed between 1° and 60° and the scan rate was 0.02°/s. Raman measurements were performed with Labram Raman spectroscopy (Horiba, Jobin-Yvon spectrometer) with a wavelength of 632.8 nm.

A ball-on-disk tribometer was used to determine the dynamic friction of coefficient of the composites. The samples were cut in order to have a squared base with different measures, from 8x8 mm^2 to 15x15 mm^2 (average values), depending on the given materials. They were fixed in the tribometer and the antagonist material we chose was steel (100Cr6), a sphere of 6 mm diameter in order to have a single contact point between the rubber and the steel. No lubricants were used. The sliding velocity was set at 0.01 m/s and the normal load varied from 0.05 N (softer samples) to 0.1 N (harder samples). For each sample from three to five measurements were realized.

The method used to measure the static friction coefficient is based on the Coulomb theory of friction. Each sample was positioned on a plate and fixed on it. After, a weight is put on the sample. The plate was then tilted until the stable configuration was overwhelmed and the weight slides on the rubber surface. The final configuration is tilted by a certain angle with respect to the initial position of the plate and corresponds to the transition from a stable state (static equilibrium) to an unstable one (incipient movement). The tangent of that angle corresponds to the ratio between the tangential force and the normal applied load (the weight). Five measures per sample were performed.

The damping properties were tested through a vibration generated via a pneumatic percussion system hitting a metallic plate. The impact area is a metallic plate where the sample to be tested has been fastened to. The sample was hit by a percussion which excites the vibration. A shock accelerometer positioned in the back plate is thus excited and the response is recorded and digitalized via high performance data acquisition system. The impact velocity was set to 8m/s

resulting in an impact energy of 58 J. Three tests were repeated on each sample; the experimental error was estimated below 1%.

Thermal conductivity measurements follow the "two thermometer-one heater" method using a custom built stage. Two PT100 thermocouples, contacted to the surfaces of a 13*40 mm^2 rectangular shape and 14 mm thick sample, monitor the temperature of two polished oxygen-free sample sides. A 3,4 Ohm resistor heats the top plate (13*40 mm^2 surface, 14 mm thick) to a temperature T_{Hot} . Heat flows from the top plate, through the sample, and into the bottom plate which is thermally grounded to T_{Cold} (i. e. 20°C) by the cold plate. Thermally conducting grease was used to enhance the thermal contact to the bottom of the sample.

The microstructure of the samples was investigated by micro tomography (micro-CT) using a Carl Zeiss Xradia Versa-410 3D X-ray microscope. The scan was performed over a 360° rotation using 1600 projections, 80 KV voltage, 7 W power, 80 sec exposure time, and 20x objective lens. The resulting nominal voxel (volumetric pixel) size was 0.36 micron and the total scan time was ~38 hours for each scan. Reconstruction of the attenuation data was performed using filtered back- projection, producing a stack of 967 cross-sectional, grey-scale digital images. The different components and their distributions have been analysed by segmenting regions of a given range of grayscale values from the rest of the image by using the XM3D viewer and Fiji software.

A.2. Results and discussion

Raman spectroscopy has been carried out to elucidate the Raman characteristics of 2D graphite material used in this work, such as differentiating few-layer and multi-layer from bulk graphite [25] and detecting structural defects [26]. The main features in Raman spectra reported in Figure A.1 a are the G and D bands and the second order of the D band, so-called 2D band. The G band, standing at around 1580 cm^{-1}, corresponds to in-plane carbon-atom stretching vibrations [26]. The positions of the D and 2D band are excitation-energy dependent and occur at

around 1329 cm^{-1} and 2663 cm^{-1}, respectively (Figure A.1 a). The D band is activated by the presence of defects [26]. After characterizations of a large number of AB-stacked few-layer graphene samples during the past years [27], the FWHM of 2D band (Figure A.1 b) unambiguously is associated to the graphite layer number. The typical FWHM of 2D peaks plotted in Figure A.1 b is consistent with five-layer graphitic material and thus with graphite nanoplatelets 2D materials with AB stacking, and having a thickness and/or lateral dimension less than 100 nm [27].

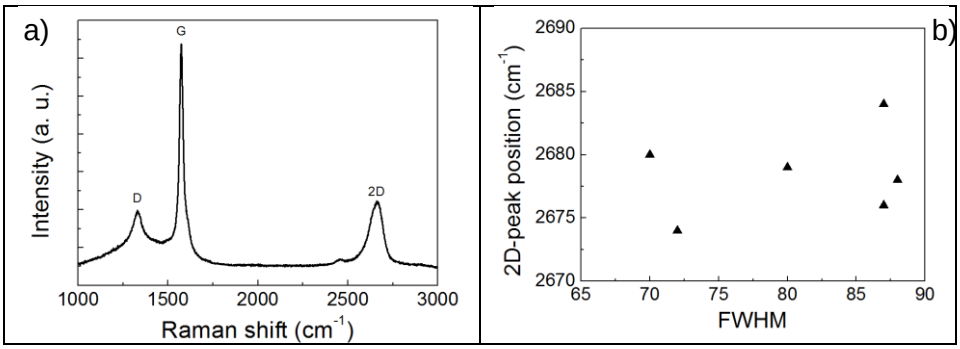

Figure A.1 a) Raman spectra of GNPs. b) The data of FWHM with respect to 2D peak positions.

Graphite nanoplatelets have attracted considerable attention in nanocomposites, thanks to the excellent in-plane mechanical and thermal properties of graphite. The stress-strain characteristics of the prepared nanocomposites are presented in Figure A.2 a and the tensile properties given in terms of the modulus at different strains (50%, 100% and 300%), maximum strength and elongation at break are reported in Figure A.2 b and Figure A.3, respectively. It is known that carbon blacks or silica when added to elastomers create a modulus that increases with strain. This non-linearity protects rubber from damage during large deformations [28]. Pristine GNPs provide enhanced non-linear strength to elastomers. The interface is similar to that of carbon black, the flexibility of the GNPs enables deformation at low strains and strengthening at higher deformations. As expected, the addition of the fillers to the EPDM matrix gives rise to an increase in the stiffness of the material which is reflected in an improvement of the modulus at

different strains (Figure A.2). The elongation at break, as an indicator for the toughness of the materials, decreases when adding GNPs to the EPDM/CB blend (Figure A.3) (i. e. EPDM-7 sample). The synergistic effect of CB and GNPs is evident in the sample EPDM-6 (i. e. 2 wt.% of GNPs and 24wt.% of CB) that showed a higher increment of the maximum strength (Figure A.2) along with a higher elongation at break with respect to the EPDM/CB blends (Figure A.3).

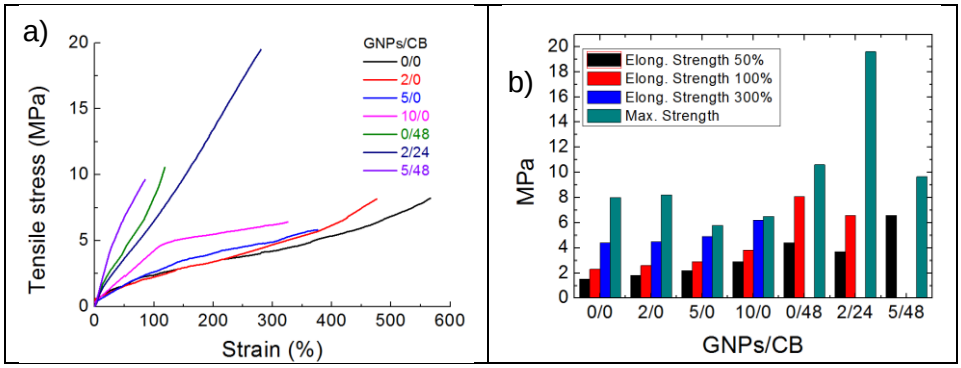

Figure A.2 (a) Stress-strain curves of the prepared samples. (b) Modulus at different strains and maximum strength of the prepared samples.

For a system containing two types of fillers such as GNPs and CB, our results can be rationalized in terms of the following mixture model:

$$\sigma = \sigma_m(1-f_{GNPs}-f_{CB})+\sigma_{GNPs}f_{GNPs}+\sigma_{CB}f_{CB}$$

where σ is again the composite strength, σ_m is the matrix strength, σ_{GNPs} is the GNP strength, σ_{CB} is the CB strength and f_{GNPs} and f_{CB} are the GNPs and CB concentrations, respectively.

Assuming σ_{GNPs}= 800 MPa [29], σ_{CB} ~14MPa (obtained by using the rule of mixture for CB single phase $\sigma \cong \sigma_m(1-0.48)+0.48\sigma_{CB}$) and f_{GNPs} and f_{CB} the concentrations for obtaining the maximum of the mechanical resistance, the model predict for the composite a mechanical strength of about 25MPa that is in good agreement with that obtained experimentally (i.e. ~20MPa). For a single phase inclusion, if an ideal dispersion, thus without agglomeration, is considered, the

composite mechanical resistance would depend linearly on the percentage of the phase itself, thus an increment of *f* would cause an increment also in the mechanical resistance (assuming the strength of the inclusion much larger than that of the matrix). This is not true if the agglomeration of the phase takes place. In the model for two immiscible phases, the synergy can be understood as a retardation of the agglomeration towards higher total concentration as reported below.

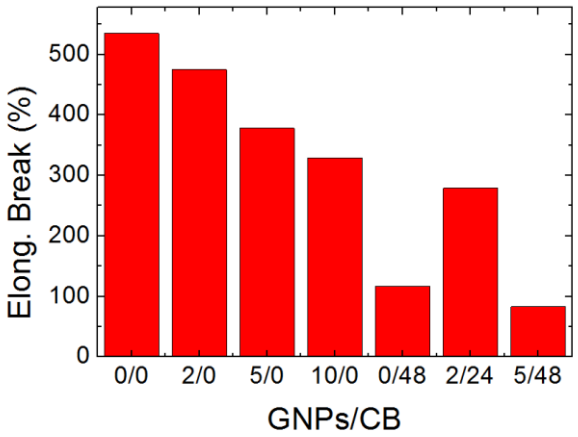

Figure A.3 Elongation at break of the prepared samples.

The dynamic friction coefficients of the samples were estimated accordingly to the Herzian analysis for a smooth sphere in contact with a smooth flat surface, where the radius of contact circle expressed as *a=[3LR/4E]^1/3*, where *L* is the applied load, *R* is the sphere radius and *E* is the elastic modulus of the softer material (i.e. rubber). In the present case, the only parameter varied was the load, thus accordingly to the mechanical properties, it was decreased for the softer composite samples containing a GNP/CB ratio of 2/0, 5/0 and 10/0, respectively. The final values are shown in Figure A.4. For composites with a GNP/CB ratio of 5/0, 10/0 and 2/24 values major than 1 were obtained and in literature for particular combinations of rubbers similar results were found (i. e. rubber-steel contact) [30-34]. It was also reported that the dynamic friction coefficient depends

on the sliding velocity, it increases if the velocity increases, but becomes almost stable for velocities around 0.01 m/s [30-34].

The static coefficient of friction of the samples was estimated by putting a weight made of steel (0.7 g) on the rubber samples and tilting the plate, until the incipient sliding was reached. The dynamic and static coefficients of friction are not comparable due to the different type of steel used as counterpart as well as the different type of setup adopted for dynamic and static tests. The addition of GNPs to the EPDM/CB blend reduces the static coefficient of friction while the partial substitution of CB with GNPs did not affect the grip of the EPDM/CB sample surfaces.

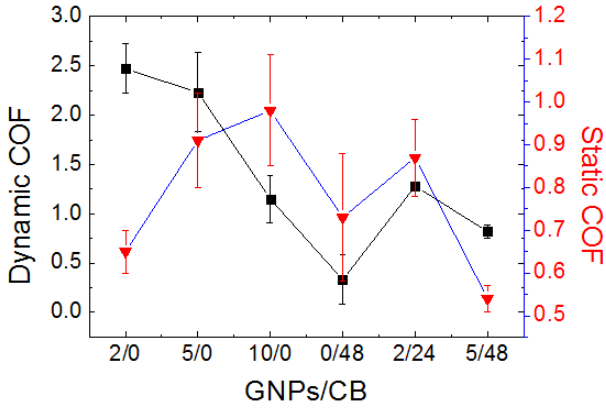

Figure A.4 Dynamic and static coefficient of friction measured of the prepared samples.

Figure A.5 reports the peak acceleration measured in the impact excitation test. The damping of the sample can be qualitatively estimated by the peak acceleration. No data were recorded on neat EPDM due to the cracking of the samples even at lower impact velocity. It is evident how in the composites, the impact performances depend on the elongation at break; in particular, the higher stiffness of the composites with CB shows a scarce damping properties. The obtained results can be explained with the increase in the modulus at different strain along with the reduction of elongation when the GNPs were added. The addition of 5wt.% of GNPs in the 48 wt.% CB filled matrix deteriorates the

damping properties. The partial substitution of CB in the sample with 2 wt.% of GNPs and 24 wt.% of CB showed the best shock absorbing performance with a lower variation of the acceleration peak after the impact.

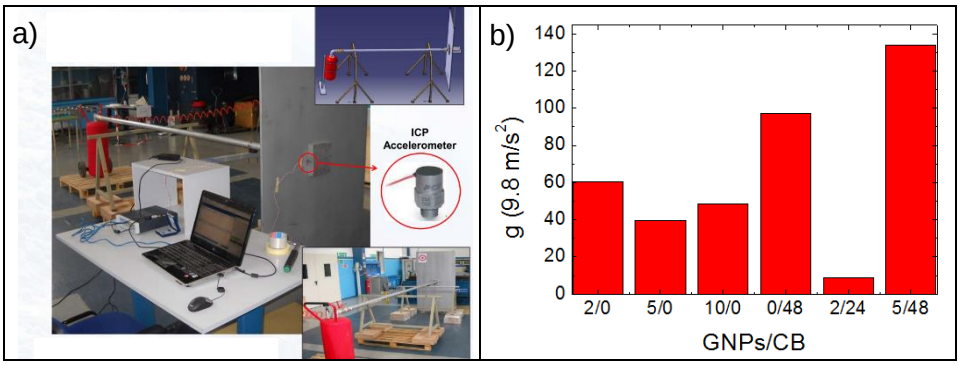

Figure A.5 Set-up of the impact test. The impact area is a metallic plate where the sample to be tested has been fastened to. The sample was hit by a percussion which excites the vibration. A shock accelerometer positioned in the back plate is thus excited and the response is recorded and digitalized via high performance data acquisition system. b) Peak acceleration measured by the accelerometer in the impact test of the prepared samples.

Figure A.6 a shows the experimental set up for the thermal conductivity measurements. The in-plane thermal conductivity was measured through a rectangular shaped (1.5cm wide, 1.4 mm high, 4cm long) specimen, as shown in Figure 5a.

The in-plane thermal conductivity test method was used with the goal to conduct heat only by conduction through the solid sample.

A Mylar cap around the cold plate fixed at T_{Cold} and a high vacuum 10^{-5} Torr reduce thermal losses due to radiation and convection, respectively. When the sample is powered, the generated heat flows through the sample from the sample heater to the cold plate. Heat is generated in the sample from electrical resistance heating of the sample heater.

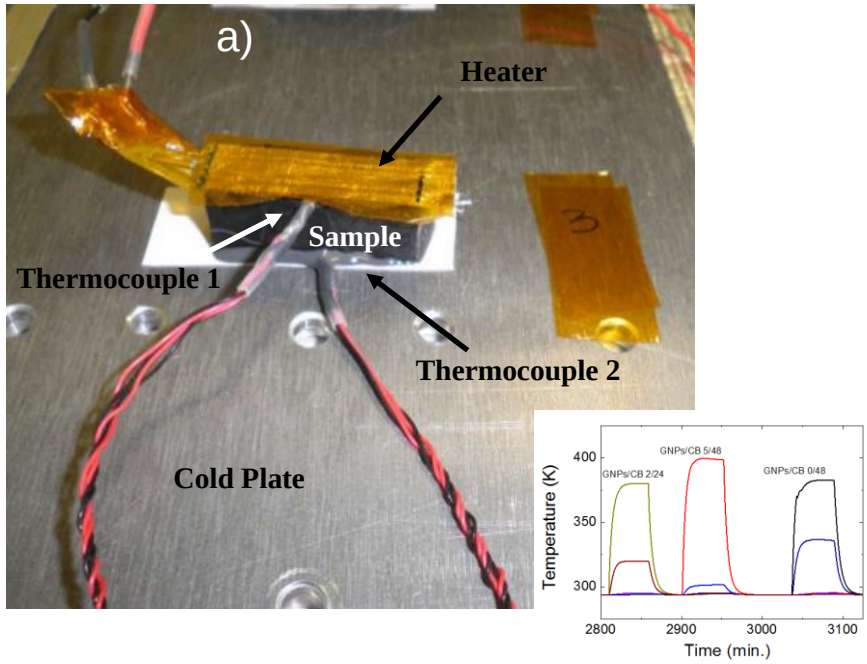

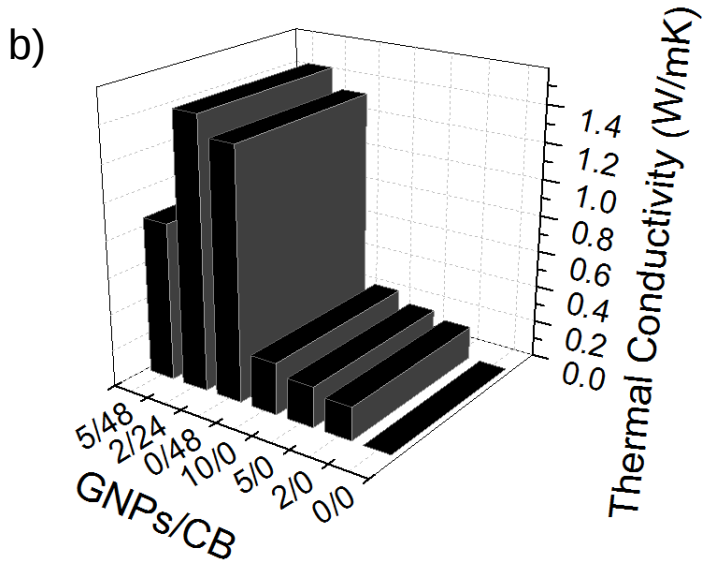

Figure A.6 (a) Set up of the thermal conductivity measurements. (b) Thermal conductivity values as a function of the GNPs/CB content.

Thus, heat is equal to the power dissipated by the resistor (*V*I*). Figure A.6 a illustrates this set up. The thermal conductivity of the specimen is determined by [35] $\lambda=(V*I/\Delta T)*(d/A)$ where λ is the thermal conductivity of the specimen being tested; *V* is the voltage drop across the sample heater resistor; *I* is the current through the sample heater resistor; ΔT is the temperature difference across the specimen; *d* is the distance between the two junctions of the thermocouples; and *A* is the cross-sectional area of the specimen (specimen width*specimen height). Such in-plane thermal conductivity test method is based on the steady state method (see inset of Figure A.6 a).

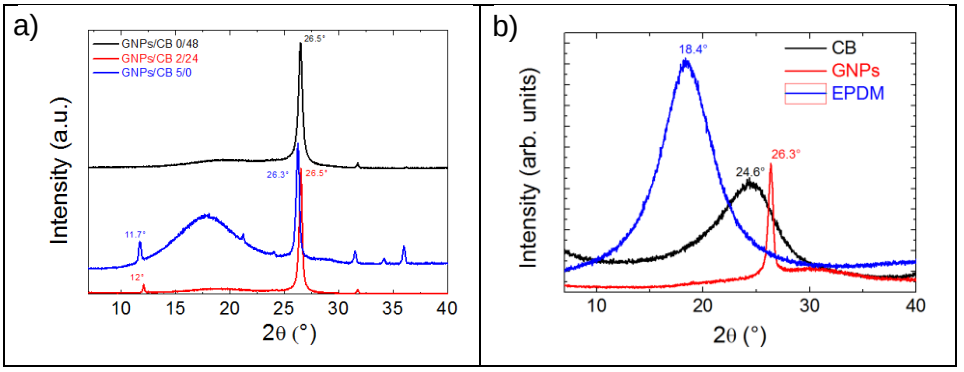

Figure A.7 X-ray diffraction patterns of (a) EPDM nanocomposites with different GNPs/CB content and (b) CB, GNPs and neat EPDM.

In analogy with electrical conductivity, the thermal conductivity of polymers filled with conducting nanoparticles derives from the formation of a percolation network of the fillers in the matrix [36]. The increasing of the conductive paths enhances the composite thermal conductivity. As for the CB filler alone EPDM-5 (i. e. 48 wt.% CB), the conductive network is formed due to the contact between GNPs and CB. For the sample EPDM-6 (i. e. 2 wt.% GNPs and 24 wt.% CB) when GNPs are added into the CB composite, GNP particles act as spacers between the CB agglomerates, which leads to the formation of linked conductive paths (Figures 6b). As proof of this statement, XRD, FESEM and MCT analyses were performed.

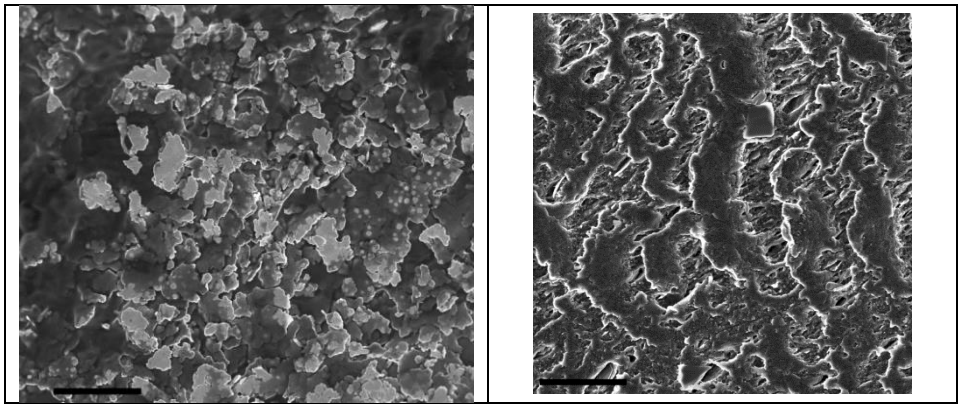

Figure A.8 FESEM images of the a) EPDM-6 and b) EPDM-7 samples. The arrows in Figure A.6 a) shows the CB agglomerates on a GNP sheet. The scale bars indicate 1 μm.

XRD experiments on GNPs and CB related rubber composites are reported in Figure A.7 a. All XRD spectra present a broad region at 2θ = 14°-20° due to the EPDM polymer reported in Figure A.7 b [37].

Figure A.7 b shows the X-ray diffractogram recorded for the pristine carbon black; the spectrum reveals a peak at about 2θ=24.6°, which is the $d^{(002)}$ 3.72Å lattice spacing of the graphite layers [38,39]. XRD pattern of the EPDM-5 (i. e. 48 wt.% CB) with CB filler alone, reveals that the EPDM region is followed by a distinct crystalline region at 2θ = 26.5°. This results is in agreement with a previous study reported in ref. [40], stating that carbon black aggregates tend to concentrate in amorphous regions of the polymer matrix; the peak at 2θ of about 32° corresponds to (100) lattice plane of the hexagonal wurtzite structure of zinc oxide (ZnO) [41]. XRD pattern of EPDM-3 (i. e. 5 wt.% GNPs) shows three significant peaks at 2θ of about 32°, 34° and 36° corresponding to (100), (001) and (101) lattice planes of the hexagonal wurtzite structure of zinc oxide (ZnO), respectively [41]. By comparison with the XRD pattern of pristine graphite nanoplatelets reported in Figure A.7 b, it is evident that the peak at about 26.3° is due to the GNPs. The diffraction peak at about 11,7° is attributed to the intrinsic diffraction of oxidized graphite, as confirmed by the XRD pattern of oxidized graphite reported

elsewhere [42] and indicated by Raman measurement that there are substantial defects on graphite plane prone to be oxidized during the vulcanization process.

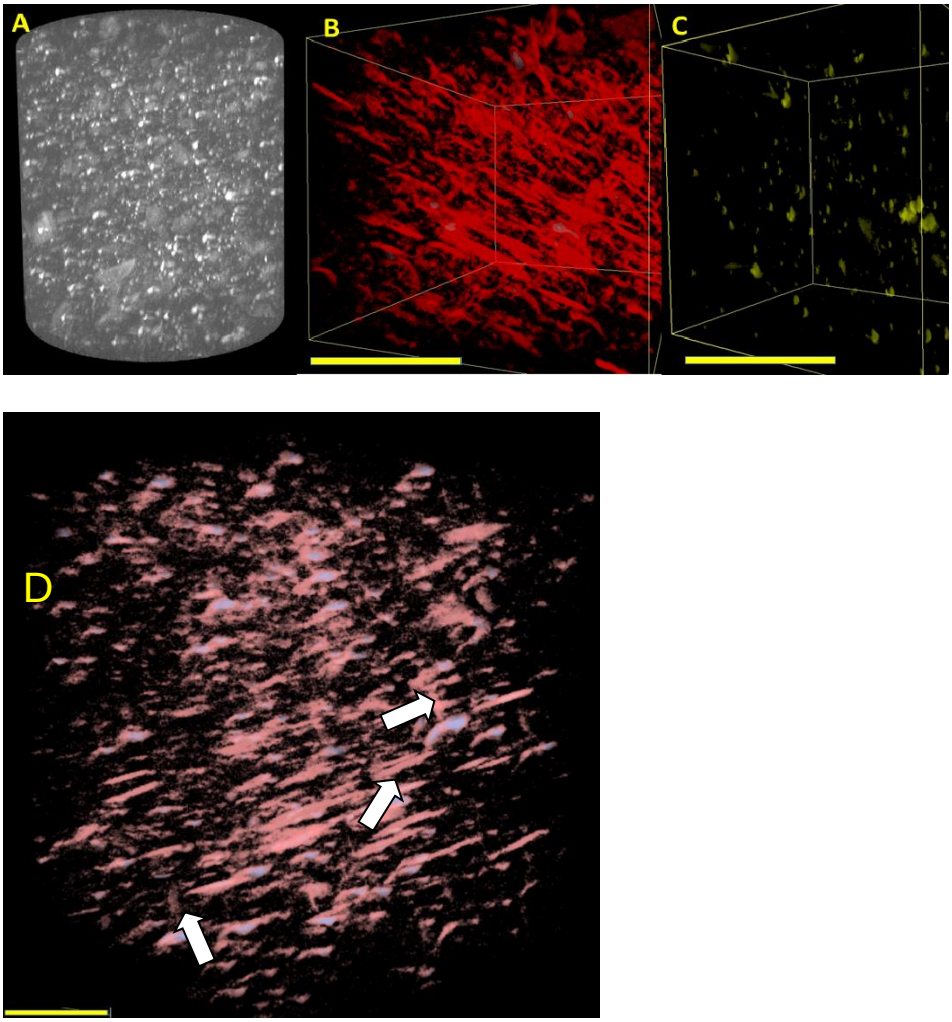

Figure A.9 a) Total cylindrical volume of the EPDM-6 sample (348 micron in diameter and 360 micron in height); b) and c) Detail of segmented CT images showing the distribution of the graphite nanoplatelets and carbon black aggregates, respectively (scale bar is 50 microns). d) Detail of segmented CT images showing the whole distribution of the graphite nanoplatelets (in red) and carbon black aggregates (in blue indicated by the arrows) (scale bar is 50 microns).

Accordingly to Wei et al. [36], our FESEM analysis reported in Figure A.8 a shows small CB agglomerates attached on the surface and edge of the GNPs. On the other hand, increasing the GNPs content into the sample with the highest CB concentration (i. e. 5 wt.% GNPs and 48 wt.% CB) contribute to the increase in the CB agglomeration resulting in a decrease of both impact properties and thermal conductivity (Figures 6b and 8b).

Figure A.9 shows the results of micro-CT analyses for the sample EPDM-6 (i. e. 2 wt.% GNPs and 24 wt.% CB). The raw data acquired by the X-ray microscope have been processed using tomographic reconstruction, producing a stack of 967 cross-sectional, grey-scale digital images. The total cylindrical volume of the analysed sample has 348 microns in diameter and 360 microns in height (Figure A.9 a). As the grey level value in 3D image is related to the X-ray absorption of the material, the concentrated CB agglomerates are shown in lighter grey to white colour, while GNPs due to its flat shape is shown in darker grey colour.

Image analysis techniques have been applied in order to segment the 3D imaged data and separate the different materials by their grey level value. Segmented CT images reported in Figures 9a and 9b, show that both GNPs and CB are uniformly dispersed within the polymer matrix. Particularly CB forms aggregates (Figure A.9 d) mostly on the surface of the graphite nanoplatelets linking the gap distance between the GNPs resulting in the formation of additional conductive paths and increasing the interface resistance in the hybrid composite.

A.3. Conclusions

In this paper we adopt a processing technology to develop elastomer plus nano-graphite hybrid composites with multifunctional properties. Beyond the improvements of the mechanical properties, the research findings demonstrate the synergistic effect of carbon black and graphite nanoplatelets to prepare rubber composites thermally conductive and to design a new class of shock absorbers. It was found that a critical GNPs/CB ratio was able to reduce the strong interlayer

forces among the GNPs sheets, which led to the efficiency on reinforcement in mechanical properties and improvements of the performance of the rubber composites.

A.4. References

[1] Rattanasom N, Saowapark T, Deeprasertkul C. Reinforcement of natural rubber with silica/carbon black hybrid filler. Polym Test 2007;26, 369-377.

[2] Yimin Zhang S, Ge B, Tang T, Koga M, H Rafailovich J C, Sokolov D G, Peiffer Z, Li A, J Dias K O, McElrath M Y, Lin S, K Satija S G, Urquhart H, Ade H, Nguyen D. Effect of carbon black and silica fillers in elastomer blends Macromolecules 2001;34, 7056-7065.

[3] Wang, M. J.; Mahmud, K.; Murphy, L. J.; Patterson, W. J. Kautsch. Gummi Kunstst. 1998, 51, 348.

[4] Qu L L, Huang G S, Zhang P, Nie Y J, Weng G S, Wu J R. Synergistic reinforcement of nanoclay and carbon black in natural rubber. Polym Int 2010;59, 1397-1402.

[5] Verdejo R, Lopez-Manchado M A, Valentini L, Kenny J M. Carbon nanotube reinforced rubber composites in S. Thomas R. Stephen (Eds.), Rubber Nanocomposites, Wiley, Singapore, 2010, 147-168, Chapter 6.

[6] Wang Z, Meng X Y, Li J Z, Du X H, Li S Y, Jiang Z W, Tang T. A Simple method for preparing carbon nanotubes/clay hybrids in water. J Phys Chem C 2009;113, 8058-8064.

[7] Tang Z H, Wei Q Y, Lin T F, Guo B C, Jia D M. The use of a hybrid consisting of tubular clay and graphene as a reinforcement for elastomers. RSC Adv 2013;3, 17057-17064.

[8] Zhang S M, Lin L, Deng H, Gao X, Bilotti E, Peijs T, Zhang Q, Fu Q. Synergistic effect in conductive networks constructed with carbon nanofillers in different dimensions. Express Polym Lett 2012;6, 159-168.

[9] Galimberti M, Coombs M, Riccio P, Ricco T, Passera S, Pandini S, Conzatti L, Ravasio A, Tritto I.

The role of CNTs in promoting hybrid filler networking and synergism with carbon black in the mechanical behavior of filled polyisoprene. Macromol. Mater. Eng. 2013;298, 241-251.

[10] Mao Y, Wen S, Chen Y, Zhang F, Panine P, Chan TW, Zhang L, LiangY, Liu L. High performance graphene oxide based rubber composites. Sci Reports 2013;3, 2508-2515.

[11] Sun Y, Bao H-D, Guo Z-X, Yu J. Modeling of the electrical percolation of mixed carbon fillers in polymer-based composites. Macromolecules 2009;42, 459-463.

[12] Ma PC, Liu MY, Zhang H, Wang SQ, Wang R, Wang K. Enhanced electrical conductivity of nanocomposites containing hybrid fillers of carbon nanotubes and carbon black. Acs Appl Mater Inter 2009;1:1090–6.

[13] Weber EH, Clingerman ML, King J A. Thermally conductive nylon 6,6 and polycarbonate based resins. I. Synergistic effects of carbon fillers. J Appl Polym Sci 2003;88, 112-122.

[14] Lee GW, Park M, Kim J, Lee JI, Yoon H G. Enhanced thermal conductivity of polymer composites filled with hybrid filler. Compos. A 2006;37, 727-734.

[15] Yang G, Liao Z, Yang Z, Tang Z, Guo B. Effects of substitution for carbon black with graphene oxide or graphene on the morphology and performance of natural rubber/carbon black composites. J Appl Poly Science 2015;132, 41832.

[16] Das A, Boldt R, Jurk R, Jehnichen D, Fischer D, Werner Stockelhuber R, Heinrich G. Nano-scale morphological analysis of graphene –rubber composites using 3D transmission electron microscopy. RSC Advances 2014;4, 9300-9307.

[17] Das A, Boldt R, Jurk R, Jehnichen D, Fischer D, Werner Stockelhuber R, Heinrich G. Rubber composites based on graphene nanoplatelets, expanded graphite, carbon nanotubes and their combination: A comparative study. Comp Sci Technol 2012;72, 1961-1967.

[18] Hu H, Zhao L, Liu J, Liu Y, Cheng J, Luo J, Liang Y, Tao Y, Wang X, ZhaoJ. Enhanced dispersion of carbon nanotube in silicone rubber assisted by grapheme. Polymer 2012;53, 3378-3385.

[19] Li H, Yang L, Weng G, Xing W, Wu J, Huang G. Toughening rubbers with a hybrid filler network of graphene and carbon nanotubes. J Mater Chem A 2015;3, 22385-22392.

[20] Chung DDL. Exfoliation of graphite. J Mater Sci 1987;22, 4190-4198.

[21] Chung DDL. Review graphite. J Mater Sci 2002;37(8):1475–1489.

[22] Pugno, N. Nanotube Superfiber Materials: Changing Engineering Design 2013, 495-518.

[23] Araby S, Zaman I, Meng Q, Kawashima N, Michelmore A, Kuan H-C, Majewski P, Ma J, Zhang L. Melt compounding with graphene to develop functional, high-performance elastomers. Nanotechnology 2013;24, 165601.

[24] Han Z, Fina A. Thermal conductivity of carbon nanotubes and their polymer nanocomposites: A review. Progress in Polymer Science 2011;36, 914-944.

[25] Editorial. All in the graphene family – A recommended nomenclature for two-dimensional carbon materials. Carbon 2013;65, 1-6.

[26] Ferrari AC, Meyer JC, Scardaci V, Casiraghi C, Lazzeri M, Mauri F, Piscanec S, Jiang D, Novoselov KS, Roth S, Geim AK. Raman Spectrum of graphene and graphene layers. Phys Rev Lett 2006;97, 187401.

[27] Hao Y, Wang Y, Wang L, Ni Z, Wang Z, Wang R, Koo CK, Shen Z, Thong JTL. Probing layer number and stacking order of few-layer graphene by raman spectroscopy. Small 2010;6, 195-200.

[28] Tosaka M, Kawakami D, Senoo K, Kohjiya S, Ikeda Y, Toki S, Hsiao B S. Crystallization and stress relaxation in highly stretched samples of natural rubber and its synthetic analogue. Macromolecules 2006;39, 5100-5105.

[29] Valentini L, Bittolo Bon S, Signetti S, Pugno NM. Graphene based bionic composites with multifunctional and repairing properties. ACS Applied Materials & Interfaces 2016; DOI: 10.1021/acsami.6b02530.

[30] Roth FL, Driscoll R L, Holt W L. Frictional Properties of Rubber. Rubber Chemistry and Technology. 1943;16, 155-177.

[31] Leilei W, Zhang L, Tian M. Effect of expanded graphite (EG) dispersion on the mechanical and tribological properties of nitrile rubber/EG composites. Wear 2012; 276, 85-93.

[32] Song SH, Jeong HK, Kang YG. Preparation and characterization of exfoliated graphite and its styrene butadiene rubber nanocomposites. Journal of Industrial and Engineering Chemistry 2010;16, 1059–1065.

[33] Karger-Kocsis J, Mousa A, Major Z, Békési N. Dry friction and sliding wear of EPDM rubbers against steel as a function of carbon black content. Wear 2008;264, 359-367.

[34] Felhös D, Karger-Kocsis J. Tribological testing of peroxide-cured EPDM rubbers with different carbon black contents under dry sliding conditions against steel. Tribology International 2008;41, 404-415.

[35] Demain A, Issi, JP. Effective thermal conductivity of composites with interfacial thermal barrier resistance. J Compos Mater 1993;27, 668-683.

[36] Wei T, Song L, Zheng C, Wang K, Yan J, Shao B, Fan Z-J. The synergy of a three filler combination in the conductivity of epoxy composites. Materials Letters 2010;64, 2376–2379.

[37] Hu X, Gao H, Zhou X, Cui Y, Ge H. A new approach to rubber reinforcement. RSC Adv. 2014;4, 13662-13668.

[38] Charreteur F, Jaouen F, Ruggeri S, Dodelet J-P. Fe/N/C non-precious catalysts for PEM fuel cells: Influence of the structural parameters of pristine commercial carbon blacks on their activity for oxygen reduction. Electrochimica Acta 2008;53, 2925–2938.

[39] Biscoe J, Warren B E. An X-ray study of carbon black. J Appl Phys 1942;13, 364–371.

[40] Lawandy SN, Halim SF, Darwish NA. Structure aggregation of carbon black in ethylene-propylene diene polymer. eXPRESS Polymer Letters 2009;3, 152–158.

[41] Allahbakhsh A, Mazinani S, Kalaee MR, Sharif F. Cure kinetics and chemorheology of EPDM/grapheme oxide nanocomposites. Thermochimica Acta 2013;563, 22–32.

[42] Valentini L, Cardinali M, Kenny JM, Prato M, Monticelli O. A photoresponsive hybrid nanomaterial based on graphene and polyhedral oligomeric silsesquioxanes. European Journal of Inorganic Chemistry 2012; 5282-5287.

Whenever two bodies are in contact due to a normal load and one is sliding against the other, a tangential force arises, opposed to the motion. This force is called friction force, and involves different mechanisms, such as asperity interactions, energy dissipation, chemical and physical alterations of the surface topography and wear. The friction coefficient is defined as the ratio between the friction force and the applied normal load. Despite this apparently simple definition, friction appears to be a very complex phenomenon, which also involves several aspects at both the micro- and nano-scale, including adhesion and phase transformation. Moreover, it plays a key role in a variety of systems, and must be either enhanced (e.g. for locomotion) or minimized (e.g. in bearings), depending on the application.

Considering friction as a multiscale problem, an analytical model has been proposed, starting from the literature, to describe friction in the presence of anisotropy, adhesion and wear between surfaces with hierarchical structures, e.g. self-similar. This model has been implemented in a MATLAB code for the design of the tribological properties of hierarchical surfaces and has been applied to study the ice friction, comparing analytical predictions with experimental tests.

Furthermore, particular isotropic or anisotropic surface morphologies (e.g., microholes of different shapes and sizes) has been investigated for their influence to the static and dynamic friction coefficients with respect to a flat counterpart. In particular, it has been proved that the presence of grooves on surfaces could decrease the friction coefficients and thus reduce wear and energy dissipation. Experimental tests were performed with a setup realized *ad hoc* and the results were compared with full numerical simulations.

If patterned surfaces showed that they can reduce sliding friction, other applications could require an increase in energy dissipation, e.g. to enhance toughness of microfibers. Specifically, the applied method consists of introducing sliding frictional elements (sliding knots) in biological (silkworm silk, natural or degummed) and synthetic fibers, reproducing the concept of molecules, where the sacrificial bonds provide higher toughness to the molecular backbone, with a hidden length, which occurs after their breakage. A variety of slip knot topologies with different unfastening mechanisms have been investigated, including even complex knots usually adopted in textile industry. The knots were made by manipulation of fibers with tweezers and the resulting knotted fibers were characterized through nanotensile tests to obtain their stress-strain curve until failure. The presence of sliding knots strongly increase the dissipated energy per unit mass, without compromising the structural integrity of the fiber itself.